Restoring mangroves with structures

Improving the mangrove habitat using local materials

Gijón Mancheño, A.

DOI
10.4233/uuid:ed292367-ed2b-4bd3-a236-9f10d9c01da8

Publication date
2022

Document Version
Final published version

Citation (APA)
Gijón Mancheño, A. (2022). *Restoring mangroves with structures: Improving the mangrove habitat using local materials*. [Dissertation (TU Delft), Delft University of Technology].
https://doi.org/10.4233/uuid:ed292367-ed2b-4bd3-a236-9f10d9c01da8

RESTORING MANGROVES WITH STRUCTURES

Alejandra Gijón Mancheño

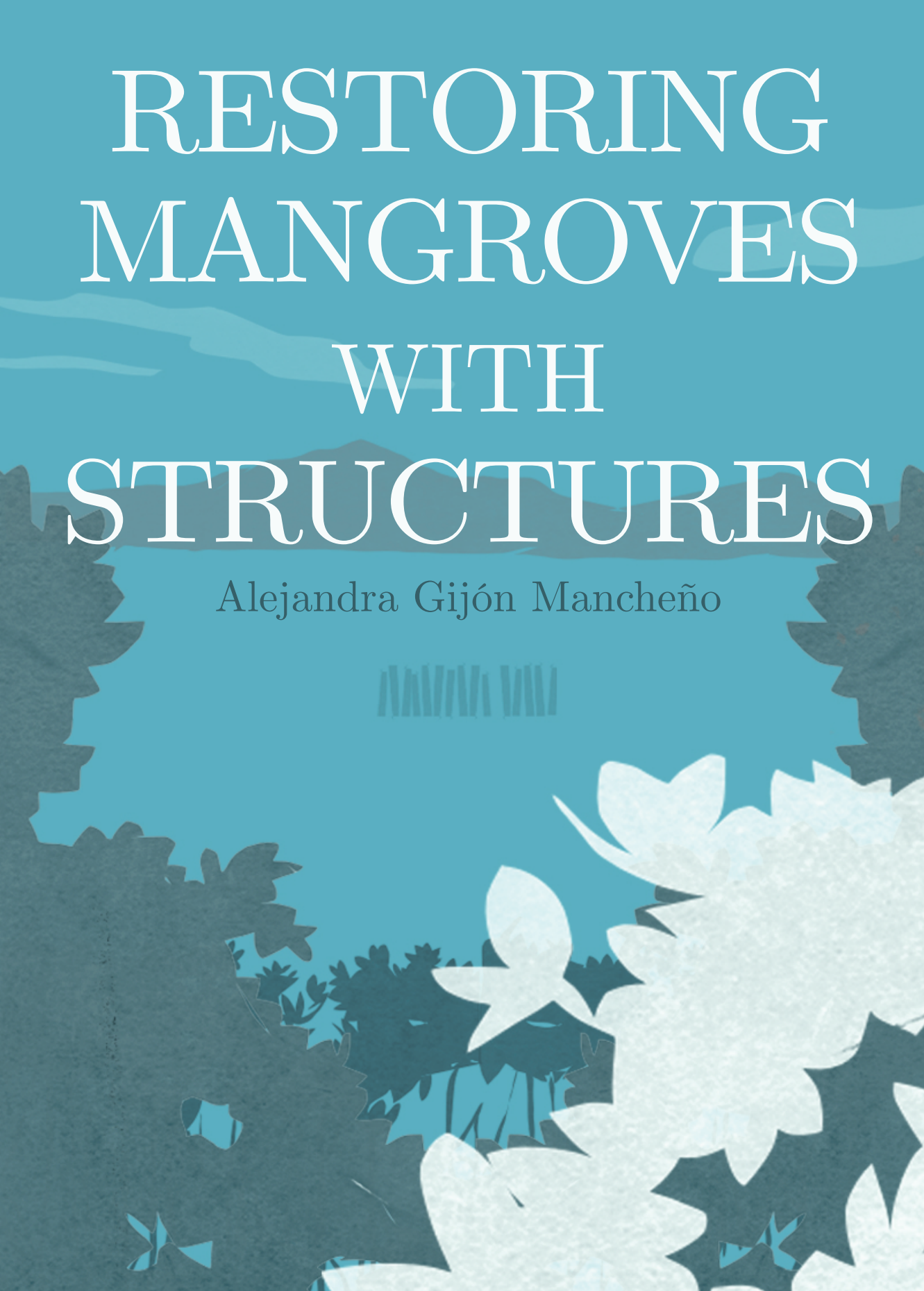

RESTORING MANGROVES WITH STRUCTURES

IMPROVING THE MANGROVE HABITAT USING LOCAL MATERIALS

RESTORING MANGROVES WITH STRUCTURES

IMPROVING THE MANGROVE HABITAT USING LOCAL MATERIALS

PROEFSCHRIFT

ter verkrijging van de graad van doctor aan de Technische Universiteit Delft, op gezag van de Rector Magnificus prof. dr. ir. T.H.J.J. van der Hagen, voorzitter van het College voor Promoties, in het openbaar te verdedigen op donderdag 29 september 2022 om 13:00 uur door

Alejandra GIJÓN MANCHEÑO

Ingenieur in de Civiele Techniek, Universidad de Sevilla, Spanje,
Master of Science in Coastal and Maritime Engineering and Management, Norwegian University of Science and Technology, University of Southampton, and Technische Universiteit Delft,
geboren te Sevilla, Spanje.

Dit proefschrift is goedgekeurd door de promotoren.

Samenstelling promotiecommissie:

Promotor: prof. dr. W.S.J. Uijttewaal
Promotor: prof. dr. A.J.H.M. Reniers

Onafhankelijke leden:

Prof. dr. K.R. Bryan
Prof. dr. M. Muskananfola
Prof. dr. T.J. Bouma
Prof. dr. P.M.J. Herman
Prof. dr. J.C. Winterwerp

Overige leden:

Prof. dr. Dano J.A. Roelvink

BioManCO project consortium partners: Deltares, Delft University of Technology, Ecoshape, NIOZ, Universitas Diponegoro, Wetlands International, Witteveen and Bos

KEYWORDS: mangroves, restoration, bamboo structures

PRINTED BY: Ridderprint, www.ridderprint.nl

FRONT & BACK: illustration of a mangrove coastline, by A. Gijón Mancheño

ISBN 978-94-6458-601-5

An electronic version of this dissertation is available at hhtp://repository.tudelft.nl/.

Summary

Mangrove forests effectively function as natural flood defences, and their deforestation has exposed millions of people worldwide to coastal erosion and flooding. Since mangroves require a stable sedimentary environment, stopping coastal erosion is a necessary step for their restoration. Bamboo structures have thus been built to induce accretion at the coast by attenuating waves. However, these structures often fail to rehabilitate mangroves, likely due to the lack of guidelines for their design.

This thesis investigates the effect of structures formed by bamboo poles on waves, currents, and sediment transport, to develop physics-based models for structure design. These effects were studied through flume experiments with scaled structure prototypes, field experiments in Demak (Indonesia), 1D morphodynamic modelling (with the model XMgrove, calibrated with field measurements), and remote sensing.

Models to predict structure performance were developed for waves and currents. Flume experiments showed ways to optimize structure designs. For instance, wave dissipation per pole is maximum for dense rows of poles with large spacing in the wave direction. Modelling scenarios with XMgrove suggest that the optimal structure location is site-dependent, and that subsidence rates in Demak may be too high to be counteracted with structures. A large-scale method to find potential restoration sites was also developed and applied in Bangladesh.

As such, the physics-based tools, together with the mapping method presented in this thesis, open up the path to optimize and generalize mangrove restoration efforts.

Samenvatting

Mangrove bossen dienen als natuurlijke bescherming tegen overstromingen. Hun ontbossing stelt miljoenen mensen bloot aan erosie van de kust en overstromingen. Voor mangroven is een stabiel sedimentklimaat van belang, daarom is het stoppen van erosie van belang voor hun herstel. Bamboe-constructies worden gebouwd om golven te verzwakken en daarmee sediment laten aanwassen aan de kust. Echter, het gebruik van bamboe-constructies voor mangrove herstel mislukt vaak vanwege een gebrek aan ontwerprichtlijnen.

In dit proefschrift wordt het effect van bamboe-paal constructies op golven, stroming en sediment transport onderzocht om fysische modellen te ontwikkelen voor het ontwerpen van de constructies. Deze effecten zijn bestudeerd middels goot-experimenten experimenten met schaalmodellen, veld-experimenten in Demak (Indonesië), 1D- morphodynamische modellen (met het XMgrove model, gekalibreerd met metingen), en remote-sensing.

Modellen om de effectiviteit van de stucturen te testen zijn ontwikkeld voor golven en stroming. Goot-experimenten experimenten hebben aangetoond dat de golf dissipatie per paal maximaal is voor rijen waar de palen dicht op elkaar staan in de niet-golfrichting terwijl ze ver van elkaar staan in de golfrichting. Model scenario's met XMgrove duiden erop dat de optimale locatie voor de constructies afhankelijk is van het gebied, en dat de bodemdaling in Demak mogelijk te groot is om te compenseren met constructies. Er is ook een grootschalige methode ontwikkeld en gebruikt om mogelijke herstel locaties in Bangladesh in kaart te brengen.

Concluderend, de fysische modellen samen met de methode om herstel locaties in kaart te brengen openen de weg naar de optimalisatie en generalisatie van toekomstige herstel-programma's.

Ringkasan

Hutan bakau merupakan salah satu penahan banjir alami yg disediakan alam, namun rusaknya mangrove telah membuat wilayah pesisir yang ditempati oleh jutaan manusia terkena erosi pantai dan banjir. Struktur bambu merupakan salah satu metode yang telah dibangun untuk membantu proses akresi di pantai dan juga berfungsi untuk meredam gelombang. Namun, struktur ini sering gagal untuk merehabilitasi mangrove, hal ini dikarenakan kurangnya studi untuk desainnya.

Tesis ini bertujuan untuk menyelidiki pengaruh struktur yang dibentuk oleh tiang bambu pada gelombang, arus, transportasi sedimen, dan untuk mengembangkan model berbasis fisika untuk desainnya. Efek ini dipelajari melalui eksperimen flume dengan prototipe struktur berskala, eksperimen lapangan di lakukan di Kota Demak (Indonesia), pemodelan morfodinamika 1D (dengan model XMgrove, dikalibrasi dengan pengukuran lapangan), dan penginderaan jauh.

Model digunakan untuk memprediksi kekuatan struktur dan dikembangkan untuk fenomena gelombang dan arus. Eksperimen flume menunjukkan cara untuk mengoptimalkan desain struktur. Skenario pemodelan dengan XMgrove menunjukkan bahwa lokasi struktur yang optimal bergantung pada lokasi, dan bahwa di Demak struktur dibatasi oleh tingkat penurunan tanah yang besar. Metode skala besar untuk menemukan lokasi restorasi potensial juga dikembangkan dan diterapkan di Bangladesh.

Dengan demikian, perangkat berbasis fisika, bersama dengan metode pemetaan yang disajikan dalam tesis ini, membuka jalan untuk mengoptimalkan dan menggeneralisasi upaya restorasi mangrove.

Contents

1. Introduction

Timbulsloko is a small fishermen village in the Demak province of North Java, Indonesia. The only way to reach the village is a narrow earth road that diverges from the highway, and enters a small community formed by brick houses and stands of nasi goreng.

As the path approaches the coast, wide surfaces of water surround it at both sides, transforming the road into an artificial peninsula. Unfinished concrete houses line up along the road, which is the only emergent ground.

Timbulsloko was not always inundated by the sea. Old colonial Dutch maps show that a hundred years ago this coastal area was a mangrove forest, formed by tree species tolerant to salt water. However, the forest was almost fully converted into aquaculture ponds during the course of the 20th century.

Uncontrolled groundwater extraction in the nearby city of Semarang caused ground sinking at a regional scale, up to 16 cm/year[174]. As the coastal area sunk, the tide was able to penetrate through the excavated ponds, and eroded their bunds away. Now the whole area is flooded, and during spring tide the sea can also enter the houses.

Unfortunately, Timbulsloko is not alone. 30% of the world's mangrove forests have been lost in a 50-year period[45], mostly to aquaculture and agriculture. The wellbeing of coastal communities is intrinsically linked to the health of the mangroves[1,55], and unsustainable deforestation has consequently thrown many coastal communities back to poverty[165].

1.1. Why is mangrove loss so harmful?

Mangrove forests are natural barriers against coastal hazards for millions of people all over the world[98]. Since mangroves grow at the interface between sea and land, they act as a buffer against cyclones and storms by attenuating waves and currents, and trapping floating debris[155,46,55,144,138]. Worldwide, coastal protection benefits of mangroves exceed 65 billion USD per year[98].

Their coastal protection role is even more relevant in view of climate change, since mangrove ecosystems mitigate both its causes and effects, as shown in Figure 1.1. Mangroves capture CO_2 from the atmosphere, and accumulate it as carbon in their branches, trunks and roots[103]. Moreover, as waves and currents slow down through the forest, any particles carried in the water column, such as nutrients or sediment, will deposit on the ground[170,85]. Sediment and organic-matter accumulation allowed mangroves to keep up with rising sea levels during the last 10,000 years, in contrast with unvegetated areas that sunk under the sea[125].

Unsustainable land conversion removes the previous functions, exposing coastal communities to coastal hazards and sea level rise. For instance, unvegetated shores in Colombia retreated 3-15 times

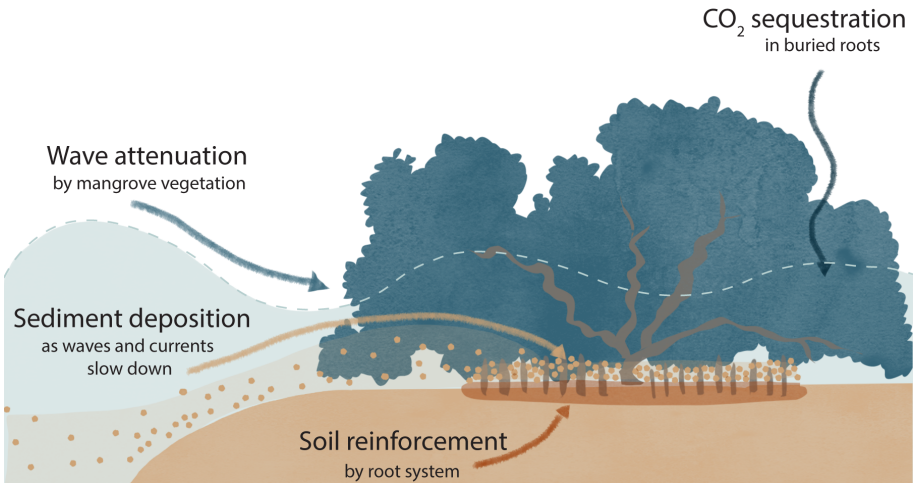

Figure 1.1: Diagram illustrating climate change mitigation by mangroves. Mangroves absorb carbon from the atmosphere, and use it as building material for their roots, branches and leaves. Their root systems reinforce the soil, which hinders sediment erosion inside the forest. Moreover, mangroves attenuate waves and currents, resulting in the deposition of sediment particles transported by the flow. The combination of sediment and organic matter accumulation increases the ground elevation, which can compensate for rising sea levels.

more than mangrove sites with equivalent wave exposure[127], and more fatalities occurred at areas without mangroves during the tsunami of 2004[144].

In view of the negative consequences of mangrove loss, numerous large-scale planting schemes have attempted to restore damaged mangrove coastlines. Only 51.3% of the reported efforts survived[15].

1.2. Why can't we simply plant the mangroves back?

Planting can help recovering areas with low seedling availability, but it can only succeed if the coastal area remains suitable for mangroves[79]. Mangroves prevail at depositional, intertidal areas with freshwater input and low wave action[42]. They can tolerate tidal flows, but different mangrove species require different levels of salinity and tidal inundation[161]. If natural or human interventions alter those conditions, the habitat should be restored to enable mangrove establishment[79] and their long-term survival.

Diagnosing the cause(s) of mangrove loss is thus the first step for rehabilitation[79,84]. For instance, excavated pond areas may become too deep for mangrove establishment, and may require hydrologic restoration through earth filling[84]. At eroding coastlines, the loss of habitat prevents mangrove colonization, and erosion mitigation measures should be applied to restore the habitat[169].

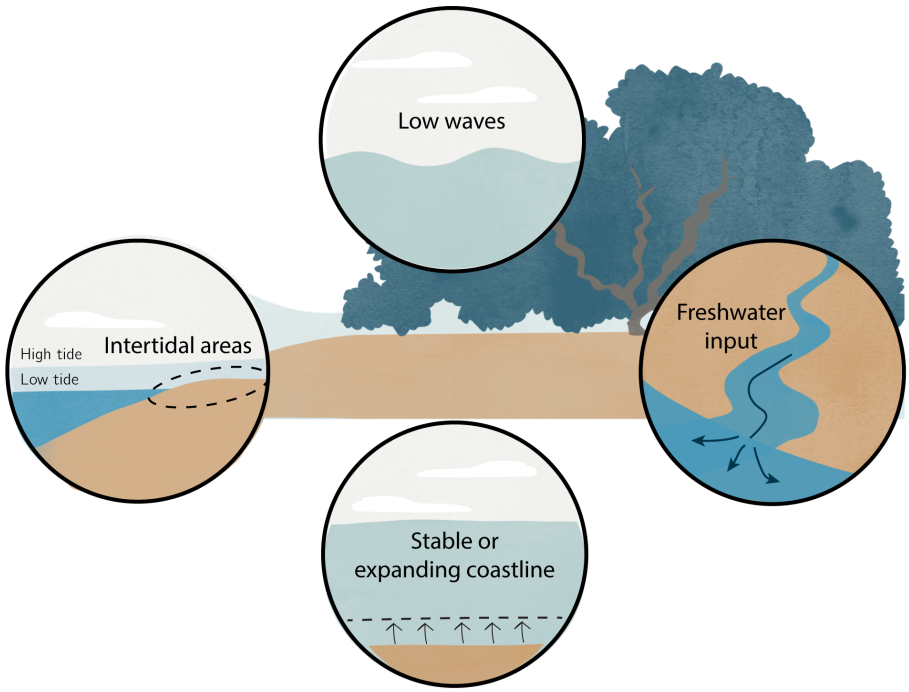

Figure 1.2: Diagram illustrating mangrove habitat requirements. Mangroves grow at intertidal areas with low wave action and sufficient freshwater input. Coastline retreat, due to flooding or erosion, causes vegetation mortality and reduces the mangrove habitat.

1.3. How can we restore eroding-mangrove coastlines?

Coastline retreat can be due to several reasons, which involve processes at several spatial and time scales. Changes in the coastal morphology depend on the input of sediment by sources (such as rivers), on the loss of sediment into sinks (like sand mining), and on the occurrence of relative sea level rise. Variations in the global climate (such as increasing storminess, or larger precipitation) can also influence how sediment is spatially distributed by waves and currents along the coast.

Locally, shoreline retreat can be triggered if human or natural interventions disrupt the balance between erosive and accretive processes[169]. Mangroves prevent erosion, and their deforestation exposes the coast to larger sediment stirring by waves and currents, as illustrated in Figure 1.3 (a-c). When erosive processes deepen the coast a feedback loop starts - larger water depths enable the propagation of higher waves towards the shore, which erode the bed even further. Mangrove removal and local subsidence in Demak have thus led to coastline retreat rates up to 215 m/year[86].

Bamboo and brushwood structures are built to mitigate erosion at degraded mangrove coastlines[168,131,169,30,165,108] in which former mangrove areas have become subtidal and thus unsuitable for mangroves. The structures emulate the effect of the lost mangrove vegetation; they are placed parallel to the coastline to attenuate waves, favoring sediment accumulation behind them, and recovering the bed elevation needed for vegetation establishment[169] (Figure 1.3, d). This concept was inspired on land reclamation works done in

the Wadden Sea over centuries[168]. The structures are made of wood since they are designed to degrade naturally after a few years, once the mangrove forest is restored[40].

Demak was the site of a pilot study for brushwood structures between 2014-2020[40,168]. The structures built in the pilot consisted of bags of brushwood held in place by vertical bamboo poles. Their width varied between 0.7-1.5 m in the wave direction, and their volumetric porosity ranged between $n \approx 0.5-0.9$, where n is defined as the ratio of the fluid volume to the total volume. The effect of the structures on the sea bed was monitored monthly throughout the project, which provided useful insights on their performance.

Structure maintenance was found essential to cause sediment accretion[36]. The bags of brushwood were often damaged by wave action and shipworms, and if not replaced early enough, the degraded structures had a negligible effect on the morphology. Furthermore, although the structures caused sediment deposition locally, and mangrove establishment was observed episodically, they did not stop coastline retreat nor led to mangrove restoration in the long term[36].

1.4. How can we improve restoration success using structures

Improving future designs requires investigating several factors. Firstly, design tools are necessary to optimize the structure performance. The structures built in Demak were not tailored to the local conditions due to the lack of design rules to do so, which may have contributed to their failure. Developing design tools requires quantify-

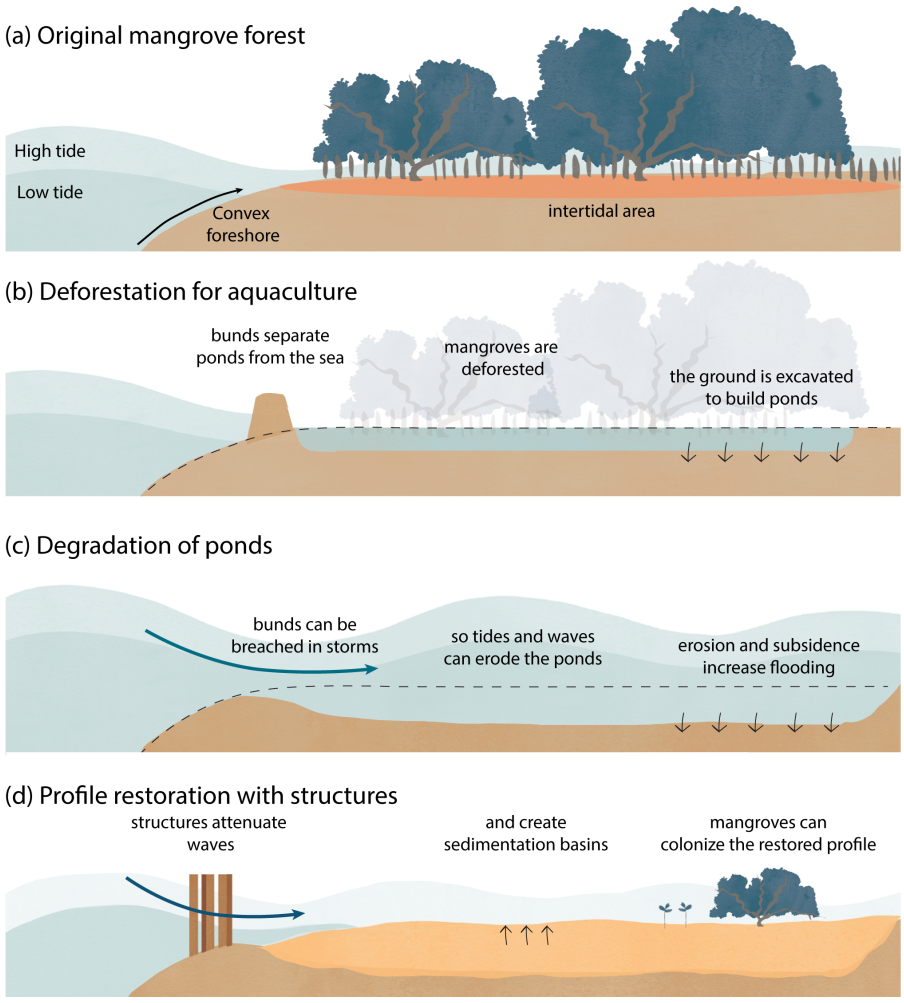

Figure 1.3: Diagram showing the stages of mangrove degradation in Demak and mangrove restoration using bamboo and brushwood structures. (a) Healthy mangrove fringes are (b) deforested and excavated to build ponds for shrimp farming. (c) The bunds separating the ponds from the sea can be breached, which exposes ponds to erosion by tides and waves propagating from the sea - a problem that is exacerbated by subsidence. (d) Mangroves cannot colonize subtidal areas and bamboo and brushwood structures are thus built to increase the bed levels and aid mangrove restoration.

ing how bamboo and brushwood structures affect currents, waves, and sediment transport. Such tools would enable finding the designs that successfully mitigate coastline retreat for different boundary conditions. The outcome of the pilot study also suggested that structures without brushwood - formed by the larger bamboo poles only - would require less maintenance.

Secondly, structures should be designed considering not only the physical processes, but also the mangrove ecology. Avoiding shoreline retreat is only one of the various requirements for mangrove restoration. Seedling availability is the first condition for natural recruitment, and once a seedling strands at a mudflat during low tide[120], wave action should remain mild while the seedling is still growing as it could otherwise be toppled over[12]. The previous limits for mangrove establishment have been investigated by exposing seedlings to currents in the laboratory[12], but their values likely vary under waves and with varying sediment properties in the field. Knowledge of the physical thresholds for Demak would enable to design structures that do not only stabilize the coast, but also create the windows of opportunity required by mangroves.

Thirdly, the natural system can offer valuable lessons on how to design the structures. In Demak mangroves have successfully grown naturally behind cheniers[156], which are large intertidal sand lenses that function like natural breakwaters. Investigating the effect of cheniers on the morphodynamics can thus provide a target to produce with the structures.

The BioManCO project was created to investigate the three previous topics. Its name stands for “Bio-morphodynamic modelling of mud-mangrove coastlines”, and it is formed by 3 PhD students

(the project structure is shown in Figure 1.4). This dissertation focuses on the first topic, on how structures influence waves, currents, and sediment transport. Celine van Bijsterveldt investigated mangrove ecology in Demak, which required finding the physical conditions required by mangroves and testing if those were satisfied in Demak[18]. Silke Tas studied the morphodynamics of cheniers, to understand what drives their sheltering presence on the coast[147].

This thesis thus elaborates on the study of the permeable bamboo and brushwood structures, but its conclusions are linked to mangrove ecology and chenier dynamics in the last two chapters.

1.5. How can we improve bamboo structure designs?

Waves and currents transport sediment across the coastal system. Predicting how structures influence the coastline position thus requires understanding how they affect their surrounding flow. Bamboo and brushwood structures exert resistance (drag) forces to incoming currents[101], which deflect the flow towards areas of less resistance[16]. Waves reflect at the front of the structures, and lose energy as they propagate through them, which shelters the coast from wave action[169].

Wave dissipation by permeable structures also depends on the drag forces acting on the brushwood and bamboo poles[32,97], which are often represented using an empirical bulk drag coefficient. This bulk drag coefficient has been thoroughly investigated for relatively sparser vegetation canopies[97,58], and measured for dense bundles of

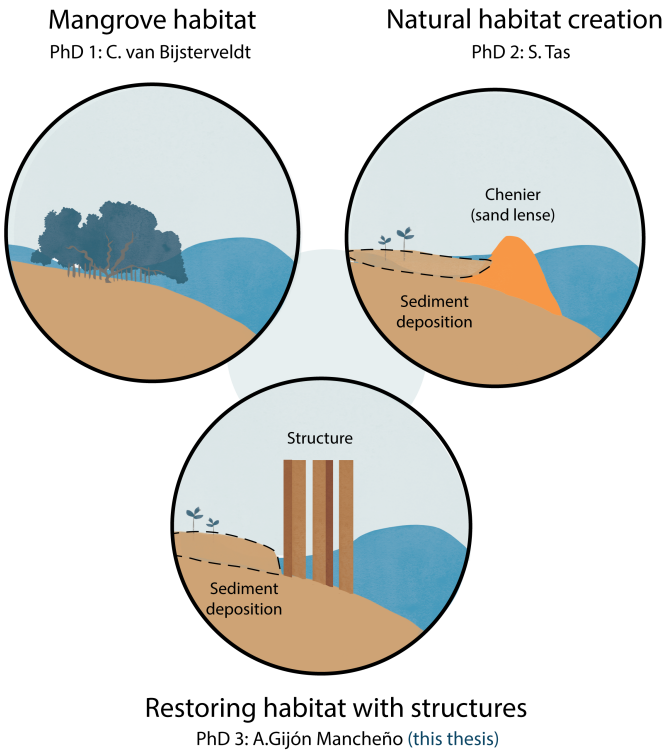

Figure 1.4: This dissertation is part of the BioManCo project, formed by 3 PhD students: (1) Celine van Bijsterveldt, investigating mangrove ecology, (2) Silke Tas, studying the migration of cheniers (sand lenses that shelter the coast, creating conditions suitable for mangrove colonization), and (3) Alejandra Gijón Mancheño, researching how to produce the natural mangrove habitat using permeable structures. This dissertation corresponds with block (3).

brushwood[33].

Brushwood structures in Demak required the replacement of their brushwood filling once or twice per year, due to its rapid degradation under wave action. Bamboo structures without brushwood could thus be alternative structure designs with lower maintenance requirements. However, drag coefficients derived from brushwood could only be applicable for bamboo-only structures if the bamboo poles are similarly placed - very densely and homogeneously arranged. With anisotropic bamboo pole placements, the hydraulic conditions and the bulk drag coefficients of the structures would differ.

The differences between structure configurations depend on several physical processes that influence the bulk drag coefficient. Smaller spacings in the wave direction cause sheltering on downstream poles, which reduces the drag forces acting on them and wave dissipation per pole[176,38]. Conversely, reducing the pole spacing laterally (perpendicularly to the waves) can be a strategy to accelerate the wave-driven flow and increase wave dissipation[44]. However, we lack models to predict the bulk drag coefficient outside of the tested range of brushwood geometries. Furthermore, a systematic comparison of which bamboo structure designs maximize wave dissipation is missing.

Once the wave height reduction through the structures is known, the next step is evaluating how this wave attenuation affects sediment transport. However, wave transformation through brushwood structures has been investigated but not linked to the coastal morphology. Wave attenuation rates of 50-60% have been reported as sufficient to lead to mangrove expansion[168]. Nevertheless, differ-

ent coastal systems (with varying sediment properties) may react differently to identical wave conditions. Identifying the suitable design for each case study thus requires implementing the effect of the structures on waves into a morphodynamic model.

This dissertation consequently aims to derive tools for bamboo structure design in several steps:

1. developing predictive methods to estimate the resistance exerted by bamboo structures in currents,
2. developing predictive methods to predict wave reflection and dissipation by bamboo structures,
3. investigating the effect of these structures on sediment transport and on the coastline position for the case of Demak,
4. and lastly, deriving a mangrove mapping methodology to find new locations where mangroves could also be restored.

These objectives are followed by conducting field experiments in Indonesia in collaboration with Universitas Diponegoro (Indonesia), and laboratory experiments, numerical modelling and spatial analysis at TU Delft (the Netherlands). The research activities are described and elaborated upon in five chapters:

CHAPTER 2 develops a physics-based model to predicts the forces acting on a bamboo structure in a current. The model is validated with data collected in the laboratory, and against data from the literature.

CHAPTER 3 describes flume experiments designed to investigate the forces acting on a bamboo structures under waves. The labora-

Chapter 2
Effect of structures on currents

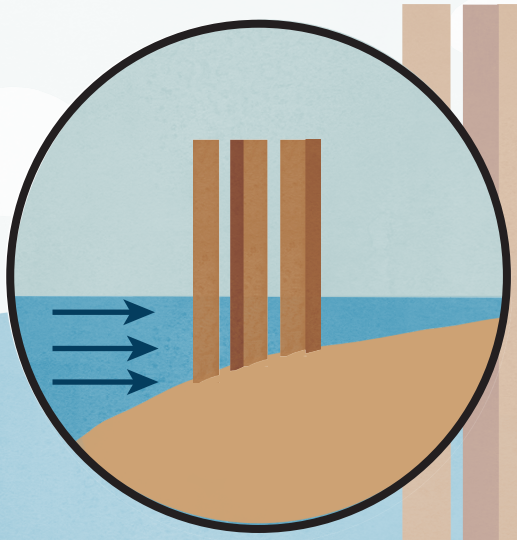

Chapter 3
Effect of structures on waves

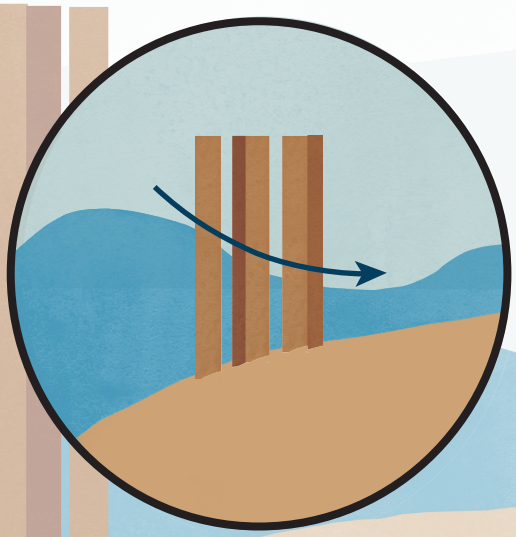

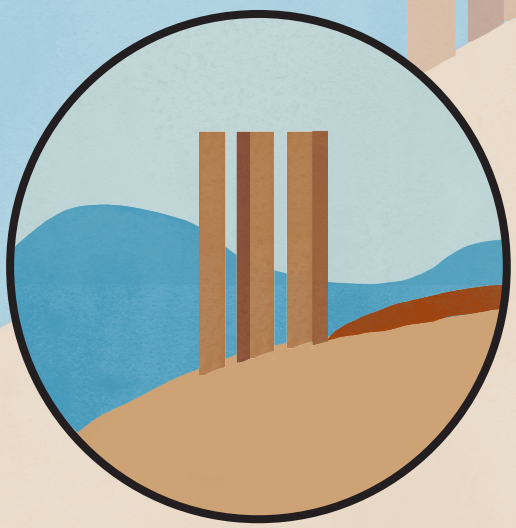

Chapter 4
Effect of structures on sea bed

Chapter 5
Mapping mangrove opportunities

tory measurements provide empirical parameters for wave attenuation, and give insights on how to design bamboo structures without brushwood.

CHAPTER 4 characterizes the physical conditions around the coastline of Demak, based on two field campaigns conducted in 2017 and 2018. The field data were used to validate a process-based morphodynamic model, which was applied to investigate which designs can maximize coastline expansion.

CHAPTER 5 derives a methodology to find mangrove establishment opportunities at a countrywide scale, which is applied to the coastal system of Bangladesh.

CHAPTER 6 synthesizes the different chapters of the thesis, discussing how optimal structure designs may change at other sites, and presenting the limitations of this study and recommendations for future research work.

2. Effect of structures on currents

2.1. Introduction

Bamboo and brushwood structures affect local currents, which in turn influences sediment transport and mangrove habitat creation. However, the interaction between structures and currents has received limited attention in existing designs. Predicting the impact of the bamboo structures on spatial flow patterns requires quantifying the resistance forces exerted by the structures. The aim of this chapter is thus to develop a design tool to calculate this resistance, which could be implemented in large-scale flow models to optimize bamboo structure designs. The content of this chapter is included in the following publication:

A. Gijón Mancheño, W. Jansen, W.S.J. Uijttewaal, J.C. Winterwerp (2021) Predictive model of bulk drag coefficient for a nature-based structure exposed to currents. Scientific Reports 11.

2.2. Resistance by cylinders in a current

When a current encounters a bamboo structure, flow separation causes form drag forces on the individual poles, and the associated energy dissipation. The drag forces depend on the local flow velocities inside the structure, and on an empirical drag coefficient, c_D. The drag coefficient varies with object geometry (surface roughness, cross-sectional shape, height compared to the water depth), and with the flow regime, usually classified as viscous or turbulent[136]. For a circular cylinder in turbulent flow, c_D takes a value of approximately 1[136].

The local flow velocities will vary depending on the arrangement of the poles. On one hand, the presence of the poles reduces the available cross-sectional fluid area ("blocking the flow"), which increases the velocities between the elements due to mass conservation. This effect is referred to as blockage[43,123,3,57]. On the other hand, downstream elements may be sheltered by upstream wakes, which reduces the velocities acting on them[52,83,137,177,176]. This second effect is referred to as sheltering. The relative importance of these two processes will depend on the flow conditions, and on the size and distance between the poles, as illustrated in Figure 2.1 (c).

Blockage and sheltering effects are often combined into a single fitting parameter, the bulk drag coefficient, $c_{D,b}$. Several authors have referred the drag forces measured inside cylinder arrays to bulk channel velocities U_b, and used $c_{D,b}$ as a fitting factor. The subscript b indicates that c_D is referred to the bulk velocities, estimated as $U_b = Q/(wh)$, where Q is the total flow discharge, w is the channel width, and h the water depth. $c_{D,b}$ values from Tanino and Nepf[146]

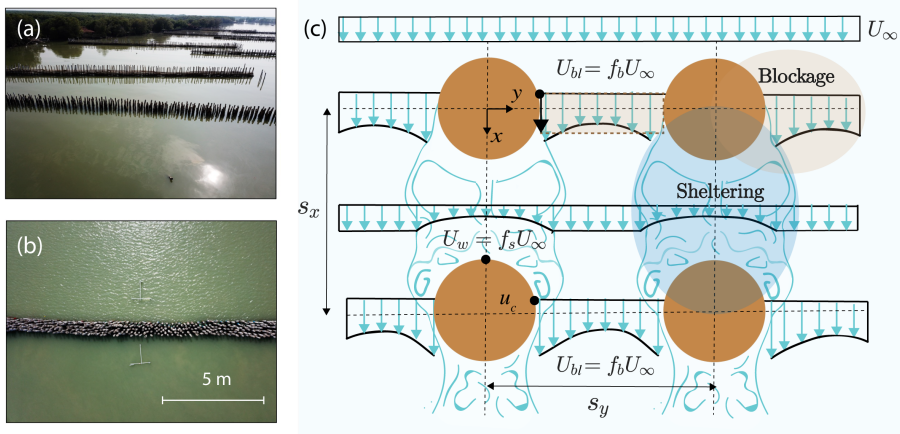

Figure 2.1: (a) Pictures of bamboo structures built by the Indonesian Ministry of Marine Affairs and Fisheries in Demak, Indonesia. The structures are formed by arrays of bamboo poles with a diameter of $d \approx 0.15$ m, distributed over widths between approximately 0.7-1.5 m in the streamwise direction. Their volumetric porosity ranges between $n \approx 0.5 - 0.9$. (b) Top view of one of the structures. Both drone pictures are courtesy of S.A.J. Tas. (c) Sketch representing the effects of blockage and sheltering on the local flow velocity (blue arrows) at the scale of the bamboo poles of a structure (solid brown circles), inspired by Etminan *et al.*[43] and Zdravkovich[176]. Incoming flow velocities U_∞ accelerate to U_{bl} between the cylinders, an effect known as blockage. Behind the first row of cylinders, velocities reduce to U_w due to sheltering effects. The relative magnitude of these effects depends on the streamwise and lateral or spanwise spacing of the cylinders (s_x and s_y, respectively).

and Tinoco and Cowen[150] are shown in Figure 2.2 (a) as a function of $Re_p = U_p d/\nu$, where Re_p is the the Reynolds number based on the average pore velocities, U_p, and the cylinder diameter d. The pore velocity is defined as the velocity averaged over the pore space, which can be estimated as $U_p = U_b/n$, where U_b is the bulk velocity and n is the volumetric porosity[146].

Application of the coefficients of Figure 2.2 (a) into designs is not straightforward, due to the variability of $c_{D,b}$ for a fixed value of Re_p. For instance, $c_{D,b}$ varies between $1-10$ for $Re_p = 1,000$ in Figure 2.2 (a), and referring the drag forces to the bulk velocities does not enable distinguishing how blockage and sheltering effects led to different drag values for the same Re_p. A number of authors have proposed relating the drag forces to the pore velocities U_p, and considering these as representative of the flow conditions inside the structures[146,134,150]. The concept of pore velocity is based on mass conservation over the fluid volume, and it is illustrated in Figure 2.2 (b). The drag coefficient based on U_p reduces the variability of the fitted drag to $c_{D,p} = 1-4$ for the conditions of Figure 2.2 (a) with $Re_p = 1,000$, but it still leaves too much uncertainty in the choice of the coefficient.

This led to the research work of Etminan *et al.*[43], who suggested that the variability in drag measurements could be due to the local velocities between cylinders exceeding U_p, and causing consequently higher bulk drag coefficients. Their modelling work showed that the drag forces were better represented by the constrained velocities, calculated from mass conservation at a cross-section of the flow, as shown in Figure 2.2 (c). Etminan *et al.*[43] modelled conditions that corresponded with natural vegetation, with a volumetric porosity

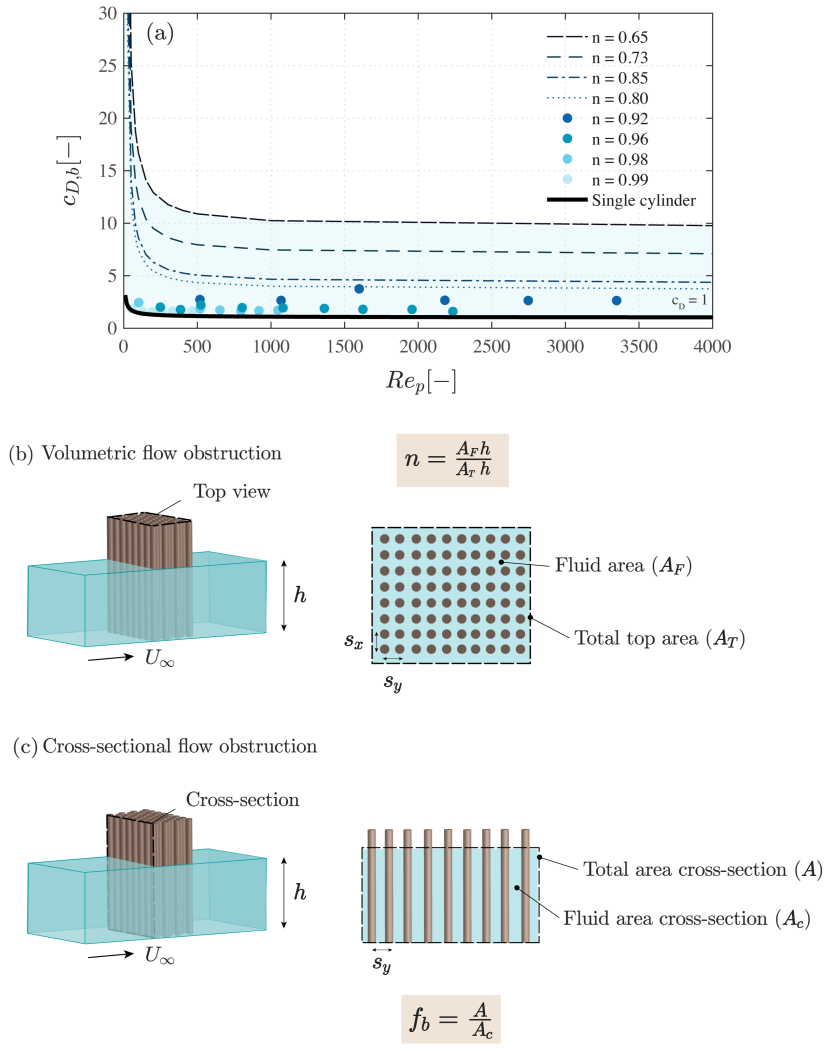

Figure 2.2: (a) Bulk drag coefficient values ($c_{D,b}$) from the literature (including blockage and sheltering effects) as a function of the Reynolds number based on the cylinder diameter and pore velocities (Re_p). The shaded blue area shows the region of variation of $c_{D,b}$ for arrays of emergent and smooth circular cylinders in a current, fully covering the cross-section of the flume. The data points are obtained from Tinoco and Cowen[150], and the fit lines from Tanino and Nepf[146]. (b) Definition of the volumetric porosity n, given as the ratio between the fluid volume, $V_F = hA_F$ over the total volume $V = hA$. (c) Definition of the blockage factor f_b, given as the ratio between the total cross-sectional area A of the array and the constrained flow section, A_c.

of $n = 0.78 - 0.98$, where sheltering effects were very small. Incorporating sheltering effects in drag predictions may be necessary for the bamboo structures, which are relatively less porous with $n = 0.5 - 0.9$.

A number of (semi)empirical approaches have been derived to integrate sheltering effects in the predictions of the drag forces. Blevins[20] developed an expression for the velocity deficit on a downstream cylinder based on wake similarity laws, for two cylinders in cross-flow. Higher turbulence levels are expected inside an array with more elements[106], and this factor has been observed to influence the rates of velocity decay behind cylinders[38]. Eames *et al.*[38] developed a model for the velocity deficit behind a cylinder that also included the effect of ambient turbulence, but the application of this model for the bamboo structures would require a separate module to calculate turbulent production between the cylinders.

Meftah and Mossa[96] developed a model for the flow velocity reduction inside sparse cylinder arrays, relating the velocity deficit behind the cylinders with the geometrical properties of the array, and with an empirical turbulent mixing length scale l. However, due to the lower porosity of the bamboo structures, and the smaller relative distance between their poles, blockage is likely to influence turbulence production, which sets the bamboo structures outside the range of calibrated data and the assumptions of the previous models. Quantifying sheltering effects for the bamboo structures thus requires adapting the existing approaches.

We consequently present a physics-based model to predict the drag forces acting on emergent cylinder arrays exposed to currents, which provides a direct relationship between cylinder arrangement

and $c_{D,b}$. The velocities inside the arrays are estimated using a blockage factor, based on mass conservation, and a sheltering factor, based on the wake flow model developed by Eames *et al.*[38]. Since the model of Eames *et al.*[38] requires knowledge of the ambient turbulence intensity, we expand the turbulence model of Nepf[106], including a turbulence production term by flow expansion, as done by Mossa *et al.*[102], and the effects of blockage and sheltering in the wake production term.

This model focuses on the local physical processes inside the structures, and it computes the bulk hydrodynamic forcing using the incoming flow velocity and flow depth as input parameters. In order to calculate the effects of the structures on the surrounding flow field (such as backwater effects or changes in the flow direction in coastal regions), the equations of the model could be built in standard free surface flow models that solve for those processes.

The development of the bulk drag model is presented in the next section. Following its derivation, the model is tested against force measurements from random cylinder arrays by Tanino and Nepf[146] and Tinoco and Cowen[150], and from regular cylinder arrays by Jansen[68]. The experiments of Jansen[68] are described in Appendix A. The model behaviour is also explored for different cylinder configurations. Finally, the model sensitivity to different input parameters is investigated, and the model is applied to optimize future structure designs.

2.3. Physics-based model for cylinders in a current

The model consists of (1) an adapted drag formulation for closely-packed cylinder arrays, including blockage and sheltering, and (2) a turbulent kinetic energy balance, necessary to quantify sheltering. The turbulence model builds on the formulation suggested by Nepf[106] for vegetation canopies, and incorporates a turbulence production term by flow expansion, and an extended drag formulation in the wake production term. The steps to derive the equations are presented below.

2.3.1. Drag model

The drag forces experienced by an array of cylinders, per unit mass, can be calculated as:

$$F_d = \frac{1}{2} c_D a |U| U \tag{2.1}$$

where c_D is the drag coefficient of a single cylinder, which can be estimated using the empirical expression of White[166], given by:

$$c_D = 1 + 10 Re^{-2/3} \tag{2.2}$$

where Re is the Reynolds number based on the cylinder diameter and the depth-averaged local flow velocity U. a is the projected plant area per unit volume, defined by Nepf[106] as:

$$a = \frac{dh}{hs^2} = \frac{d}{s^2} \tag{2.3}$$

with d being the cylinder diameter, s the spacing between cylinders, and h the water depth.

The main unknown in Equation 2.1 is the local flow velocity U. If a cylinder array is sufficiently sparse, the local flow velocity could be assumed equal to the depth-averaged incoming flow velocity, U_∞, either measured or calculated with a free surface flow model. For denser configurations, the velocity will change as the flow propagates through the array due to (1) flow acceleration between the elements (blockage), and (2) flow deceleration due to the sheltering effects of upstream rows of cylinders. Both effects are illustrated in Figure 2.1 (c). The changes in flow velocity are included by multiplying U_∞ by a blockage factor, f_b, and a sheltering factor, f_s:

$$U = f_b f_s U_\infty \tag{2.4}$$

Inserting both factors in the expression for the drag force results in Equation 2.5:

$$F_d = \frac{1}{2} c_D a |U| U = \frac{1}{2} c_D a f_b^2 f_s^2 |U_\infty| U_\infty = \frac{1}{2} c_{D,b} a |U_\infty| U_\infty \tag{2.5}$$

where the changes in velocity have been incorporated in the bulk drag coefficient, $c_{D,b} = c_D f_b^2 f_s^2$. This expression provides a direct relationship between the drag coefficient of a single cylinder, c_D, and bulk drag coefficients $c_{D,b}$ measured for cylinder arrays in laboratory experiments. Predicting the drag force thus depends on determining the values of f_b and f_s.

The blockage factor f_b can be estimated based on mass conservation through a row of cylinders[43], considering that the velocity will increase as the same flow discharge travels through the smaller section between the elements:

$$U_\infty A = U_c A_c = f_b U_\infty A_c \tag{2.6}$$

where the total frontal area is $A = hs_y$, and s_y is the distance between cylinders perpendicular to the flow, center-to-center (see Figure 2.1). Subtracting the frontal area of the cylinders from the total area gives the available flow area, A_c:

$$A_c = hs_y - hD = h(s_y - d) \tag{2.7}$$

Here we are assuming that the water depth is the same just upstream and in between the cylinders. Solving for f_b in Equation 2.6 results in Equation 2.8, see also Etminan *et al.*[43]:

$$f_b = \frac{hs_y}{h(s_y - d)} = \frac{1}{1 - d/s_y} \tag{2.8}$$

The sheltering factor f_s can be estimated from the wake flow model by Eames *et al.*[38], which predicts the velocity deficit behind a cylinder as a function of the distance downstream of the cylinder, s_x, the cylinder diameter, the local turbulent intensity I_t, and the drag coefficient:

$$\frac{U_\infty - U_w}{U_\infty} = \frac{c_D d}{2\sqrt{2\pi} I_t s_x} \tag{2.9}$$

where U_w is the velocity in the cylinder wake, U_∞ is the incoming flow velocity, and I_t is the mean turbulent intensity, defined as $I_t = \sqrt{k}/U_\infty$[106,146]. k represents the turbulent kinetic energy per unit mass, with $k = 1/2(\overline{u'^2} + \overline{v'^2} + \overline{w'^2})$, where u', v', and w' are the instantaneous velocity fluctuations in the streamwise, lateral, and vertical direction respectively, and where the overbar denotes time averaging. The turbulent velocity fluctuations are defined as the difference between the instantaneous velocities and their mean value over a measurement period. Here we consider the depth-averaged value of the turbulent intensity, in view of the uniformity

of the turbulent properties over the vertical observed inside emergent arrays[106].

Equation 2.9 was developed assuming turbulent flow. Viscous effects decrease the velocity deficit[38], with the reduction factor being given by:

$$f_{Re} = \sqrt{\frac{Re}{Re_t}} \tag{2.10}$$

where Re_t is the lowest Reynolds number corresponding to fully turbulent wake flow. Laminar effects are included in the wake flow model by multiplying the velocity deficit of Equation 2.9 by the reduction factor f_{Re} for $Re < Re_t$, where the the turbulent Reynolds number is assumed equal to $Re_t = 1,000$. This value is based on the observation that although a wake starts becoming turbulent at $Re_t \sim 200$, drag coefficient measurements usually become constant at Reynolds numbers beyond $Re_t \sim 1,000$, e.g. as shown in Figure 2.7 of Sumer and Fredsoe[136]. The influence of varying Re_t on the model results is investigated in Section 2.4.

Defining the sheltering factor as $f_s = \frac{U_w}{U_\infty}$, and including f_{Re} and the bulk drag coefficient in the definition of the velocity deficit results in Equation 2.11:

$$f_s = \frac{U_w}{U_\infty} = 1 - f_{Re}\frac{c_{D,b}d}{2\sqrt{2\pi}I_t s_x} = 1 - f_{Re}\frac{c_{D,b}d}{2\sqrt{2\pi}(\sqrt{k}/U_\infty)s_x} \tag{2.11}$$

Equation 2.9 also assumes that the downstream cylinder is placed inside the ballistic spreading region of the wake. The ballistic regime occurs for a downstream distance $s_x < L/It$, where L is the integral length-scale of turbulence, and it is characterized by a rapidly decaying velocity deficit, and by a linear increase of the wake width with downstream distance. Inside the cylinder arrays,

the length scale development is limited by the downstream spacing, resulting in $L < s_x$. Considering that turbulent intensity measurements of Jansen[68] varied between $I_t = 0 - 0.8$ inside cylinder arrays with $n = 0.64 - 0.9$, this would result in $L < s_x/It$. This is a reasonable general assumption for the bamboo structures, since their porosity varies in a similar range. If the poles were sparsely placed, there would be a transition from ballistic to diffusive spreading of the wake. Eames *et al.*[38] also developed expressions for turbulent flow under the diffusive regime, which could be used in place of Equation 2.9.

In the opposite case of very high pole densities, there may be a point where the elements are so closely-packed that vortex shedding is inhibited by the presence of the neighboring cylinders. Considering an analogy with a cylinder placed close to a solid boundary, vortex shedding would not take place for spanwise spacings smaller than $s_y/d < 1.3$[136], causing a decrease of the drag coefficient that would not be reproduced by the expression of White[166]. The application of the present model is thus restricted to $s_y/d > 1.3$.

2.3.2. Balance of turbulent kinetic energy

Application of Equation 2.11 requires predicting the turbulent kinetic energy. This is calculated by expanding the model developed by Nepf[106], based on a balance between turbulence production and dissipation:

$$P_w \sim \epsilon \tag{2.12}$$

where P_w is the turbulent production rate and ϵ is the dissipation rate. For a dense cylinder array, k is produced by (1) generation in the wakes of the cylinders[106], and (2) shear production by the jets

formed between the elements[102]. The total turbulence production term, P_w, consequently has two parts:

$$P_w = P_{w1} + P_{w2} \tag{2.13}$$

We assume that for dense cylinder arrays these two terms are much higher than turbulence production by shear at the bed, based on observations by Nepf[106] for sparse arrays. This assumption is further tested in Section 2.4.

The first term in Equation 2.13, P_{w1}, represents turbulence production at the wakes, and can be estimated as the work done by the drag force times the local flow velocity:

$$P_{w1} = \frac{1}{2} c_D a |U| U^2 = \frac{1}{2} c_D a f_b^3 f_s^3 |U_\infty| U_\infty^2 \tag{2.14}$$

The second term, P_{w2}, represents turbulence generation due to flow expansion[102], and can be estimated from the Reynolds shear stresses:

$$P_{w2} = \overline{u'v'} \frac{\partial u}{\partial y} \tag{2.15}$$

where the overbar denotes time averaging. The loss in mean kinetic energy E_c due to flow expansion is equal to:

$$\Delta E_c = \frac{1}{2} U_\infty^2 \left(\left(\frac{A}{A_c} \right)^2 - 1 \right) = \frac{1}{2} \left(f_b^2 - 1 \right) U_\infty^2 \tag{2.16}$$

where the energy loss due to flow expansion, ΔE_c, is modelled using the Carnot losses. Assuming that the mean kinetic energy is transformed into turbulent kinetic energy E_t, and assuming isotropic turbulence, gives Equation 2.17:

$$\frac{1}{2} \left(f_b^2 - 1 \right) U_\infty^2 = \frac{3}{2} \overline{u'u'} \tag{2.17}$$

Equation 2.17 enables expressing the normal Reynolds stress as a function of the incoming flow velocities and the blockage factor:

$$\overline{u'u'} = \frac{1}{3}\left(f_b^2 - 1\right) U_\infty^2 \tag{2.18}$$

The Reynolds shear stress is estimated as $\overline{u'v'} = R\overline{u'u'}$, where the correlation factor R is given a constant value of 0.4 based on observations of Nezu and Nakagawa[107]. This value was derived for open channel flow conditions and is assumed acceptable as a first approximation, but it could vary inside a cylinder array. This is explored further in Section 2.4.

The velocity gradient is estimated from the velocity difference between the side of the cylinders (dominated by blockage) and the wake of the cylinders (dominated by sheltering) resulting in Equation 2.19:

$$\frac{\partial u}{\partial y} \approx \frac{U_\infty(f_b - f_s)}{\frac{1}{2}s_y} \tag{2.19}$$

Substitution into Equation 2.15 gives Equation 2.20:

$$P_{w2} = \frac{2}{3}R(f_b - f_s)(f_b^2 - 1)\frac{U_\infty^3}{s_y} \tag{2.20}$$

The dissipation term, ϵ, is estimated as:

$$\epsilon \sim k^{3/2} l^{-1} \tag{2.21}$$

The characteristic turbulent length scale l is limited by the surface-to-surface separation between the elements in the flow direction, $l = min(|s_x - d|, d)$. This differs from the expression developed by Nepf[106], who used the diameter as representative of the size of the eddies. We assume that in closely-packed cylinder arrays the spacing between cylinders may be smaller than the diameter,

$|s_x - d| < d$, which would limit turbulence development. The maximum value of l is set equal to the cylinder diameter. Here we also assume that for the dense cylinder arrangements, the spacing between cylinders is considerably smaller than the water depth, hence turbulence generated by bed friction is negligible.

Balancing the production and dissipation of turbulent kinetic energy results in Equation 2.22:

$$\frac{k^{3/2}}{l} \sim |U_\infty| U_\infty^2 \left(c_D a f_b^3 f_s^3 + \frac{4R}{3 s_y} (f_b^2 - 1)(f_b - f_s) \right) \tag{2.22}$$

Taking the cubic root at both sides and introducing the scale factor α_1 gives Equation 2.23:

$$\frac{\sqrt{k}}{U_\infty} = \alpha_1 \left(c_D f_b^3 f_s^3 a l + \frac{4}{3} R (f_b^2 - 1)(f_b - f_s) \frac{l}{s_y} \right)^{1/3} \tag{2.23}$$

Where α_1 is a coefficient of $\mathcal{O}(1)$, which is given a default value of $\alpha_1 = 1$. The sensitivity of the model to different α_1 and R values is explored in Section 2.4.

k can be calculated by solving Equation 2.23 iteratively, using the incoming upstream velocity U_∞ and the geometric characteristics of the structure, s_y, s_x, d and a, as an input. This enables determining the sheltering factor, $f_s = U_w / U_\infty$ from Equation 2.11. The blockage factor $f_b = (1 - d/s_y)^{-1}$ can also be calculated from the geometric properties of each configuration. Both coefficients can be then combined to predict the bulk drag coefficient, with $c_{D,b} = c_D (f_s)^2 (f_b)^2$. Deriving $c_{D,b}$ with the present approach relies on the assumption that the changes in water depth through the structure are small. This is a reasonable assumption given the short length of the bamboo structures in the streamwise direction, which varies between 0.7-1.5 m (see Figure 2.1 b). Longer structures that

experience non-negligible changes in flow depth and velocity should be discretized, and the bulk drag coefficient should be calculated separately for the different sections. The model assumptions are discussed further in the following section.

2.4. Model results and discussion

In this section we firstly present the model validation, and investigate how turbulence production and sheltering vary under different configurations. We then explore the model sensitivity to several input parameters, and finally apply the model to investigate structure design optimization.

2.4.1. Model validation

The performance of the model is tested against drag measurements for regular, staggered and random emergent cylinder arrangements from the literature. A summary of the conditions tested in the different studies is shown in Figure 2.3. The regular configurations, also denoted as in-line arrangements, consist of rows of cylinders where the downstream elements are always in one line in the streamwise direction (see configurations 1-6 tested by Jansen[68] in Figure A.1 b of Appendix A). In the staggered arrangements, for every row the downstream elements are shifted laterally so that they are located at the center line of upstream elements, as also shown in configuration 7 of Figure A.1 (b). The random arrangements were obtained by distributing the cylinders using a random number generator, see Tanino and Nepf[146].

In Figure 2.4 we compare the model predictions for the cases

Source	Arrangement	s_x/d [–]	s_y/d [–]	d [m]	n [–]	U_∞ [m/s]	$c_{D,b}$ [–]
Tinoco and Cowen[149]	Random	2.39	2.39	0.0025	0.92	0.16	2.85
		2.89	2.89	0.013	0.96	0.22	1.90
		3.67	3.67	0.006	0.98	0.22	1.83
		4.83	4.83	0.003	0.99	0.20	1.64
Tanino and Nepf[145]	Random	2.29	2.29	0.006	0.80	0.05	2.63
		1.98	1.98	0.006	0.85	0.06	2.71
		1.71	1.71	0.006	0.73	0.03	3.61
		1.50	1.50	0.006	0.65	0.03	3.93
Jansen[68]	Regular	∞	1.50	0.040	0.33	0.40	8.98
		3.00	1.50	0.040	0.79	0.40	6.19
		1.50	1.50	0.040	0.64	0.40	4.44
		∞	3.00	0.040	0.66	0.40	2.67
		3.00	3.00	0.040	0.90	0.40	1.59
	Staggered	3.00	3.00	0.040	0.82	0.40	1.93

Figure 2.3: Validation data for emergent cylinder arrays.

of Figure 2.3 with two other approaches used in the literature to define the bulk drag coefficient. Figure 2.4 (a) shows the bulk drag coefficient calculated from the pore velocities (based on mass conservation over the fluid volume). Figure 2.4 (b) shows the drag values derived from the blockage factor (based on mass conservation over a cross-section, from Equation 2.7). Figure 2.4 (c) shows the results of the present model, which includes both blockage and sheltering effects.

Using the pore velocities to estimate the bulk drag results in a general under-estimation of the drag coefficients (Figure 2.4 a). The blockage factor provides better estimates of the bulk drag for random arrays, but it cannot reproduce the sheltering effects observed at regular arrangements with different streamwise separations (Figure 2.4 b). The present model, including both sheltering and blockage, successfully reproduces the bulk drag for regular

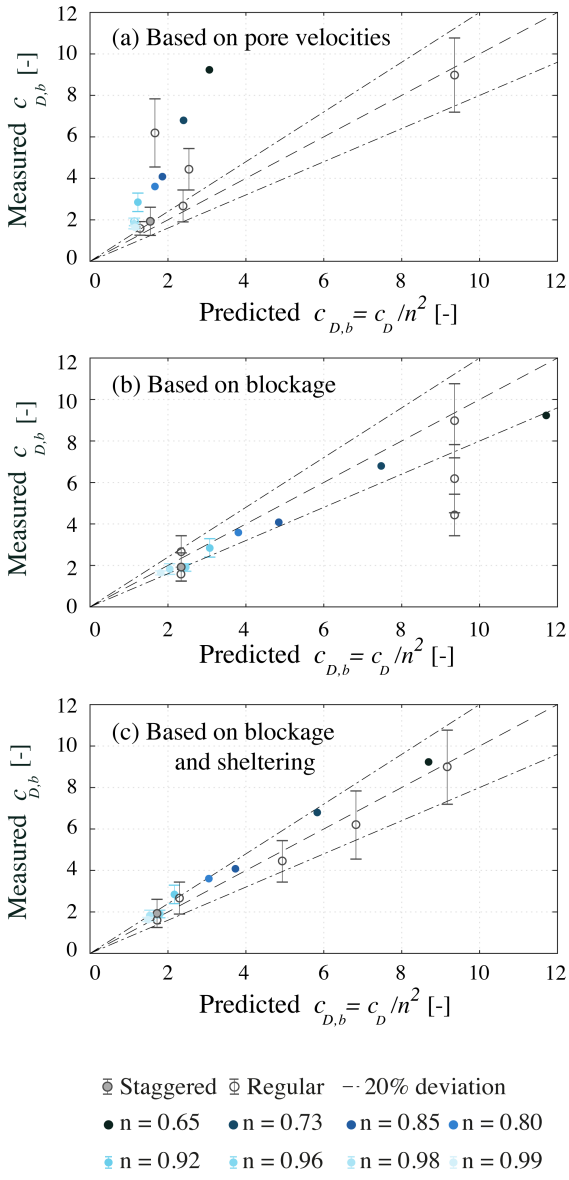

Figure 2.4: Predictions versus bulk drag coefficient ($c_{D,b}$) measurements for random cylinder arrays, by Tinoco and Cowen[150] and Tanino and Nepf[146], and versus measurements for regular and staggered arrangements by Jansen[68]. Plot (a) shows $c_{D,b}$ values calculated from the pore velocities, (b) from the blockage factor and (c) from the present model. Vertical bars show the estimated measurement error.

configurations, and it also provides a slight improvement for the random arrangements (Figure 2.4 c). The model displays a general tendency to overestimate the bulk drag of staggered and random configurations, which could be due to changes in the flow direction through such configurations.

Random and staggered arrangements have been associated to similar bulk drag coefficients in the literature[74], which were higher than for regular configurations[115,81,82,132]. Schoneboom *et al.*[132] attributed the larger drag for staggered arrays to the more tortuous water flow through them. The present model assumes that the flow propagates only in the streamwise direction, and that it does not experience changes in direction. This assumption still yielded good results with the validation, especially for the densest configurations. This is expected because as the element density increases most of the total volume is occupied by cylinders. Less room for varying the spatial arrangement results in similar drag forces for regular and random arrays.

Although the model does not include changes in water level through the structures, it could still reproduce the measurements of Tanino and Nepf[146] and Tinoco and Cowen[150], conducted with array lengths of 0.99 m and 2.84 m, respectively. This assumption may not hold for longer cylinder arrays over a fixed horizontal bed. Under those conditions the water depth could experience significant changes through the structure, which should be taken into account in bulk drag predictions. However, since the bamboo structures have a short length in the streamwise direction, such cases are beyond the scope of the present work.

2.4.2. Influence of spacing on hydrodynamic parameters

Once validated, the model is applied to investigate the influence of the distance between elements on turbulence production and sheltering, and to evaluate how the previous effects translate into different $c_{D,b}$ values. Figure 2.5 shows the turbulent kinetic energy, sheltering factor, and bulk drag coefficient calculated for three values of spanwise spacing, $s_y/d = 1.5, 3$ and 10, for streamwise separations between $s_x/d = [1, 100]$.

The turbulent kinetic energy, shown in Figure 2.5 (a), is expressed as a ratio to the turbulent kinetic energy produced by bottom friction, k_o. Turbulence generation at the bed is based on the friction velocity with $k_o = c_{f,b}U_\infty^2$, where $c_{f,b} = 0.001$ corresponding to a smooth bottom. Overall, the levels of turbulence inside cylinder arrays are considerably higher than for a bare bed. The turbulent kinetic energy increases with smaller spanwise spacing s_y/d, since blockage increases the drag forces, their work, and the shear production term. The largest spanwise spacing, $s_y/d = 10$, produces relatively lower values of k, but these are still between $k = [4 - 20]k_o$.

The turbulence levels also vary as a function of the streamwise spacing, decreasing their values for the lowest s_x/d, since sheltering effects cause a strong reduction of the turbulence production terms. Higher streamwise separations reduce sheltering effects, and increase turbulence production up to a relative maximum around $s_x/d \sim 2$. Beyond the maximum, the larger streamwise separations are associated to a lower number of cylinders per unit volume, a smaller projected area a, and less production of turbulent kinetic energy per unit mass.

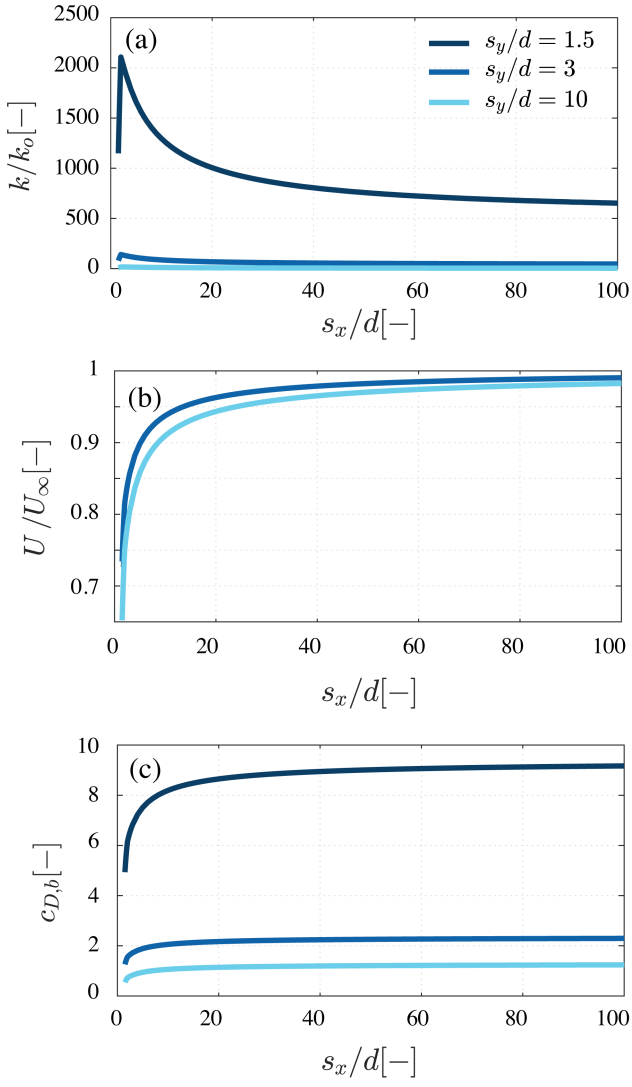

Figure 2.5: Model results for (a) the turbulent kinetic energy k compared to the turbulent production of a bare smooth bed, k_o, for (b) the sheltering factor, U_w/U_∞, and for (c) the bulk drag coefficient $c_{D,b}$ as a function of the streamwise spacing s_x and spanwise spacing s_y between cylinders compared to the cylinder diameter, d. The lines for $s_y/d = 1.5$ and $s_y/d = 3$ are on top of each other in plot (b). The figure shows that smaller spanwise spacings s_y result in higher turbulence production and faster wake recovery. The smaller sheltering effects combined with larger flow acceleration result in higher bulk drag coefficients for low s_y.

These trends are also visible in the sheltering factor, shown in Figure 2.5 (b), as the velocity deficit over a cylinder is inversely proportional to the level of ambient turbulence. The velocity deficit is consequently smaller for low s_y/d values. Since the velocity reduction is also inversely proportional to s_x/d, sheltering effects are less pronounced for higher s_x/d values. This results in the bulk drag coefficients, shown in Figure 2.5 (c), being governed by the blockage factor for $s_x/d > 15$, and by both sheltering and blockage for lower s_x/d values.

2.4.3. Sensitivity analysis

The present model depends on the values that are assumed for the parameters α_1, R and Re_t. The model sensitivity to changes around their default values is explored in Figure 2.6.

The scale factor α_1 is varied between 0.5 and 1.5 in Figure 2.6 (a). The lower limit of $\alpha_1 = 0.5$ is associated to a relatively low turbulence production, which in turn increases the velocity deficit on downstream elements. This results in considerable sheltering effects up to $s_x/d \sim 40$. $\alpha_1 = 1$ increases turbulence production and reduces the velocity deficit, causing appreciable sheltering effects up to $s_x/d \sim 20$. The higher value of $\alpha_1 = 1.5$ provides comparable results to $\alpha_1 = 1$. A more precise assessment of α_1 would require measurements of turbulence production and dissipation inside different cylinder configurations. Since laboratory measurements presented in the literature show that sheltering effects can be evident at a downstream distance of $s_x/d = 15$[83], it is concluded that $\alpha_1 = 1$ provides reasonable predictions of the sheltering effect. As shown in Figure 2.6 (b), the model results display low sensitivity

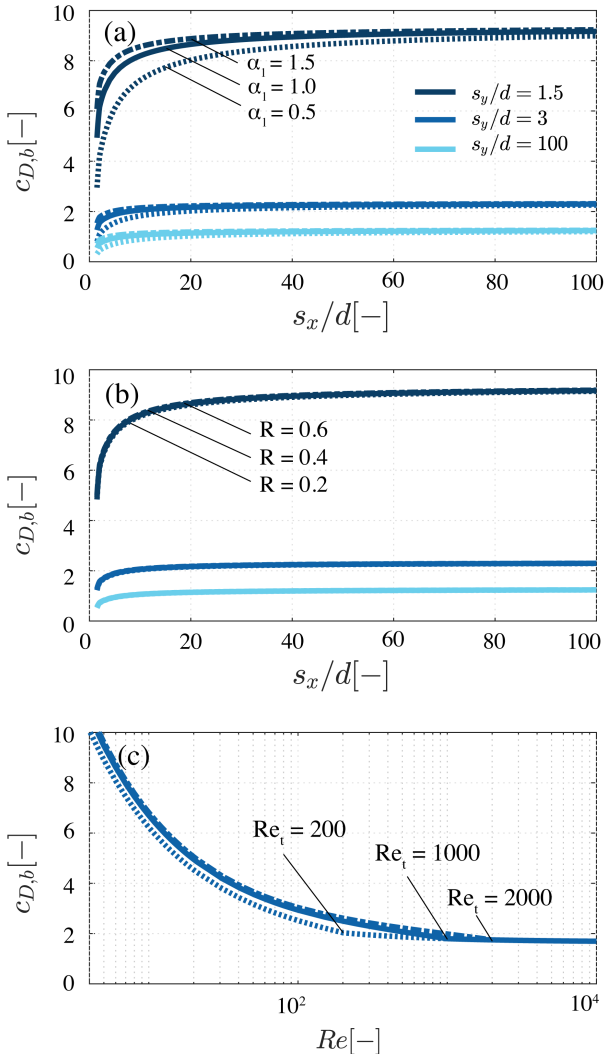

Figure 2.6: Sensitivity of the modelled bulk drag coefficient $c_{D,b}$ to varying values of (a) the scale factor α_1 and (b) the correlation factor R, as a function of the streamwise spacing s_x and spanwise spacing s_y between cylinders compared to the cylinder diameter, d. Plot (c) shows the influence of the limit for turbulent flow, Re_t, on the bulk drag predictions for $s_y/d = 1.5$ as a function of the Reynolds number Re.

to variations of the factor R, since the shear production term P_{w2} has a relatively lower weight on the total turbulence production in comparison with the wake production term P_{w1}.

The influence of Re_t on the bulk drag predictions is illustrated in Figure 2.6 (c). Lower values of Re_t result in stronger sheltering effects and smaller bulk drag coefficients. The largest difference between the three tested values was observed for $Re = 200$, where $c_{D,b} = 2, 2.5$, and 2.6 for $Re_t = 200, 1,000$, and $2,000$, respectively. An accurate evaluation of this threshold would require force and velocity measurements inside cylinder arrays with Reynolds numbers varying in the previous Re_t range. Considering the large diameter of the bamboo poles, the Reynolds numbers in the field are most likely to be of the order of $Re \sim 10,000$. This implies that the Re_t threshold will not affect significantly the drag force predictions for the structures.

2.4.4. Drag maximization

The choice of pole configuration, in terms of element spacing s_x/d and s_y/d, is thus essential to assess the bulk drag and the resistance provided by a structure. This is conceptualized in Figure 2.7.

Figure 2.7 illustrates the computed bulk drag coefficient for different combinations of the dimensionless spacing s_x/d and s_y/d. The lowest value of s_y/d is limited to 1.3 since, as previously discussed, below that value the expression of White[166] may not be valid. We also include solid black lines showing configurations with the same volumetric porosity. Figure 2.7 shows that a structure with a porosity of 80% can have an average bulk drag coefficient

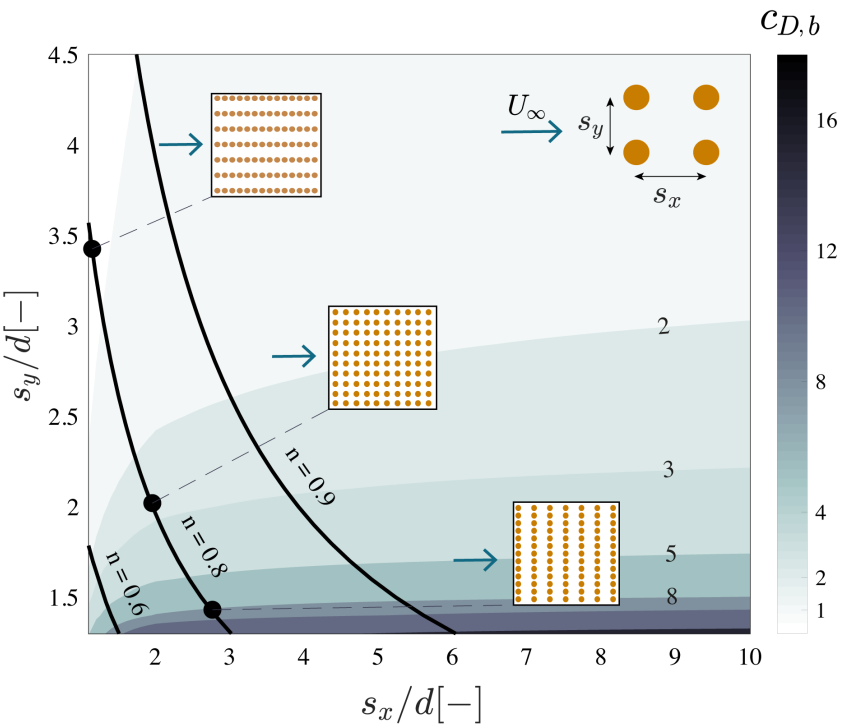

Figure 2.7: Predicted bulk drag coefficient as a function of the streamwise spacing s_x and spanwise spacing s_y between cylinders compared to the cylinder diameter, d. The diagram shows lines of constant volumetric porosity n. Three examples of regularly spaced configurations with constant porosity of $n = 0.8$ but varying streamwise/spanwise spacing are given. Flow direction relative to the arrays is indicated by a blue arrow (from left to right). The diagram shows that given a constant porosity, higher drag values can be obtained for smaller spanwise spacings s_y and longer streamwise spacings s_x.

between $c_{D,b} = 1 - 10$ depending on the element placement.

The highest bulk drag coefficients are associated to rows of cylinders with a small spanwise spacing s_y/d, which enhances blockage, and a large streamwise spacing s_x/d, so that downstream rows experience less velocity reduction. For instance a regular structure with 80% porosity and a spanwise spacing of $s_y/d = 1.4$, would have a streamwise spacing of $s_x/d = 2.8$. This would result in a bulk drag coefficient of $c_{D,b} = 8$. If the same number of elements were placed in a uniform setting, with $s_x/d = s_y/d = 2$, this would led to a much lower bulk drag coefficient of $c_{D,b} = 3$.

Placing the rows in a staggered manner could reduce sheltering effects, but even assuming negligible sheltering, a spanwise spacing of $s_y/d = 2$ would lead to a bulk drag coefficient of $c_{D,b} = 4$ (with $c_{D,b} = c_D f_b^2$). A similar effect could be achieved with a random configuration, but predicting the net effect of the spatial changes in density on the drag would require more detailed knowledge of the cylinder density distribution. In a random arrangement the flow will tend to deflect to areas of low element density, but its trajectory will also depend on the length of the paths. A shorter path where the cylinder are more densely placed could lead to lower resistance than a longer and sparser alternative[122]. However, as previously discussed, for relatively denser structures, uniform and random arrangements should yield comparable forces.

The present drag model may be implemented in large scale hydrodynamic models to evaluate the impact of currents, and the associated forces, on the cylinders. This approach would enable varying the cylinder arrangement, structure length and location, and help identify parameter combinations that optimize future structure de-

signs.

Moreover, although the present model was developed for currents, it is applicable for long waves (with $KC > 100$, where KC represents the ratio of wave excursion to pole diameter) where non-stationary effects are negligible. For shorter waves (with $KC < 100$), the hydrodynamic forces also depend on additional aspects, such as inertial effects[101], or turbulence enhancement by waves[72]. The influence of wave hydrodynamics on the bulk drag coefficient is investigated further in the next chapter.

3. Effect of structures on waves

3.1. Introduction

The implementation of bamboo and brushwood structures in Demak was limited by lack of tools to predict wave transmission through the structures. Guidelines for traditional coastal infrastructure are not directly applicable for bamboo structures, as these have different hydraulic properties than structures like breakwaters or seawalls. The aim of this chapter is thus to develop tools to predict wave reflection and dissipation by bamboo structures, and to find optimum structure designs. These objectives are reached by conducting flume experiments, which enable comparing the relative performance of different structure configurations. The experimental results are also used to develop an empirical model, which can be applied to predict the wave height behind the structures. The content of this chapter is included in the following publication:

A. Gijón Mancheño, W. Jansen, W.S.J. Uijttewaal, A.J.H.M Reniers, A.A.van Rooijen, T. Suzuki, V. Etminan, J.C. Winterwerp (2021). Wave transmission and drag coefficients through dense cylinder arrays: implications for designing structures for mangrove restoration. Ecological Engineering 165.

3.2. Wave transformation through structures

3.2.1. Wave dissipation

When a wave propagates through a bamboo structure, part of its energy is reflected seawards, as shown in Figure 3.1. Wave reflection

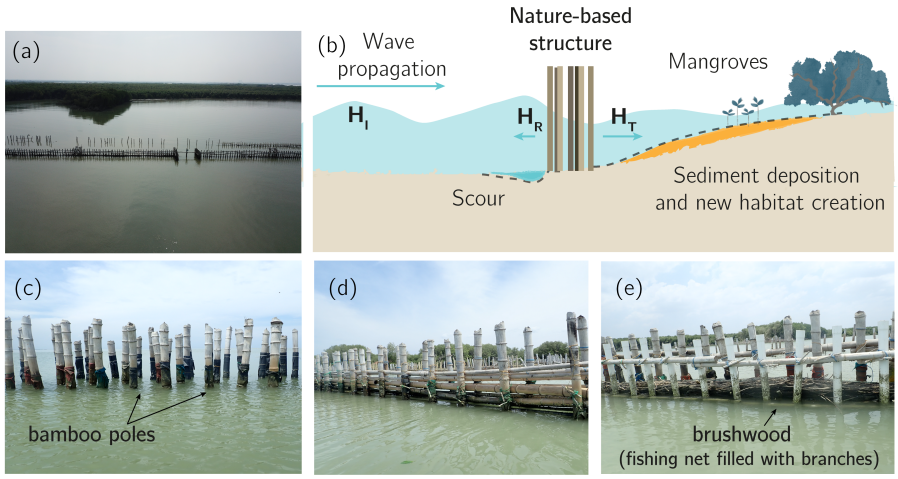

Figure 3.1: (a) Aerial view of permeable structure built in Demak, Indonesia. (b) Illustration of the concept of enhancing mangrove restoration with permeable structures. When an incoming wave H_I encounters a structure, there is a reflected wave component H_R that propagates seawards and may cause scour at the toe. Another part of the wave energy is dissipated due to drag through the structure. The smaller transmitted wave height, H_T, enhances sediment deposition, creating new potential habitat for the mangroves. The structures can have different configurations, such as (c) vertical bamboo poles, (d) vertical poles and horizontal beams and, (e) vertical poles with a brushwood filling.

increases the flow velocity in front of the structure, and enhances scour at the toe. The remaining wave energy continues travelling into the structure and exerts hydrodynamic forces on the poles. These forces consist of several parts; (1) skin friction forces, (2)

form drag forces due to flow separation behind the poles, and (3) inertia forces, associated with the acceleration of the wave-driven flow. The friction forces are often neglected, since they are much smaller than the form drag components. For a vertical cylindrical element the total in-line force F_x is often parameterized using the Morison equation[101]:

$$F_x = \int_{-h}^{\eta} \left(\frac{1}{2} \rho c_D d u|u| + \rho c_M \frac{\pi d^2}{4} \frac{\partial u}{\partial t} \right) \partial z, \tag{3.1}$$

where h is the still water depth, η is surface elevation, ρ is the water density, c_D is the drag coefficient, d is the pole diameter, u is the local horizontal flow velocity, c_M is the inertia coefficient, $\frac{\partial u}{\partial t}$ is the horizontal flow acceleration, and z is the vertical coordinate. The work done by the hydrodynamic forces over a wave cycle, ϵ_v, causes wave energy dissipation, which reduces wave transmission through the structure. For an array formed by vertical cylinders, the total work done by the horizontal in-line forces, F_x would be given by Equation 3.2:

$$\epsilon_v = \overline{\int_{-h}^{\eta} F_x u N_v} \tag{3.2}$$

Where N_v is the cylinder density per unit area.

Since the inertia force and the velocity are 90º out of phase, the wave-averaged work, ϵ_v, is dominated by the drag component of Equation 3.1. Assuming negligible wave reflection and that the velocity field can be described by linear wave theory gives Equation 3.3[32]:

$$\epsilon_v = \frac{2}{3\pi} \rho c_{D,b} d N_v \left(\frac{kg}{2\omega} \right)^3 \left(\frac{\sinh^3 kh + 3 \sinh kh}{3k \cosh^3 kh} \right) H^3 \tag{3.3}$$

Where $c_{D,b}$ is an empirical bulk drag coefficient, which includes the effect of disturbances of the velocity field by the cylinder array, k

is the wave number, ω is the wave frequency, g is the acceleration of gravity and H is the wave height.

A horizontal beam exposed to waves experiences form drag forces in both the horizontal and vertical direction, since the water particles move in elliptical motions. Suzuki *et al.*[141] expanded the expression for horizontal structures by incorporating the work done by the vertical drag forces, resulting in Equation 3.4:

$$\epsilon_v = \frac{2}{3\pi}\rho c_{D,b} d N_v \left(\frac{kg}{2\omega}\right)^3 \left(\frac{\sinh^3 kh + 3\sinh kh}{3k\cosh^3 kh} + \frac{\cosh^3 kh - 3\cosh kh + 2}{3k\cosh^3 kh}\right) H^3 \tag{3.4}$$

The additional vertical dissipation term implies that changing the element orientation from vertical to horizontal may increase wave dissipation. The vertical velocities, drag forces, and associated dissipation, are relatively larger in deeper water conditions, characterized by a large ratio of the water depth to the wave length. The vertical velocities and their effects on wave dissipation are smaller in shallow water, which produces comparable wave dissipation rates by vertical and horizontal cylinders. The effect of element orientation on wave dissipation has been included in analytical and numerical models, e.g. Suzuki *et al.*[141], but it was not tested in previous laboratory studies.

3.2.2. Drag coefficients

Predicting wave dissipation by the bamboo structures relies on the knowledge of the drag coefficient.[97,142]. However, most literature has investigated the drag values for a single cylinder[72,50,112], or for sparse cylinder arrays with volumetric porosities above $n =$

0.78[128,5,54,6,58,113,28,44,116].

The drag and inertia coefficients derived in those studies are often expressed as a function of the KC number, defined as the ratio of the wave excursion ξ to the cylinder diameter d[72]. KC represents the relative importance of the drag and inertia force components, with $0 < KC \ll 20 - 30$ corresponding to inertia-dominated cases, and $KC > 20 - 30$ associated with drag-dominated conditions[136]. For $KC > 100$ the drag coefficients converge with the values of steady flow, and the KC-dependency disappears[72,50,112].

The drag coefficients for arrays are often calculated by fitting Equation 3.1 with velocities either measured upstream from the array, or estimated assuming a harmonic flow[128,5,54]. Neglecting the hydrodynamic changes inside the arrays has resulted in considerable variability in the drag values found in literature, with values ranging between $c_{D,b} = [0, 16]$ for emergent rigid cylinders[128,25,54].

The variability in $c_{D,b}$ for emergent arrays has been mostly attributed to the processes of sheltering and blockage. Sheltering takes place when downstream rows are exposed to the wake of upstream elements, and they thus experience lower drag forces[54,21,83]. Sheltering in wave driven flows depends on whether the wave excursion is long enough to reach the next neighbouring cylinder[54,140], as illustrated in Figure 3.2 (e-g). When the ratio between flow excursion, ξ, and streamwise separation, s_x, is between $1 < \xi/s_x < 5-7$, sheltering is a function of the excursion length compared to the spacing[54,140]. For larger ξ/s_x ratios sheltering relates to the dimensionless spacing between cylinders s_x/d[54], analogously to uniform flow. Other studies found that in relatively sparse emergent vegetation, sheltering effects can often be neglected, and that the drag

forces are well described by blockage. Blockage refers to flow acceleration through a cross-section of the vegetation[43,123,44], which causes higher drag forces on the cylinders.

Previous studies often focused on one of the two processes, which dominated the drag forces in their application. However both sheltering and blockage may influence the drag forces for the bamboo structures. The influence of the distance between elements on sheltering and blockage is illustrated in Figure 3.2 (a-d), with a smaller lateral spacing s_y increasing blockage effects, and a smaller streamwise separation s_x increasing sheltering effects.

In view of the processes of sheltering and blockage, we hypothesize that structures with small lateral distance s_y (increasing blockage) and a relatively longer streamwise separation s_x (decreasing sheltering) could maximize the forces, and thus the energy dissipation per element. This type of geometric arrangement could consequently reduce the material costs of a bamboo structure. However, excessively low lateral spacings could increase wave reflection and scour, hindering structure stability[169]. An optimum structure should thus maximize wave dissipation while minimizing reflection.

3.3. Laboratory experiments and model for structures

In order to explore the effect of cylinder arrangement and orientation on wave transformation and the drag coefficients, structure prototypes consisting of arrays of cylinders were tested in a wave flume. We measured wave transformation, hydrodynamic forces and flow velocities inside the arrays. The experiments focused on

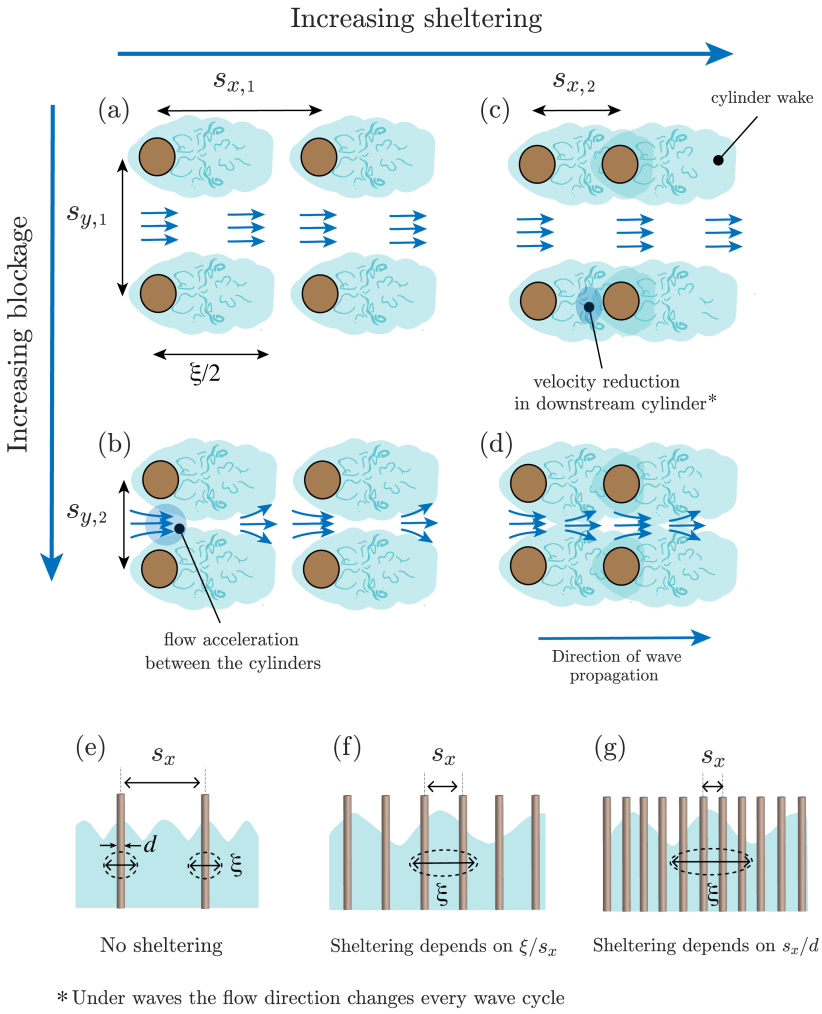

Figure 3.2: Sketch illustrating sheltering and blockage for cylinder arrays. (a) Situation where the cylinders do not interfere with each other. (b) For small lateral spacings, flow acceleration increases the forces on the elements (blockage). (c) For small streamwise spacings, downstream cylinders are in the wake of upstream elements, which reduces the forces on them (sheltering). (d) Situation with both blockage and sheltering. (e-g) Sheltering under waves depends on the wave excursion ξ compared to the spacing between cylinders s_x and their diameter d. (e) If $\xi/s_x < 1$, the wake of one element does not reach neighbouring cylinders. (f) If $1 < \xi/s_x < 5-7$ sheltering depends on ξ/s_x[54,140]. (g) If $\xi/s_x > 5-7$ sheltering depends on s_x/d[54].

regular or in-line configurations, since they simplify the analysis of the physical processes. Random arrangements would provide higher drag variability under comparable conditions, and besides this, regular arrangements may provide more efficient designs that maximize blockage and minimize sheltering.

Due to the properties of the bamboo structures, the experiments enabled investigating processes not addressed in other studies. We tested cylinder arrays that were denser and shorter (in the direction of wave propagation) compared to most experiments in the literature, since fully developed canopy conditions cannot be directly applied to the bamboo structures. Wave reflection was also analyzed, given the higher density of the structures compared to natural vegetation, and the potential detrimental effects of reflection on structure stability. The set-up of the experiments and the data analysis are explained in the following sections.

3.3.1. Data collection

Wave generation

The laboratory experiments were conducted in a wave and current flume at Delft University of Technology. The flume is 40 m long, 0.8 m wide and 0.8 m high. A wave generator with an active reflection compensation system was placed at one side of the flume and a wave absorber at the opposite end. We prescribed the second-order steering of the wave maker for all tests. Monochromatic waves were generated, with a water depth of $h = 0.55$ m, a wave height of $H = 0.13$ m, and periods of $T = 1, 1.25, 1.5, 1.75, 2$, and 3 s, respectively.

Physical model

The generated waves propagated through a frame with cylinders placed in the middle of the flume, as illustrated in Figure 3.3 (a). The physical model consisted of a grid of 0.76 x 0.76 m, where aluminum cylinders could be introduced in different arrangements. The elements were held together by a top and a bottom plate, as shown in Figure 3.3 (c). The cylinder diameter was $d = 0.04$ m for all experiments. The tested configurations are illustrated in Figure 3.4. The configurations are named based on their lateral spacing (D, for dense with $s_y = 1.5d$, and S, for sparse with $s_y = 3.0d$), their streamwise spacing s_x (also D or S), the number of rows, and the cylinder arrangement (with R for regular or in-line, and T for staggered).

Most experiments were conducted with vertical cylinder arrangements, starting with one single row, and adding additional rows in successive experiments. For a smaller subset of configurations, indicated by an asterisk in Figure 3.4, the frame was also placed horizontally in the flume to analyze the effect of cylinder orientation on wave transformation.

Instrument set-up

For each cylinder arrangement we measured the water surface elevation, flow velocities and the forces acting on individual cylinders. The locations of the instruments are presented in Figure 3.3 (a). All the instruments were measuring throughout each experiment with a frequency of 100 Hz.

The water surface elevation was measured with capacitance-type wave gauges; two in front of the structures (WG1 and WG2 in Fig-

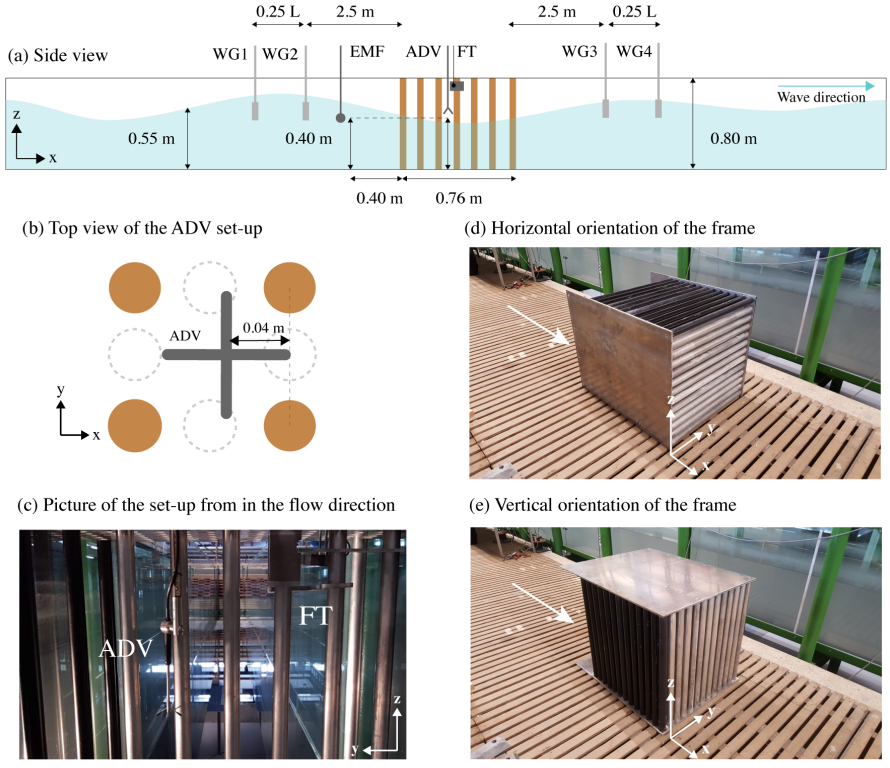

Figure 3.3: (a) Side view of the instrument set-up in the flume. (b) Detail top view of the placement of the ADV inside the physical model. (c) Picture of the ADV and the load cell (FT) inside the flume. (d) Picture of the frame outside of the flume in the horizontal orientation. (e) Picture of the frame outside of the flume in the vertical orientation

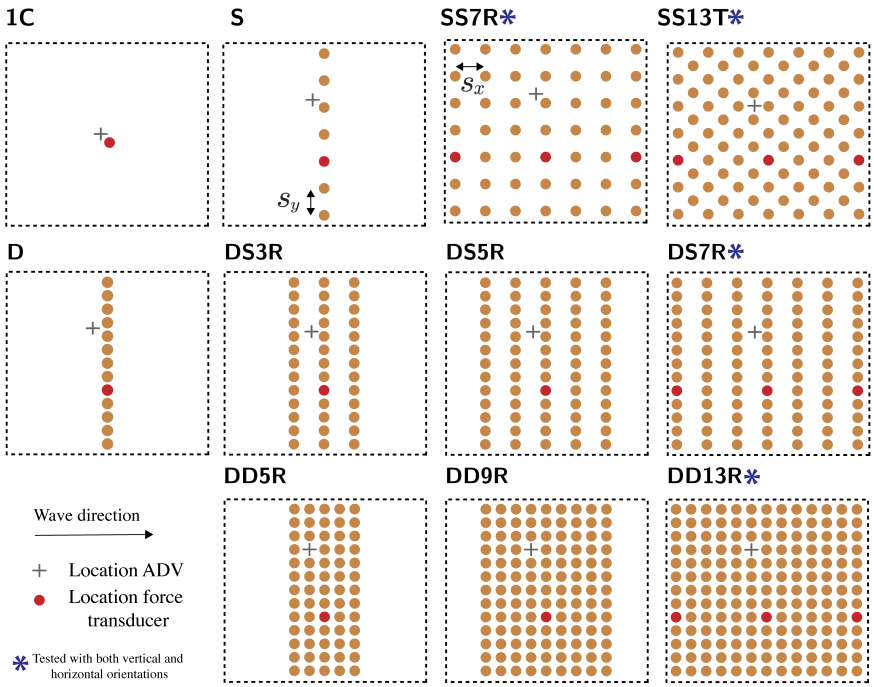

Figure 3.4: Configurations tested in the experiments. The location of the ADV for each configuration is indicated by a grey cross, while the location of the force measurements is shown with a red dot. The configurations were tested by starting with a single row, and adding downstream rows in successive steps. All the configurations were tested with a vertical orientation, while the configurations with blue asterisks were also tested with a horizontal cylinder orientation.

ure 3.3), and two behind it (WG3 and WG4 in Figure 3.3). The output of the wave gauges was in volts, and the surface elevation was obtained from linear regression, using separate calibration factors for each of the wave gauges. The accuracy of the gauges was 1%[59]. The separation between each pair of wave gauges was set to 0.25 times the wave length of each wave condition, for optimal wave reflection analysis[49].

An electromagnetic flow meter (EMF) was placed at a distance of 0.4 m upstream from the structure. The elevation of the EMF was changed between tests to provide velocity measurements at 3 elevations from the bed: $z = 0.15$ m, 0.25 m, and 0.4 m. The EMF measurements had an accuracy of approximately 1%[60].

The velocities inside the structures were measured with a Nortek Vectrino acoustic velocimeter (ADV), placed 0.04 m upstream from the center of a cylinder (see Figure 3.3 (c) and Figure 3.4). The elevation of the ADV was also varied between tests, and it measured the flow velocity at $z = 0.15$ m, 0.25 m, and 0.4 m. The ADV had an accuracy of approximately 1%[111].

The hydrodynamic loads acting on a single cylinder were recorded with a SCAIME load cell mounted on the upper part of the element, measuring in volts with 0.017% accuracy[130]. The load cells were calibrated using known weights, and fitting a linear relationship between weight and voltage output. The measured forces were calculated by multiplying the sensor output by the calibration factor, and by the acceleration of gravity. Force and velocity measurements were only collected for the vertical orientations, since we could not introduce the sensors inside the horizontal structures without removing multiple elements.

3.3.2. Data analysis

Wave transformation

The incoming and reflected wave components were separated with the method of Goda and Suzuki[49], using the dispersion relation for non-linear waves of Kirby[75], consistently with the second-order wave paddle steering. The method was applied to the time series of WG1 and WG2 to calculate wave reflection in front of the structure, and to the measurements of WG3 and WG4 to calculate the wave transmitted through the structure. The analysis was conducted over time intervals during which (1) the propagating wave had already reached the wave gauges but (2) its reflected component from the end of the flume had not yet arrived at WG4.

Force coefficients

The drag and inertia coefficients were determined with a least-square fit method, using the depth-averaged velocity and acceleration in Equation 3.1 to reproduce the measured forces[136]. This approach thus required reconstructing the full velocity profile from the different experiments to estimate the depth-averaged quantities.

Although the instruments were automatically synchronized by the data logger during each test, the velocity measurements at the different elevations ($z = 0.15$ m, 0.25 m, and 0.4 m) were collected during separate experiments. Combining those measurements to obtain the vertical velocity profile required correcting for the relative time shift between tests, to ensure that the velocities along the vertical coordinate corresponded with the same phase of the wave.

The time shift was calculated by maximizing the correlation

between the time series of WG2 for each test with respect to the reference case, which was taken as the test with $z = 0.15$ m. An example of the velocity measurements before and after correcting for the time shift is shown in Figure B.2 of Appendix B. A moving average was applied to the velocity time series over intervals of 0.25 s. For the velocity measurements of 1C, the mean flow component was removed using the detrend function in Matlab. The acceleration time series was computed from the time derivative of the velocities.

Prior to calculating the depth-averaged quantities, we estimated the values of the velocity and acceleration at the flume bottom $z = 0$ and at the mean water level $z = h$ to include the velocity changes throughout the whole water column. We extrapolated those values from a hyperbolic cosine fit through the measurements at $z = 0.15, 0.25$, and 0.4 m. The reconstructed velocity profiles from the EMF measurements of 1C are shown in Figure B.3 of the Appendix. The hyperbolic cosine fit was made assuming that the vertical profile can be described by the main harmonic, since we generated regular waves in the flume. We also calculated the wave spectrum for all wave conditions, and reconstructed the vertical profile by adding the velocity of each harmonic. The maximum differences were up to 2% at $z = h$.

The depth-averaged quantities were then calculated by trapezoidal integration over the vertical. A moving average was applied over intervals of 0.25 s to the force time series of the reference case, $z = 0.15$ m. The drag and inertia coefficients were determined by fitting Equation 3.1 over an interval of 4 wave periods in order to minimize spurious effects. The interval length of the moving aver-

age was varied to evaluate how it affected the fitted drag coefficients for 1C. Averaging over intervals of 0.12 and 0.37 s provided very similar values of the force coefficients, with maximum differences of -1.98 and 2.95%, respectively.

Model development

Optimal structure designs are characterized by low reflection (K_r), high dissipation (K_d) per element. We consequently present a simplified conceptual model to investigate how wave reflection and dissipation vary with different cylinder arrangements, in order to identify the most optimal designs.

Wave reflection through a single row of cylinders is calculated as a function of its lateral spacing s_y compared to the cylinder diameter d. If the cylinders are so close that they touch each other, i.e. $s_y - d = 0$, the incoming wave height is fully reflected, with $K_r = 1$. In the extreme case where the lateral separation is infinite, the reflection coefficient is zero. We consequently model wave reflection with a function of the form:

$$K_r = \frac{1}{1 + c_R \frac{s_y - d}{d}} \tag{3.5}$$

where c_R is an empirical coefficient.

Equation 3.5 provides the reflection coefficient of the first row. The energy flux entering the first row after subtracting wave reflection is thus given by $(1 - K_r^2) E_i c_{g,i}$, where $E_i c_{g,i}$ is the incoming wave energy flux seawards from the structure.

The energy dissipated due to the drag forces acting on the first row of cylinders is obtained by introducing Equation 3.3 in the wave

energy flux balance[32]:

$$\frac{\partial E c_g}{\partial x} = -\epsilon_v \tag{3.6}$$

Where x is the horizontal coordinate in the direction of wave propagation. Expressing the balance as a function of the wave height results in Equation 3.7:

$$\frac{\partial H}{\partial x} = -A_o H^3, \tag{3.7}$$

where $A_o = 8\epsilon_v/(\rho g c_g H^3)$. Solving the linear differential equation for the wave height results in Equation 3.8[32]:

$$K_t = \frac{H}{H_o} = \frac{1}{1 + \alpha s_x}, \tag{3.8}$$

where K_t is the wave transmission coefficient through the first row of cylinders, expressed as the ratio of the wave height just downstream of the row, H, to the incoming wave height, H_o. s_x represents the separation between two rows of cylinders center-to-center in the wave direction, and the damping factor α is given by $\alpha = \epsilon_v H/2\rho g c_g$.

The bulk drag coefficient used in Equation 3.3 is estimated as the product of the drag coefficient of a single cylinder, c_D, times an empirical characteristic velocity, u_c, representative of blockage and sheltering effects inside an array, and divided by the undisturbed flow velocity u obtained with linear wave theory:

$$c_{D,w} = c_D \left(\frac{u_c}{u}\right)^3 \tag{3.9}$$

The subscript w denotes that since this bulk drag coefficient is implemented in the wave dissipation term, it relates to the local velocity to the power of three. The characteristic velocity is estimated

as a function of several empirical factors:

$$\frac{u_c}{u} = f_b f_{KC} f_s, \tag{3.10}$$

where the blockage factor f_b is based on mass conservation through a cross-section of the structure[43,123,44], resulting in Equation 3.11:

$$f_b = \frac{1}{1 - d/s_y}, \tag{3.11}$$

f_{KC} is an empirical factor representing the transition of the drag coefficient between inertia and drag dominated conditions, e.g. as shown in Figure 9 of Etminan *et al.*[44].

The right term, f_s, representing sheltering effects, is computed using Equation 3.12:

$$f_s = 1 - \frac{c_s}{s_x/d} \tag{3.12}$$

Here we assume that for highly turbulent environments the velocity reduction in the wake of a cylinder is proportional to $1 - c_s/(s_x/d)$, as shown by Eames *et al.*[38] for uniform flow, where c_s is an empirical parameter dependent on the turbulent intensity. This approach has also been successfully applied to predict sheltering effects for dense cylinder arrays in currents (see Chapter 2).

Equations 4.6-3.12 estimate the wave dissipation caused by each row. The total wave reflection and dissipation rates of the structure can be calculated cumulatively row by row, by (1) firstly calculating wave reflection, (2) subtracting the reflected energy flux, and (3) calculating wave dissipation between each row and the downstream one.

3.4. Experimental and model results

3.4.1. Wave transmission

Wave transmission through the different configurations is shown in Figure 3.5 as a function of KC. The transmission coefficient K_t is defined as the ratio of the transmitted wave amplitude to the incoming wave amplitude. The transmission measurements range between $K_t = 0.4 - 1$. Overall, the transmission rates decrease for longer waves, associated with higher KC values, and for an increasing number of rows for each configuration. However, most wave height reduction takes place in the first rows of the structures.

The influence of element density on wave transmission is more pronounced than the effect of wave excursion. The densest structure, DD13R, produces the lowest transmission rates (Figure 3.5, a), and the most porous structure, SS7R, the highest transmission rates (Figure 3.5, d). Nevertheless, element arrangement plays an important role on the wave height reduction per cylinder. For instance, the configuration formed by dense rows with a relatively longer streamwise separation, DS7R, (Figure 3.5, b), has half as many elements as the least porous configuration, but their wave transmission rates are similar. The results of Figure 3.5 (b) and (d) correspond with structures that have the same number of elements, but wave transmission is higher through the staggered arrangement, SS13T, (Figure 3.5 d) than through the dense rows with a long streamwise separation (Figure 3.5 b).

Horizontal arrangements reduce wave transmission compared to vertical configurations, as shown in Figure 3.5. The additional wave height reduction is largest for the smallest KC, with horizontal

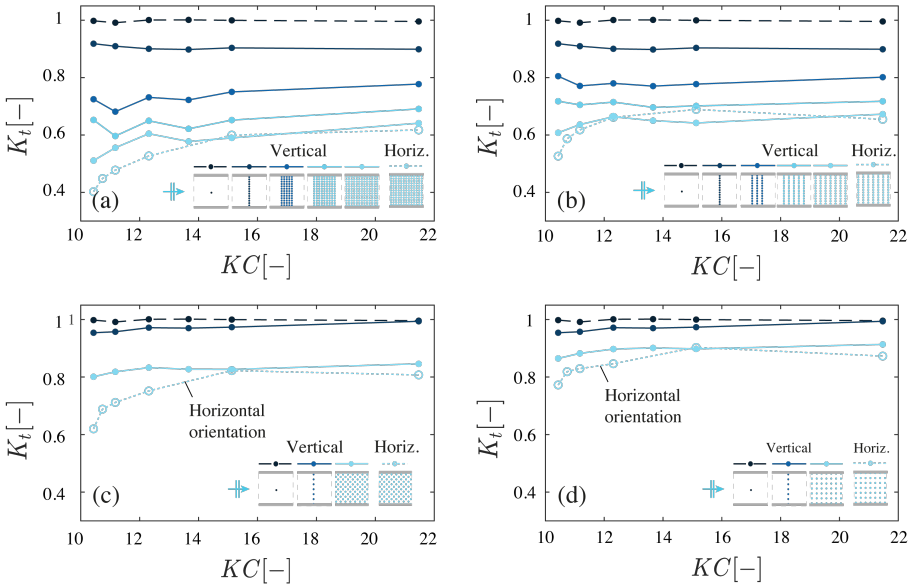

Figure 3.5: Wave transmission coefficient as a function of KC. Each plot shows the evolution of the transmission coefficient for the vertical configurations, from one single cylinder (black dashed lines), to a single row (black solid lines), and to a full configuration (solid blue lines, with lighter shades indicating a higher number of rows) for (a) DD13R, with $s_x = s_y = 1.5d$, (b) DS7R, with $s_y = 1.5d$ and $s_x = 3d$, (c) SS13T, $s_x = s_y = 3d$ in a staggered arrangement and (d) SS7R, $s_x = s_y = 3d$ in a regular arrangement. We also include the measurements with a horizontal orientation for each full configuration (light blue dotted lines). The plots show that the transmission rates are mostly influenced by the structure configuration, rather than the wave excursion, and that most wave attenuation takes place on the first rows of the structure. The results also indicate higher wave height reduction for the horizontal arrangements compared to the vertical orientations, especially for smaller wave periods.

configurations having transmission coefficients $10 - 20\%$ smaller, whereas for $KC > 15$ horizontal and vertical arrangements show similar wave transmission rates. Since the frames have the same frontal and volumetric porosity for both orientations (resulting in the same frontal area), and the measurements were collected for intermediate water conditions (for which the vertical velocities are still significant), the additional wave height reduction is likely due to the work done by the vertical drag forces[141].

3.4.2. Wave reflection

Wave height reduction behind the structures is partly due to wave reflection. The wave reflection rates for the different configurations are illustrated in Figure 3.6, where K_r represents the ratio of the reflected wave amplitude to the incoming wave amplitude. The results of 1C (single cylinder) are representative of wave reflection from the end of the flume, and show values oscillating between $K_r = 0.02 - 0.07$. We calculated K_r before the propagating wave reached WG4 after being partly reflected at the wave absorber. However, small oscillations were generated by the wave maker in the beginning of the experiments, which explain the reflection rates observed for 1C.

The reflection rates in front of the structures vary between $K_r = 0.05 - 0.4$. Wave reflection in front of the cylinder arrays increases with KC until $KC = 15$. Beyond this KC value, the reflection rates show a slight decrease for most configurations except for DS7R (Figure 3.6, b). The highest reflection rates are measured for the least porous configuration, DD13R (Figure 3.6, a), and the smallest reflection rates for the most porous configuration, SS7R (Figure 3.6,

d).

Wave reflection also varies depending on the cylinder arrangement. Using the same frontal area but increasing the number of rows (Figure 3.6 a and 3.6 b respectively), results in higher wave reflection. This is partly due to the increase in the number of cylinders. However, DS5R and DD5R have the same number of elements and the same frontal area, while DS5R (with a longer streamwise spacing, and thus a longer structure width) experiences lower reflection rates. This suggests that increasing the streamwise spacing, and the structure width in the direction of wave propagation, reduces wave reflection. Staggering the elements also reduces the reflection rates, as it can be observed by comparing Figure 3.6 (b) and (c).

3.4.3. Velocities and forces

Wave dissipation inside the structures is caused by the work done by the forces acting on the elements. We consequently investigated the magnitude of the forces and velocities measured inside different configurations in Figure 3.7. The measured velocity signals are asymmetrical in all cases, with larger negative than positive velocities (Figure 3.7 a and b). This is caused by asymmetric placement of the sensor, as illustrated in the upper sketches of Figure 3.7.

During the positive velocities the sensor measured the flow before it accelerated between the elements, whereas during the negative velocities it experienced the jet formed between the elements. Return currents could also increase the negative velocities, but the pronounced negative asymmetry is not observed in the measure-

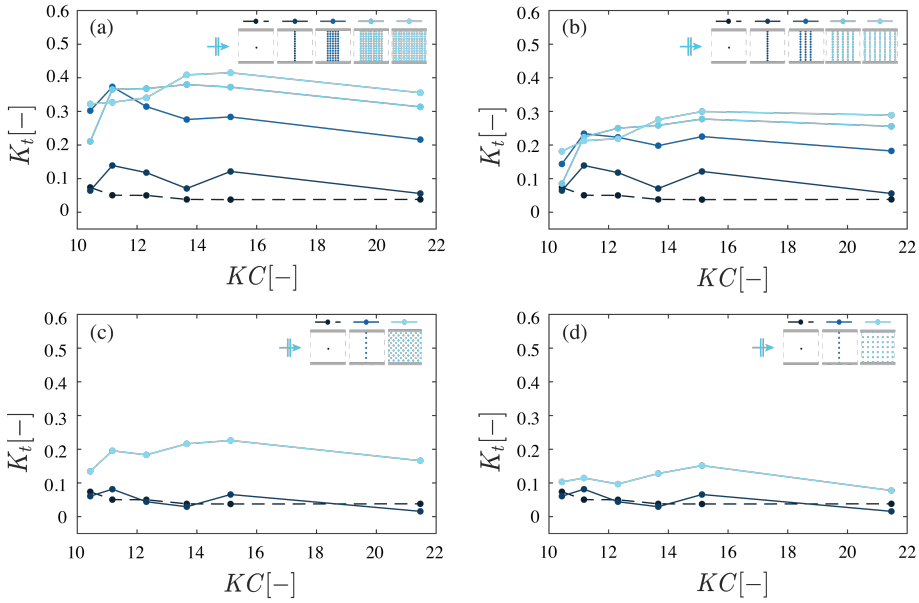

Figure 3.6: Wave reflection coefficient in front of the structure as a function of KC. Each plot shows the evolution of the reflection coefficient from one single cylinder, to a full configuration for (a) DD13R, with $s_x = s_y = 1.5d$, (b) DS7R, with $s_y = 1.5d$ and $s_x = 3d$, (c) SS13T, $s_x = s_y = 3d$ in a staggered arrangement and (d) SS7R, $s_x = s_y = 3d$ in a regular arrangement. The results show limited influence of the wave period on wave reflection, except for the lowest KC values. The reflection measurements vary with the frontal area, the number of rows and the spacing between rows. Wave reflection increases cumulatively by adding downstream rows, but the effect of each successive row is relatively smaller.

ments of the EMF, placed 0.4 m upstream from the frame. The negative velocities are thus indicative of how much the flow accelerates through the spacing between cylinders, whereas the positive velocities do not include blockage effects.

For $KC = 10$ (Figure 3.7 a) the negative velocities for the single row are 2.5 times larger than for a single cylinder. The first row of DS7R has similar negative velocities to the single row (D). Further into the structure the negative velocities reduce due to wave attenuation. In the last row, the negative velocities are actually comparable to those measured for a single cylinder. The velocities for $KC = 21$ (Figure 3.7 b) show a similar behaviour for the different configurations, but the increase in the negative velocities for the first row of the structure is smaller than for $KC = 10$, with velocities being a factor of 2 times larger than for a single cylinder.

The force measurements are shown in Figure 3.7 (c-d). The force signal for $KC = 10$ (Figure 3.7 c) has an almost 90° phase difference with the velocity, indicating inertia-dominated conditions. This is further shown in Figure 3.8, where the force coefficients were fitted for 1C (single cylinder) and D (single row with $s_y = 1.5d$), and used to estimate the contribution of the drag and inertia components to the total force. For both 1C (Figure 3.8 a) and D (Figure 3.8 c) with $KC = 10$ the inertia force is almost equal to the total force. The forces for the single row of cylinders and the first row of the structure are approximately 2 times larger than for a single cylinder, as shown in Figure 3.7 (c). The relationship between the increase in velocity and the increase in the forces is thus close to linear, which is consistent with inertia forces being linearly proportional to the

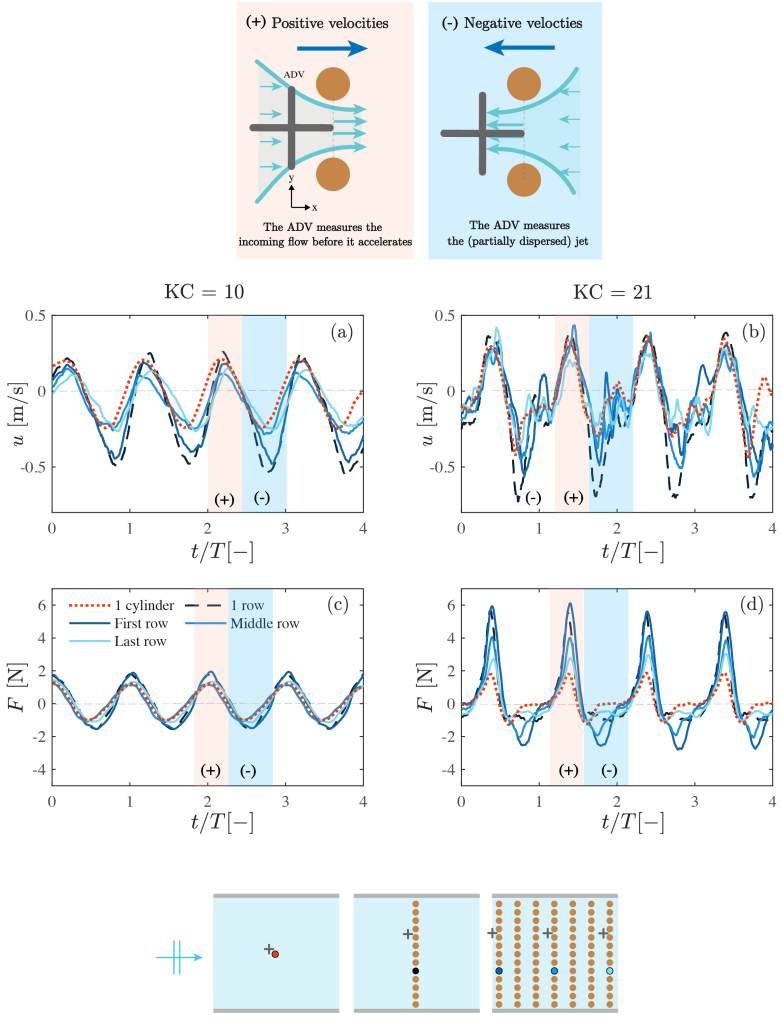

Figure 3.7: Forces and velocities measured for a single cylinder (1C), a single row (D) and a full structure (DS7R) for $KC = 10$ and $KC = 21$. The upper sketches show how the sensor placement affects the velocity measurements. When the velocities were in the direction of wave propagation, the sensor measured the flow before it accelerated between the cylinders. When the flow reversed, the sensor received the jet formed between the elements. The lower sketches show the location of the force (coloured dots) and velocity measurements (crosses) for the different configurations. Flow velocities increase between multiple cylinders compared to the the case with a single cylinder (a,b). Higher velocities also increase the forces acting on the elements (c,d).

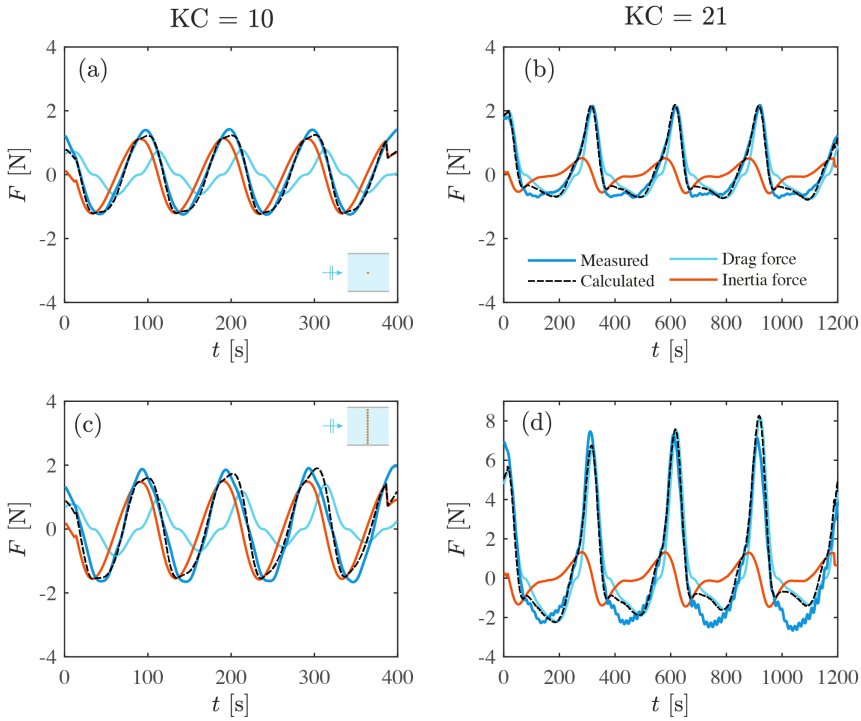

Figure 3.8: Comparison between measured and fitted forces for $KC = 10$, and configurations (a) 1C and (c) D, and for $KC = 21$, and configurations (b) 1C and (d) D. The measured force signal is shown in black, and the fitted signal in dark blue. The fitted force is decomposed in the inertia component (red) and the drag component (blue). For lowest $KC = 10$ (a,c) the force signal is dominated by inertia, whereas for $KC = 21$ (b,d) it is driven by the drag component.

acceleration.

The force signal for $KC = 21$ (Figure 3.7 d) is in phase with the velocity, indicating drag-dominated conditions. This can also be seen in Figure 3.8 (b) and (d), where the the drag component governs the total force. The forces for a single row and the first row of the structure with $KC = 21$ are approximately 2 times larger than for a single cylinder (Figure 3.7 d). If the drag forces were fully driven by blockage between the cylinders, the factor of 2 in the velocities would result in a factor of 4 in the forces, whereas the ratio we measure is smaller. Using the velocities between the elements in Equation 3.1 would consequently overpredict the drag forces for the present configurations and KC range. A similar behaviour is also found in the model results of Etminan *et al.*[44].

Etminan *et al.*[44] observed that bulk drag coefficients of cylinder arrays, which include the effect of the velocity changes on the drag forces, increase from the value of a single cylinder from $KC = 10$, until larger drag values between $KC = 20 - 60$. For higher KC numbers, the drag forces are well represented by the velocities between the cylinders due to mass conservation. Our measurements fall on their intermediate KC range, where blockage increases the drag forces compared to a single cylinder, but its effect is still reduced compared to $KC > 20 - 60$. Parameterizing the characteristic velocities for the drag forces in this KC range consequently requires applying a reduction coefficient to the velocities from mass conservation.

3.4.4. Drag coefficients

Drag coefficients from forces

The bulk drag coefficients based on the undisturbed velocities from the EMF of 1C, are shown in Figure 3.9. The drag coefficients of both the single cylinder and the single sparse row (in Figure 3.9 c and d) correspond well with drag values for a single cylinder from the literature, which decrease from $c_D \approx 2$ for $KC = 10$, to $c_D \approx 1.7$ for $KC = 21$[72,50,112]. The single denser row (in Figure 3.9 a and b), has drag higher values, approximately 2.5 times larger than for a single cylinder. These larger drag coefficients are likely due to blockage effects, as the flow contracts through the small openings between the cylinders.

The drag coefficients of the most porous configuration (SS7R) and the staggered structure (SS13T) are similar to the drag coefficients of a single cylinder, as shown in Figure 3.9 (c) and (d) respectively. The drag coefficients are higher for the structure formed by rows with a small lateral spacing and a relatively longer streamwise spacing (DS7R, shown in Figure 3.9 b), with $c_{D,b} = 2 - 4$ at the first row. The drag coefficient decreases at the middle and last rows of DS7R, since the undisturbed velocities do not include wave attenuation through the structure.

The least porous configuration (SS7R, shown in Figure 3.9 a) experiences smaller drag coefficients than DS7R. This can be partially explained by the higher reflection rates of the least porous structure. However, DS7R and DD9R have similar reflection rates for $KC = 21$, while the drag coefficient of DS7R is twice as large. This suggests that sheltering of downstream rows reduces the forces

acting on the cylinders. Sheltering effects thus decrease the work done per element, explaining the higher wave reduction efficiency of DS7R.

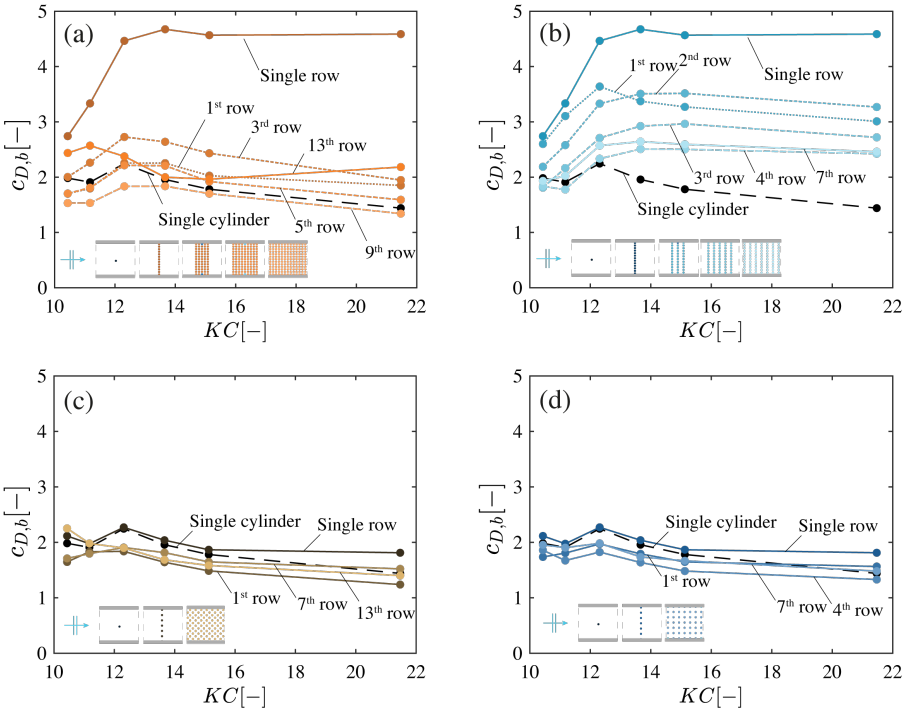

Figure 3.9: Bulk drag coefficient for configurations formed by multiple rows of cylinders as a function of KC. Each plot shows the evolution of the bulk drag coefficient from one single cylinder (dashed line), to a full configuration for (a) DD13R, with $s_x = s_y = 1.5d$, (b) DS7R, with $s_y = 1.5d$ and $s_x = 3d$, (c) SS13T, $s_x = s_y = 3d$ in a staggered arrangement and (d) SS7R, $s_x = s_y = 3d$ in a regular arrangement. The sparse (d) and staggered (c) arrangements have bulk drag values similar to the results of a single cylinder. The configuration formed by dense rows with a big streamwise spacing (b) has the highest bulk drag coefficients. When the dense rows are placed with a smaller streamwise spacing (a), the bulk drag decreases.

3.4.5. Predicting wave transmission

The expressions for wave dissipation (Equations 3.3 and 3.4) are based on the assumption of undisturbed flow, which does not hold for some of the configurations tested in the present study. However, we wondered whether these expressions could still provide reasonable predictions if blockage and sheltering effects inside the structure are accounted for.

Etminan *et al.*[44] and van Rooijen *et al.*[123] observed that the bulk drag coefficient for arrays mimicking natural vegetation was well represented by mass conservation through a cross-section of the array, as shown in Equation 3.13:

$$c_{D,b} = c_D \left(\frac{A}{A_c} \right)^2 \tag{3.13}$$

where c_D is the drag coefficient of a single cylinder, A is the total area of the cross-section of the flume, and A_c is the total available flow area between the cylinders. The wave transmission predictions obtained by using the bulk drag from Equation 3.13 are shown in Figure 3.10 (a).

We predicted wave transmission with Equation 3.3 for vertical orientations and Equation 3.4 for horizontal elements. Measurements and predictions are compared for the configurations tested with both vertical and horizontal orientations. The measured transmission rates were corrected to exclude the effect of wave reflection, which is not calculated by Equations 3.3 and 3.4. Using the drag coefficient derived from mass conservation underpredicts the measured transmission (Figure 3.10 a), indicating that the work done by the cylinders is overpredicted.

We also estimated wave transmission using the bulk drag val-

ues derived from the force measurements, illustrated in Figure 3.9. These predictions are shown in Figure 3.10 (b). For each configuration we used the bulk drag coefficients fitted to the first row of the structure. The bulk drag measurements of the middle and back rows were calculated as a function of the undisturbed velocities, and they consequently include the effect of wave attenuation through the structure. Implementing them in Equations 3.3 and 3.4 could thus result in an underprediction of the wave dissipation.

Using $c_{D,b}$ values derived from the forces to predict wave transmission provides a better agreement with the measurements, but it leads to an overestimation of the measured wave transmission, as it can be observed in Figure 3.10 (b). Chen *et al.*[28] also overpredicted wave transmission measurements when they used the same approach. This is discussed further in the following section.

Relating drag coefficient fitted from forces and dissipation

The bulk drag coefficients derived in the present study (Figure 3.9) were fitted to the forces and they are consequently related to the undisturbed velocity to the power of two:

$$c_{D,b} \sim \frac{F_d}{u^2} \tag{3.14}$$

However, when the bulk drag coefficient is used as an empirical factor to reproduce wave transmission measurements, it relates to the undisturbed velocity to the power of three:

$$c_{D,w} \sim \frac{\epsilon_v}{u^3}, \tag{3.15}$$

where the subscript w denotes that the empirical drag coefficient is related to the wave dissipation rate. Considering the previous

relationships, by using a bulk drag coefficient derived from force measurements to estimate wave dissipation we might underestimate the effect of the velocity changes inside the structure.

In order to account for the power of the velocity, we related the measured forces to the drag coefficient of a single cylinder, c_D, and replaced the undisturbed velocity u by the characteristic drag velocity u_c, which includes the effect of the structure on the flow. The relationship between u_c and $c_{D,b}$ is given by Equation 3.16:

$$F_d \sim c_{D,b} u^2 \sim c_D u_c^2 \tag{3.16}$$

Solving for u_c results in:

$$\frac{u_c}{u} = \sqrt{\frac{c_{D,b}}{c_D}} \tag{3.17}$$

Equation 3.17 expresses the bulk drag as a factor that multiplies the undisturbed velocity. Assuming that the magnitude of the characteristic velocity is the same for wave dissipation, but taking into account that the dissipation is proportional to the velocity to the third power, results in:

$$c_{D,w} = c_D \left(\frac{u_c}{u}\right)^3 \tag{3.18}$$

This formulation expresses the characteristic velocity inside a canopy as an empirical drag coefficient that can be included in the dissipation term ϵ_v. Introducing Equation 3.18 in Equation 3.3 would result in:

$$\epsilon_v = \frac{2}{3\pi} \rho c_D \left(\frac{u_c}{u}\right)^3 dN_v \left(\frac{kg}{2\omega}\right)^3 \left(\frac{\sinh^3 kh + 3\sinh kh}{3k\cosh^3 kh}\right) H^3 \tag{3.19}$$

And for Equation 3.4 it results in:

$$\epsilon_v = \frac{2}{3\pi}\rho c_D \left(\frac{u_c}{u}\right)^3 dN_v \left(\frac{kg}{2\omega}\right)^3 \left(\frac{\sinh^3 kh + 3\sinh kh}{3k\cosh^3 kh} + \frac{\cosh^3 kh - 3\cosh kh + 2}{3k\cosh^3 kh}\right) H^3 \tag{3.20}$$

The wave transmission predictions from Equations 3.19 and 3.20 are shown in Figure 3.10 (c) and (d). In Figure 3.10 (c) we estimated the characteristic drag velocity u_c from mass conservation in a cross-section of the array, with $u_c/u = A/A_c$, where A is the total cross-section of the flume, and A_c the available flow area between the cylinders. In Figure 3.10 (d) we estimated the characteristic drag velocity u_c from the the bulk drag measurements derived from the forces, using Equation 3.17.

Using the velocities due to mass conservation to the power of three also underpredicts the wave transmission measurements (Figure 3.10, c). The best agreement between predictions and measurements is obtained when using the empirical characteristic drag velocity to the power of three (Figure 3.10, d). These results suggest that the bulk drag coefficients derived from wave transmission measurements and those derived from force measurements are related, but they are not directly exchangeable. Using bulk drag coefficients from forces to predict wave dissipation requires expressing $c_{D,b}$ as a characteristic drag velocity (as done in Equation 3.17), and introducing it in the dissipation rate to the power of 3. The results also show that the expression of Suzuki *et al.*[141] as a function of the characteristic velocity provides a good agreement with the transmission rates observed for horizontal arrangements. This agreement between observations and predictions supports that the additional dissipation observed for horizontal structures is caused by the work

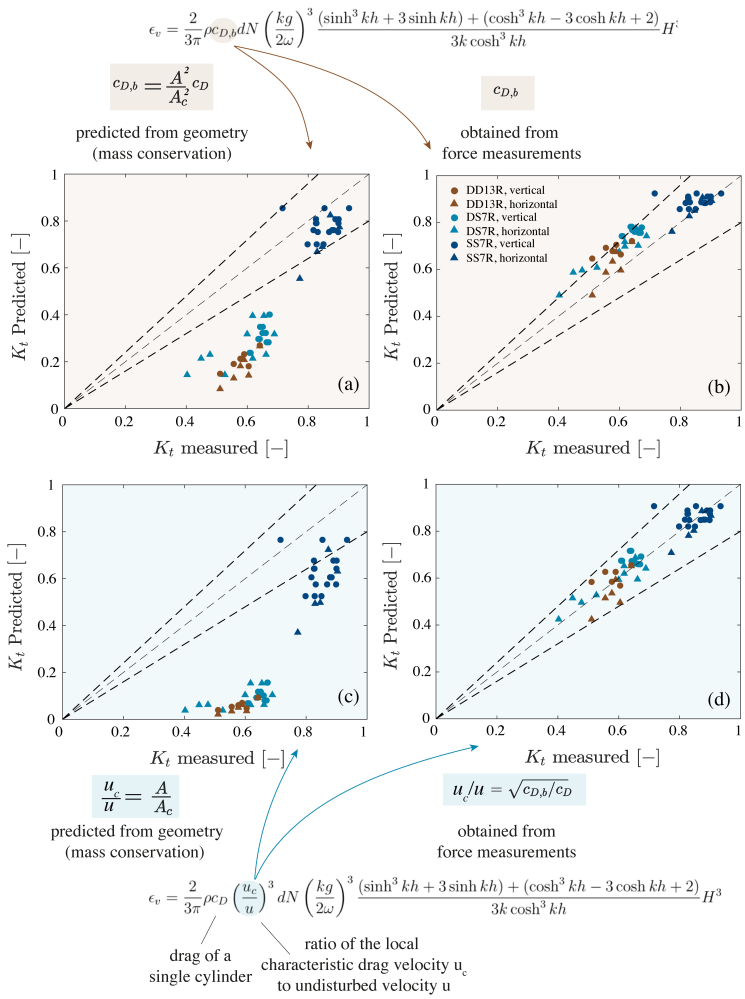

Figure 3.10: Measured versus predicted wave transmission rates from Dalrymple *et al.*[32] for the vertical structures (circles), and from Suzuki *et al.*[141] for the horizontal configurations (triangles). (a) Results obtained using the bulk drag $c_{D,b}$ derived from the constrained velocities (Equation 3.13). (b) Results obtained using the $c_{D,b}$ values from the forces measured at the first row of the structure (from Figure 3.9). (c) Results obtained using the constrained velocities in the wave energy dissipation rate. (d) Results obtained using the characteristic drag velocities u_c from Equation 3.17 in the wave energy dissipation rate. The best agreement with the measurements was obtained using the characteristic velocity from the drag forces to the power of 3 (d).

done by the vertical drag forces, and that the drag coefficient does not experience large changes when varying the cylinder orientation.

3.4.6. Model results

Applying the empirical model presented in section 3.3.2 requires defining the empirical coefficients for the drag forces, f_{KC}, and c_s, and the empirical coefficient for wave reflection, c_R.

f_{KC} was calculated using a linear fit through the laboratory measurements, resulting in Equation 3.11:

$$f_{KC} = 0.012KC + 0.44, \tag{3.21}$$

We fitted c_s such that we could reproduce the sheltering effects observed in the present experiments. The bulk drag coefficients of downstream rows include the effect of wave attenuation, and using them would overestimate sheltering effects. However, due to flow reversal under waves the elements of the first row also experience sheltering during half of the wave cycle. c_s is thus obtained by calculating the ratio of the $c_{D,b}$ value measured at the first row of the full configurations (SS7R, DS7R and DD13R) to $c_{D,b}$ values of the single rows (S and D), resulting in $c_s = 0.796$.

The factor c_R was obtained by fitting Equation 3.5 to the reflection measurements of configurations S and D, resulting in $c_R = 41.81$. We subtracted the energy reflected from the end of the flume from the measurements, since it is not accounted for in Equation 3.5.

The model can reproduce the trends observed in the reflection and transmission measurements, as shown in Figure 3.11. The max-

imum differences between modelled and measured wave heights are 0.019 m for the transmitted components, and 0.020 m for the reflected components. The deviations for different wave periods are probably linked to neglecting the influence of the wave length on sheltering and wave reflection.

Including sheltering and reflection is important for design optimization, since both processes influence how wave dissipation varies with cylinder density. For instance, the original formulation of Dalrymple *et al.*[32] gives lower transmission rates for higher cylinder densities. The inclusion of blockage in their formulation would enhance this trend further, since higher densities would also lead to higher dissipation per element.

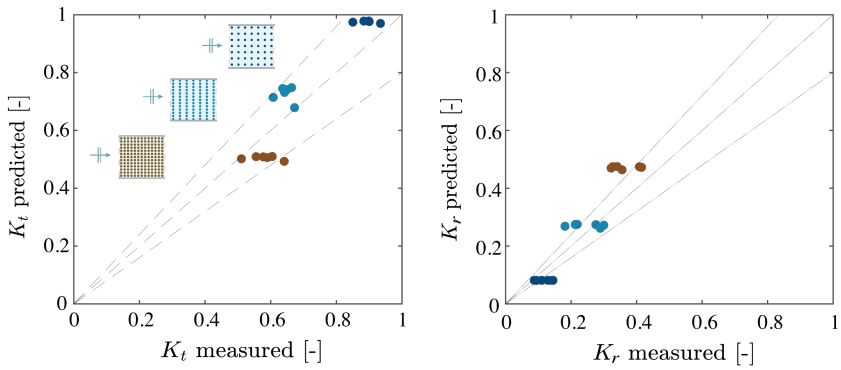

Figure 3.11: Validation of conceptual model. The left plot shows the comparison between the measured and computed transmission coefficient for SS7R (dark blue circles), DS7R (light blue circles), and DD13R (brown circles). The cylinder configuration is illustrated to the left of the results for all arrangements. The right plots shows the comparison between the measured and computed reflection coefficient for SS7R (dark blue circles), DS7R (light blue circles), and, DD13R (brown circles). The black lines indicate a 20% deviation of the results.

Sheltering would have the opposite effect, reducing wave dissipation per element if the streamwise separation s_x is small enough. Wave reflection would also decrease the wave energy available for dissipation. However, the relative influence of the previous processes is not known. We thus compared the effect of wave reflection and sheltering on wave transmission, and illustrated the results for $s_x = 1.5d$ and $s_x = 10d$ in Figure 3.12. We analyzed structures with a total width (in the wave direction) of $w = 0.76$ m, a cylinder diameter of $d = 0.04$ m, and varying lateral spacing s_y, with $s_y/d = 1.1 - 10$. The wave conditions were set to $H = 0.13$ m, $T = 3$ s, $h = 0.55$ m, which corresponded with $KC = 21$.

Figure 3.12 (a) shows that both sheltering and wave reflection have a small effect on wave transmission for $s_x = 10d$. Wave reflection becomes non-negligible for densities larger than $N_v = 20$ elements/m^2 (Figure 3.12 c), but it also has a small effect on wave dissipation (Figure 3.12 e). The effects of sheltering are more pronounced for $s_x = 1.5d$, with the dissipation being reduced almost by half for $N_v = 100$ elements/m^2 (Figure 3.12 f).

The influence of wave reflection on wave dissipation is larger for $s_x = 1.5d$ than for $s_x = 10d$, but still smaller than sheltering. This comparison suggests that accurate descriptions of sheltering may be important to predict wave transmission. Including wave reflection has a relatively smaller effect on the wave transmission predictions, but precisely assessing its magnitude is necessary to ensure the stability of the designs.

We also assessed the relative performance of different configurations in Figure 3.13, with downstream spacings varying between $s_x = 1.2 - 10d$. The remaining model parameters were set equal

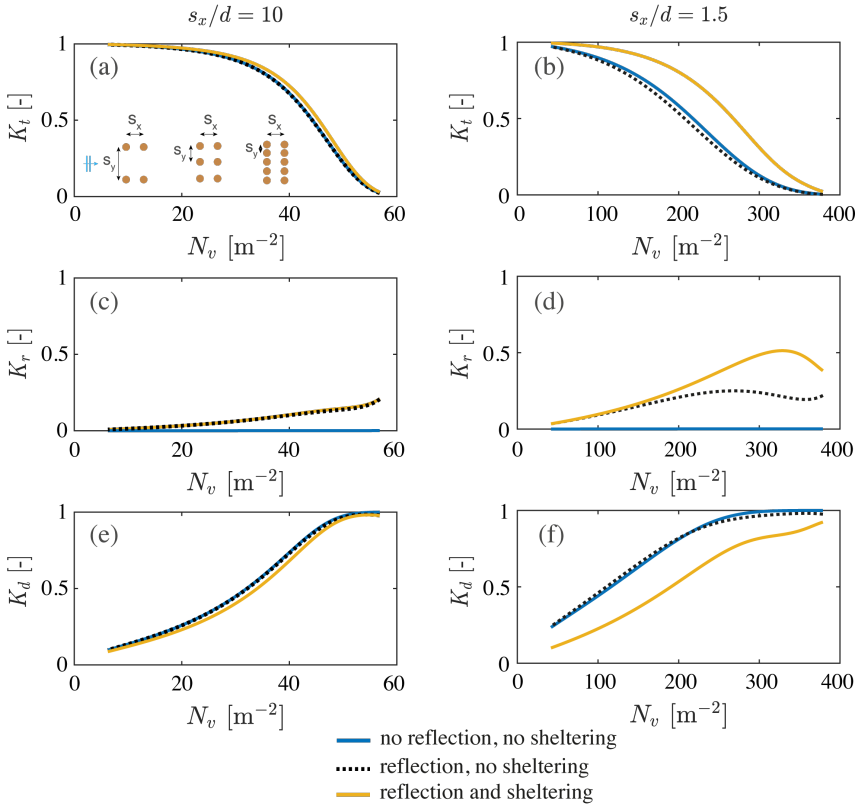

Figure 3.12: Wave transmission rates for configurations with (a) $s_x = 10d$ and (b) $s_x = 1.5d$. Wave reflection rates for configurations with (c) $s_x = 10d$ and (d) $s_x = 1.5d$. Wave dissipation rates for configurations with (e) $s_x = 10d$ and (f) $s_x = 1.5d$. The blue lines are obtained using Equation 3.19 and $u_c/u = f_b$. The black lines are obtained including the effect of reflection from Equation 3.5, and without including sheltering. The yellow lines are obtained accounting for reflection and including sheltering in the characteristic velocity (Equation 3.10). Sheltering effects are very small for the configuration with a large streamwise separation (a,c,e), whereas it reduces the wave dissipation coefficient up to 50 % for the configuration with smallest spacing (f). Wave reflection has a relatively smaller effect on wave transmission, but high reflection rates could hinder structure performance in the field.

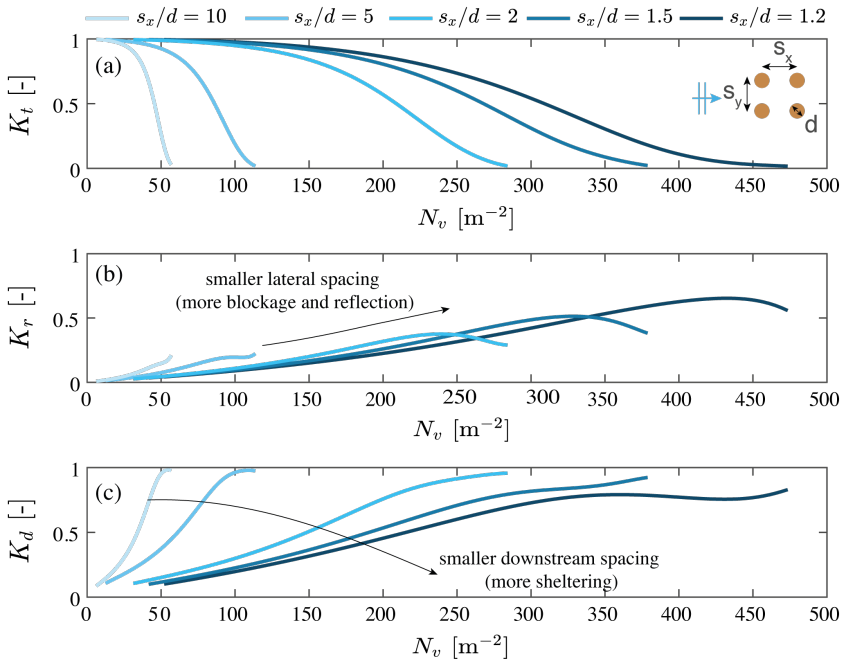

Figure 3.13: (a) Wave transmission rates, (b) wave reflection rates, and (c) wave dissipation rates for configurations with a downstream spacing between $s_x/d = 1.2 - 10$, plotted with different shades of blue (with lighter colours indicating longer downstream separation). For each s_x value the lateral spacing varies between $s_y/d = 1.1 - 10$. The same wave transmission can be achieved with different cylinder densities, but higher densities are associated to higher wave reflection rates.

to those of Figure 3.12. Figure 3.13 shows that the same amount of wave transmission can be reached over a fixed structure length with different cylinder densities. For instance $K_t = 0.5$ can be obtained with $N_v = 45$ elements/m^2 (for $s_x = 10d$), and with $N_v = 308$ elements/m^2 (for $s_x = 1.2d$). However, the reflection rate is lower for $N_v = 45$ elements/m^2, with $K_r = 0.13$, compared to $N_v = 308$ elements/m^2, with $K_r = 0.44$. Using less elements in sparsely placed rows consequently increases wave dissipation and reduces wave reflection compared to a denser and more homogeneous structure. The same trends were obtained with cylinder diameters of $d = 0.02$ m and $d = 0.08$ m.

3.5. Discussion

3.5.1. Limitations of the experimental data

Our work provided insights on the factors affecting the drag coefficients inside dense cylinder arrays within a limited range of conditions, with $KC = 10 - 21$ and two values of cylinder spacing. Obtaining measurements for a wider range of KC values and spacings is recommended to develop more generic parameterizations. Moreover, additional physical processes could modify the bulk drag coefficients in the field compared to the values of this study

The combination of waves and local currents could be one factor influencing the bulk drag coefficients. Coexistent currents generally decrease the drag coefficient, with a more pronounced drag reduction for a higher magnitude of the current compared to the orbital velocities[136]. This effect is attributed to stronger currents sweeping turbulence away from the cylinders, suppressing turbu-

lence enhancement by waves.

Despite the drag coefficient reduction, currents can also enhance wave dissipation by increasing the flow velocities and the total work (Equation 3.3). Hu *et al.*[58] observed that the generation of wave-driven return currents in pure wave flows increased flow asymmetry, and thus wave dissipation. Their study showed that relatively small currents counteracted the wave-driven return flows, reducing wave dissipation, while large currents increased the total work. Wave-driven currents had a negligible effect on both drag coefficients and wave dissipation for the conditions tested in the present work. Wave-current interaction effects are also expected to be small in Demak, where the structures are placed in shallow waters where wave orbital velocities are one order of magnitude larger than the mean flow. However, this factor could differ at other sites.

Element roughness, due to irregularities from the bamboo or barnacle growth, could also influence the drag coefficients. Roughness generally increases the drag coefficient to higher values. However, it can also cause a drag reduction for $Re \approx 10^4$, as shown in Figure 4.20 of Sumer and Fredsoe[136]. The net effect of roughness on the drag coefficient will thus depend on the local flow and material properties. Changes in diameter due to degradation of the bamboo could also gradually decrease the drag forces on the poles.

Our work suggests that $c_{D,w}$ does not change significantly for horizontal elements, but wave dissipation is higher for horizontal arrays than for vertical arrays. The increase in wave dissipation is attributed to the work done by the vertical velocities in relatively deeper water. This additional dissipation term for horizontal elements could also be relevant for modelling aquatic vegetation.

Neglecting the vertical drag for horizontal roots, such as those of red mangroves, or for horizontal branches, would lead to having to fit higher values of $c_{D,w}$ to compensate the lack of one dissipation term. However, this process will only be significant for relatively short waves compared to the water depth.

3.5.2. Model limitations

The model presented in Section 3.3.2 can qualitatively reproduce the influence of cylinder arrangement, but it should be further developed for its application in detailed designs. For instance, we assumed that the expression of White[166] for the drag coefficient of a single cylinder remains applicable for very small s_y values. Considering an analogy with a cylinder close to a wall in uniform flow, vortex shedding could be inhibited for very small lateral separations between cylinders[136]. This would in turn reduce the drag coefficient compared to the values of White[166], but this process has not been investigated for wave flows.

The wake flow model represented by Equation 3.12 does not describe the changes in flow velocity as a function of s_y, which would be necessary for modelling staggered and random arrangements. The model is also limited for turbulent flow, since Reynolds numbers in the field are of $\mathcal{O}(10^3 - 10^4)$. For applications where viscous effects are significant, the velocity deficit in the wake will decrease compared to the results of Equation 3.12[38]. Moreover, c_s values may vary for different structure and wave properties. Predicting c_s for any cylinder arrangement, given its geometry and the local wave conditions, requires a turbulence model that reproduces turbulence enhancement by waves. For high KC values, the model developed

in Chapter 2 for dense cylinder arrays in a current could be applied to estimate c_s. For low KC values, the model should be expanded to include the effect of flow reversal on the turbulent intensity.

Lastly, the present formulation for the wave reflection factor c_R neglects the influence of varying wave properties, since our wave transformation measurements were mostly influenced by structure configuration. However, this assumption should be verified for KC values outside the range tested in this study.

3.5.3. Implications for design optimization

If waves approach the coastline from a relatively constant direction, placing the bamboo poles in dense rows with a relatively longer streamwise spacing could maximize wave dissipation per element. If the direction of wave incidence has considerable variability over time, combining several structures with different orientations (based on the most frequent wave directions) or using staggered arrangements may be preferable. However, additional aspects such as the construction procedure or soil properties may also influence design optimization.

The effect of the structures on coastal accretion will also depend on the local sediment properties. The following chapter investigates the influence of the structure location on the morphodynamics, in order to find designs that protect and expand the mangrove habitat.

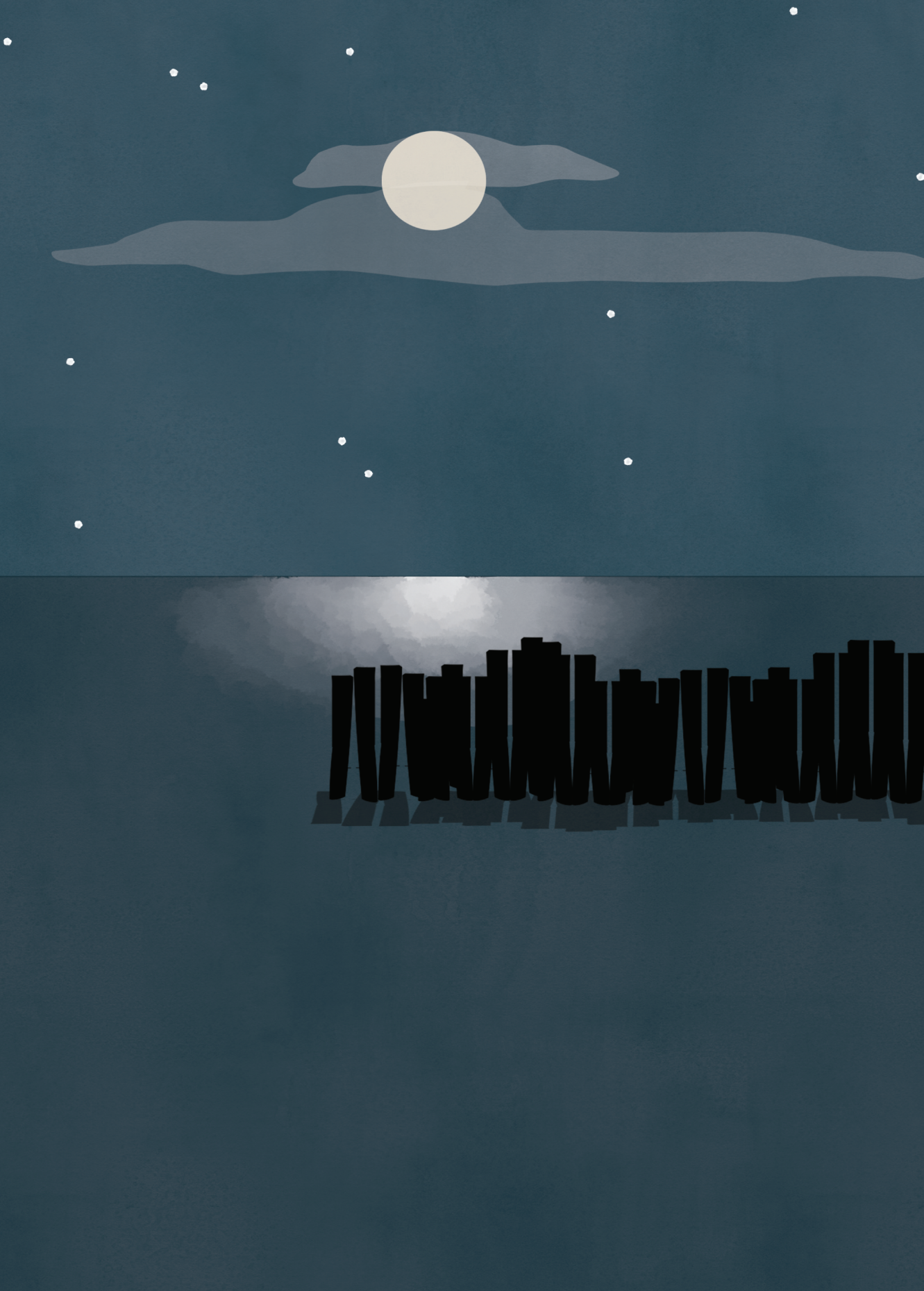

4. Effect of structures on morphodynamics

4.1. Introduction

Bamboo structures attenuate waves to promote sediment accumulation on their land side, thereby creating an area for mangrove establishment. The previous chapter thus investigated how to predict wave transmission through the structures based on laboratory experiments. Designing a structure that stops coastline retreat requires an additional step - linking changes in wave height to the local morphodynamics. Moreover, sediment accumulation by bamboo structures may be limited by boundary conditions such as sediment availability or the local subsidence rates. This chapter thus focuses on the development of a morphodynamic model to predict the effect of the structures on the coastline, and investigates in which conditions bamboo structures can aid mangrove restoration. The content of this chapter is included in the following publication:

A. Gijón Mancheño, A.J.H.M. Reniers, B.K. van Wesenbeeck, C.E.J. van Bijsterveldt, S.A.J. Tas, T. Wilms, M. Muskanonfola, and J.C. Winterwerp (2021). Restoring eroding mangrove coastlines using nature-based structures (in preparation for submission).

4.2. Mangrove restoration at retreating coasts

Mangrove forests are formed by approximately 70 species of intertidal trees and shrubs. Although mangroves can tolerate tidal flooding, different species have specific requirements in terms of inundation height and duration[161]. Mangroves are thus directly threatened by sea level rise, since they can die if their location becomes a tidal flat or a subtidal area.

Mangroves can counteract rising sea levels by enhancing sediment accumulation and building up peat[170,85,95,129,162]. Historically, vertical accretion by mangroves could compensate up to 7 mm/year of sea level rise[125]. Nevertheless, climate change could induce larger rates of sea level rise according to the high emission scenarios of IPCC[63], which estimate 10 mm/year. Locally, subsidence rates may be even higher, and reach decimeters per year[53,164]. The threshold that mangroves can survive may also be lower than 7 mm/year at sites with limited sediment availability and low sediment transport capacity by waves and currents[85].

Under pristine conditions, when rising sea levels cannot be fully compensated by vertical accretion, mangrove ecosystems can survive by migrating towards the land as the sea level rises. However, today such shifting is often constrained by urban developments, which threaten the long-term resilience of these ecosystems[152]. Conservation and restoration of existing mangrove forests is thus key for their long-term survival and for coastal protection of the hinterland.

In deforested regions, mangroves are often restored by planting

seedlings. Many of these efforts fail due to a mismatch between abiotic conditions and species selection[118]. Mangroves are often planted at sites that are too low for their survival or growth[79] and this problem will worsen with subsidence and sea level rise. Therefore, the Ecological Mangrove Restoration movement[79] was developed, which focuses on restoring the abiotic conditions needed for mangrove colonization. For open coastlines, several requirements for mangrove establishment have been identified by Balke *et al.*[12], which are illustrated in Figure 4.1.

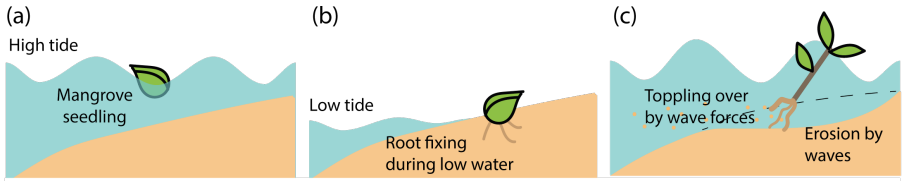

Figure 4.1: Diagrams illustrating mangrove establishment. (a) Mangrove seeds float along the coastline, (b) until they find an emerged spot to fix their roots. (c) Over time, if waves are high while the seedling is still growing, it can be toppled over, or the soil where it stands can be eroded away. Seedling survival thus depends on a long-enough window of opportunity with calm wave conditions, during which the seedling can grow undisturbed.

Mangrove seeds float along the coastline, until they strand at an emerged intertidal area where they can grow their roots[120], as illustrated in Figure 4.1 (a-b). The first requirement for mangrove establishment is thus the local emergence time[12,161]. If an area has experienced severe erosion and subsidence the water depth may be too large for seedling survival[174].

Secondly, when a mangrove seed settles at a location with the right elevation with respect to the tide, it requires a period of low wave action (also denoted as window of opportunity) to be able

to grow undisturbed by waves and related sediment dynamics[12]. If a location is exposed to high waves, they may dislodge small seedlings, and prevent mangrove colonization, as shown in Figure 4.1 (c). Sediment erosion could also reduce the anchorage forces acting on the seedlings, or even fully uproot them from the sea bed.

Permeable structures have been built to restore the mangrove habitat at retreating coastlines of Thailand, Vietnam, Indonesia, Suriname and Guayana[165,168,169]. The structures usually consist of a brushwood filling held by vertical bamboo poles, and they dissipate wave energy and create sedimentation basins at their land side. When suspended sediment is brought from offshore by the rising tide, the lower shear stresses behind the structures favour sediment deposition[168,169]. Over time, the bed level builds up, and drifting seeds can strand on the newly accreted land during low tide. Wave attenuation by the structures also creates a sheltered area that favours seedling survival.

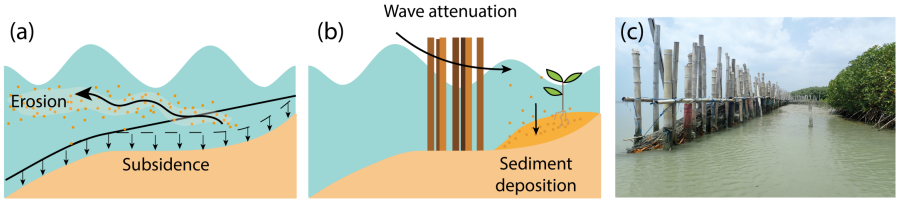

Figure 4.2: (a) Increase of the water level at the coast due to subsidence and erosion. (b) Foreshore restoration using permeable structures, which attenuate waves and enhance deposition landwards from them. Since the structures only restore the area behind them, in order to continue expanding the shoreline, a new structure should be built offshore from the old one in posterior stage. (c) Photograph of a bamboo and brushwood structure in Demak, Indonesia.

Existing designs are largely empirical, and a generic understanding of system characteristics under which these structures perform best, and where the limits of their performance lie, is yet lacking. In subsiding coastlines, the increase in water level as the ground sinks can only be compensated by a continuous sediment supply. If the subsidence rates are very high and there is not enough sediment available in the system, the presence of the structures will not stop coastline retreat in the long term.

Previous research has investigated the effect of brushwood structures on waves[34], and for alternative structures formed by bamboo poles (Chapter 3). However, these studies did not explore how different designs and structure locations would impact the morphodynamics. Here we thus test if permeable structures are a robust method to mitigate erosion and trap sediment under several scenarios of relative sea level rise. We do this by combining field measurements and the numerical model developed by Reniers et al.[121].

In order to validate the model, we collected field data in the area of Demak, in north Java (Indonesia). We monitored wave transformation through structures built in this area, and collected data of the local bathymetry, currents and sediment turbidity, which were used to set up the model. We then evaluated the morphodynamic effect of the structures, and investigated the qualitative impact of the structure location on coastline migration. Lastly, structures were modelled for several scenarios of sediment supply and relative sea level rise.

4.3. Field experiments and numerical model

4.3.1. Location description

The region of Demak is located at the North coast of Java, Indonesia (Figure 4.3 a). Its coastline is delimited by the Wulan river delta in the north, and the city of Semarang in the south. The local climate is monsoonal, driven by the North-West (NW) monsoon (November-March), and South-East (SE) monsoon (April-November), with two transition seasons in between[89]. During the NW monsoon the wind blows from the sea towards the land, resulting in offshore wave heights up to 2 m[160]. Conversely, during the SE monsoon the wind blows from the land towards the sea, producing smaller wave heights up to 0.4 m[160]. The tide in Demak is mixed-diurnal, with a mean spring tidal of approximately 1.0 m, implying a microtidal system[149].

The coastal area is mostly formed by soft clay deposits, and it experiences severe subsidence rates up to 0.16 m/year[174] due to extensive groundwater extraction in Semarang and along the national highway. Most of the coastal region was converted to aquaculture ponds during the 20th century. A storm in 2007 eroded the pond bunds, exposing aquaculture areas and coastal villages to flooding by tides and to wave action. The shoreline has been retreating since then due to erosion and subsidence, with maximum retreat rates of 215 m/year[86].

Bamboo and brushwood structures have been built in a pilot project in Demak to mitigate erosion and create a sheltered environment for mangrove restoration[165,168,169]. The structures were placed between 2014-2020 with a shore parallel orientation at a dis-

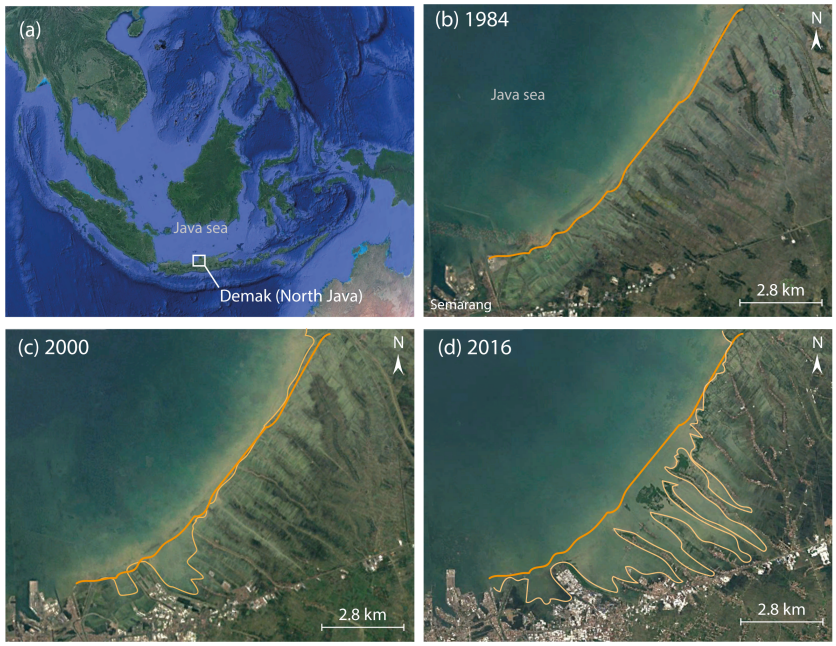

Figure 4.3: Evolution of the coastline of Demak, in North Java (Indonesia). The location of Demak is shown in plot (a). The coastline evolution over time is shown for (b) 1984, (c) 2000, and (d) 2016. The original coastline of 1984 is illustrated in orange, and the coastlines of following years are shown by yellow lines. Mangrove deforestation and land subsidence due to groundwater extraction in Semarang have resulted in severe coastline retreat, with maximum retreat rates of 215 m/year.

tance of approximately 100 m from the coastline. At this distance the water depth varied between 0.2-1 m[36] in 2019. The structures had widths varying between 0.7-1.5 m in the cross-shore direction, and an alongshore length of approximately 100 m, with 10 m-long gaps between structures. These gaps were designed to enable sediment influx by the tide.

The structures induced 20-30 cm of accretion behind them compared to control locations without structures, and initial mangrove colonization was observed at some locations[36]. However, long-term mangrove establishment was only observed behind 1 out of the 19 structures of the pilot project[36], and the coastline continued to retreat after their construction[156].

4.3.2. Field data collection

We conducted two field campaigns in Demak, one in July-August of 2017 (T1) and another in November-December of 2018 (T2). In each campaign, we monitored the impact of bamboo and brushwood structures on waves, flow velocities, and water turbidity along a transect (see Figure 4.4). Both locations T1 and T2 correspond to nearby but different bamboo and brushwood structures. The structure we had monitored in T1 (August 2017) had collapsed by November of 2018. T2 consequently monitors a new structure placed 5 m seawards from the broken structure (Figure 4.4).

Two frames were placed in each monitoring transect, seawards and landwards of a bamboo and brushwood structure. An acoustic Doppler velocimeter (ADV, from Nortek, measuring waves and currents) and an optical backscatter sensor (OBS, from Campbell,

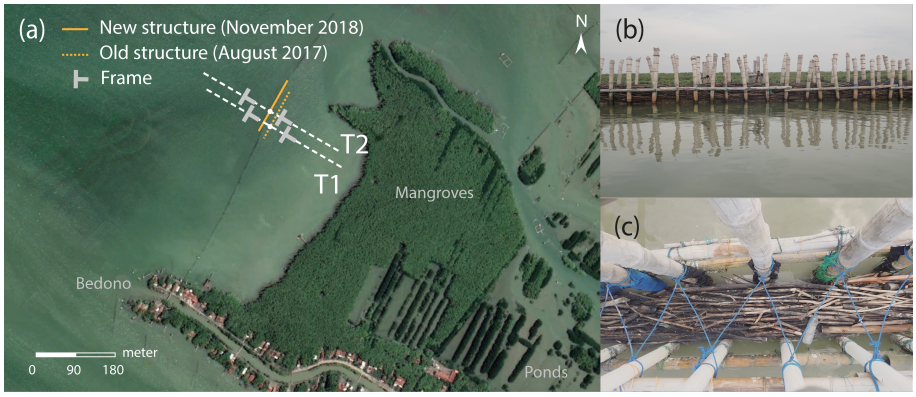

Figure 4.4: (a) Top view of the transect locations, indicating the monitored structures and the seaward and landward frames. (b) View of the bamboo and brushwood structure of T1 (2017). (c) Top view of the bamboo and brushwood structure of T2 (2018). The location of the 2018 transect had to be changed due to the collapse of the structure shown in (a).

measuring the turbidity of the water) were mounted in each frame. The ADVs and OBSs measured over 20 minute-long bursts, every 30 minutes, with a frequency of 16 Hz. The ADVs were oriented towards the bed in 2017, and horizontally in 2018. The orientation was modified to minimize sun exposure and heating of the sensor. The OBSs were pointed horizontally towards the sampling volume of the ADV. The height of all sensors with respect to the bottom is shown in Table C.1 of Appendix C.

The bathymetry along the transects was collected by measuring the distance between the water surface and the sea bed. This distance was determined by using a measuring pole with a flat ground plate attached to it. The plate prevented the pole from sinking into the soft sediment. The recorded depth measurements were corrected and referred to the mean sea level of each period, using data from the tidal station in Semarang. The bathymetry of the

higher part of the profile (i.e. for $z >$ -0.3 m with respect to MSL) could not be measured since high tide took place in the middle of the night during our field campaign, and this part of the profile was always emergent during the day. The higher part of the profile was extrapolated based on bathymetries measured at a nearby site in Demak[160].

4.3.3. Data analysis

Pressure measurements were processed to derive wave spectra over periods of 20 minutes, at a frequency resolution of 0.04 Hz. Significant wave heights and mean wave periods were derived from the energy density spectra. The mean water levels were calculated by averaging the pressure signal over each 20-minute interval.

Horizontal velocity measurements collected by the ADV were rotated to local coordinates of the transect, where the x-direction is defined as perpendicular to the local coastline and the y-direction is parallel to the coast. The rotated velocities were then averaged over the burst duration (20 minutes) to compute the mean flow velocities. For the ADV pressure measurements, the velocity information was used to determine the wave direction using the Maximum Entropy Method[87]. This enabled separating the incoming and outgoing energy fluxes through the structures.

4.3.4. Modelling

The morphodynamic processes along a coastal profile were reproduced using the model of Reniers et al.[121], XMgrove, based on the approach of Maan *et al.*[88]. XMgrove models the depth-averaged

morphodynamic processes across a coastal transect (1D). The main equations constituting the model are presented below.

Flow

Water level and tidal flow velocities are calculated from mass conservation (Equation 4.1), and from the momentum equation in the cross-shore direction (Equation 4.2):

$$\frac{\partial \eta}{\partial t} + \frac{\partial q_x}{\partial x} = 0 \tag{4.1}$$

$$\frac{\partial u}{\partial t} + u\frac{\partial u}{\partial x} = -g\frac{\partial \eta}{\partial x} - \frac{\tau_{b,cx}}{\rho_w h} + K_x \tag{4.2}$$

where η is the instantaneous surface elevation, and $q_x = hu$ is the water flux in the cross-shore direction. h is defined as the total water depth, u represents the cross-shore flow velocity, g is the acceleration of gravity, ρ_w is the water density, τ_b is the bed shear stress, and K_x represents turbulent mixing.

The bed shear stresses are modelled according to Equation 4.3:

$$\tau_{b,c} = \rho_w \frac{g}{C^2} u|u| \tag{4.3}$$

where the Chézy coefficient is given a value of $C = 57$.

A Riemann boundary condition is implemented at the offshore boundary, given by:

$$u_0(t) = (\eta_i - \eta_o)\sqrt{\frac{g}{h_0}} \tag{4.4}$$

where η_i is the incoming tidal elevation at the boundary, and η_0 is the actual elevation at the boundary including reflections from the domain.

Waves

Cross-shore wave transformation is computed from the wave energy balance:

$$\frac{\partial E c_g}{\partial t} + \frac{\partial E c_g \cos\theta}{\partial x} + \frac{\partial E c_\theta}{\partial \theta} = -D_w - D_s \tag{4.5}$$

where E is the wave energy per unit area, c_g is the group celerity, θ is the mean wave direction, D_w represents wave dissipation due to depth-induced breaking, and D_v represents wave dissipation by the structures. Here we assume that wave dissipation by bed friction is an order of magnitude smaller than the energy loss due to wave breaking or due to wave dissipation by the structures.

Wave dissipation due to depth-induced breaking is computed using the formulation of Baldock *et al.*[9]:

$$D_w = 0.25\alpha Q_b \rho_w g f_m (H_b^2 + H_{rms}^2) \tag{4.6}$$

where α is a calibrated parameter, which is set to a value of 1 in the simulations. Q_b is the fraction of breaking waves, f_m is the mean wave frequency, H_b is the breaking wave height, and H_{rms} is the root mean square wave height. The fraction of breaking waves is calculated as:

$$Q_b = \exp\left(-\left(\frac{H_b}{H_{rms}}\right)^2\right) \tag{4.7}$$

where the breaking wave height is modelled as:

$$H_b = \frac{0.88}{k}\tanh\left(\gamma\frac{kh}{0.88}\right) \tag{4.8}$$

with k being the wave length and γ an empirical parameter, which is given a value of 0.7.

Wave dissipation by brushwood structures is modelled using the formulation of Suzuki *et al.*[141]:

$$D_s = \frac{1}{2}\sqrt{\pi}\rho_w c_{D,bw} d N_v \left(\frac{kg}{2\omega}\right)^3 \left(\frac{\sinh^3 kh + 3\sinh kh}{3k\cosh^3 kh} + \frac{\cosh^3 kh - 3\cosh kh + 2}{3k\cosh^3 kh}\right) H^3 \tag{4.9}$$

Where $c_{D,bw}$ is the bulk drag coefficient under waves, d is the diameter of the brushwood, and N_v is the brushwood density per unit area. Here we assume that most of the dissipation caused by a brushwood structure is produced by the brushwood filling, since the vertical bamboo poles have a structural purpose and they are therefore sparsely placed, which reduces wave attenuation through them (see Chapter 3).

The wave-induced shear stresses are given by:

$$\tau_{b,w} = \frac{1}{4}\rho_w f_w u|u| \tag{4.10}$$

with f_w being the wave friction factor, defined as:

$$f_w = min\left(\exp\left(-6 + 5.2\left(\frac{u_{rms}}{2.5 D_{n50}\omega_m}\right)^{-0.19}\right), 0.3\right) \tag{4.11}$$

where the near-bed velocity u_{rms} is calculated from linear wave theory.

Sediment

Morphological bed level changes are calculated from the balance between sediment erosion and deposition, according to Equation 4.12:

$$\frac{\partial z_b}{\partial t} = M_f \frac{D + E}{\rho_s} \tag{4.12}$$

where z_b is the height of the sea bed, M_f is a morphological acceleration factor, and ρ_s is the sediment density.

Sediment erosion is calculated using the approach of Mariotti and Fagherazzi[90], which considers two erosion terms:

$$E = E_{shear} + E_{break} \tag{4.13}$$

The left erosion term, E_{shear}, is given by the shear stresses acting on the bed due to waves and currents:

$$E_{shear} = max\left(m_e\left(\frac{\tau_{b,s}}{\tau_{cr}} - 1\right), 0\right) \tag{4.14}$$

with m_e being a calibration coefficient, $\tau_{b,s}$ being the shear stress at the bed, and τ_{cr} being the critical shear stress for erosion of the local sediment.

The shear stress at the bed is computed as the linear summation of the shear stresses caused by waves ($\tau_{b,w}$, given by Equation 4.3) and currents ($\tau_{b,c}$, given by Equation 4.10):

$$\tau_{bs} = \tau_{b,w} + \tau_{b,c} \tag{4.15}$$

The right erosion term in Equation 4.13, E_{break}, represents the erosive effect of turbulence generated by wave breaking:

$$E_{break} = max\left(\beta\left(\frac{P}{P_{cr}} - 1\right)/d, 0\right) \tag{4.16}$$

where P is the wave power per unit area dissipated by wave breaking, P_{cr} the critical wave power threshold for erosion, and d is the length over which E_{break} occurs, which is set equal to the cell length.

Sediment deposition is modelled as:

$$D = cw_s \tag{4.17}$$

with c being the depth-averaged sediment concentration and w_s the sediment fall velocity.

The sediment concentration is computed from the advection-diffusion equation:

$$\frac{\partial ch}{\partial t} + \frac{\partial uch}{\partial x} - \frac{\partial K_c h \frac{\partial c}{\partial x}}{\partial x} = E - D \tag{4.18}$$

where K_c is the sediment diffusion coefficient. The boundary condition for Equation 4.18 is given by an equilibrium concentration at the seaward boundary, obtained assuming a balance between erosion and deposition.

In order to emulate the potential sediment supply by a local river or creek, in a set of scenarios we impose several values of additional sediment concentration along the cross-shore profile. These values are linearly summed to the output of Equation 4.18, to calculate their effect on the deposition flux, but they are not used as an input in Equation 4.18. This additional concentration is given a maximum value at the location of the minimum water depth (i.e. c^*_{max} at $h = 0.1$ m), and it decreases towards seaward locations according to:

$$c^* = \frac{c_{max} h_{min}}{h} \tag{4.19}$$

where c^* is the local concentration at a grid point with a water depth equal to h. Thus, in the scenarios with an external sediment supply the total deposition flux used in Equation 4.12 is given by:

$$D^* = D + c^* w_s \tag{4.20}$$

The effect of subsidence on the profile is modelled by lowering the bathymetry at every timestep, according to the prescribed subsidence rates.

4.3.5. Validation of wave transformation through structure

Predictions of wave dissipation by the structures in XMgrove were validated against the field measurements. The wave measurements of the seaward frame were propagated seawards until the offshore model boundary to extend the domain, and thus increase the distance between the model boundary and the structures. This was possible because, for the validation test, we placed the offshore boundary at a location where the bathymetry locally became shallower (so the seaward boundary had a smaller water depth than the structure). The transect was modelled with a grid size of $dx = 10$ m and the dissipation by the structures was modelled using Equation 4.9. The average branch size of the brushwood bundles and the branch density were determined by counting the number of branches and measuring their size. This resulted in a brushwood density of $N_v = 400$ elements/m^2, a mean brushwood diameter of $d = 0.025$ m, and a structure width of $w = 0.7$ m. We used a drag coefficient of $c_{D,bw} = 2$ based on the measurements of Chapter 3 for dense cylinder arrays. The bed level was assumed static in this computation, since we modelled a short period of time with calm conditions during which bed level changes were negligible.

4.3.6. Validation of the morphodynamic processes

The morphodynamic module was tested against the coastline change measurements over a NW monsoon season by van Bijsterveldt *et al.*[156]. Their study analyzed satellite images of Demak collected at low tide, and classified every pixel as either water, mud, sand or vegetation. This classification provided information of how the

mudflats changed between 2015 and 2019, and of how the vegetation responded to variations in mudflat width. Since the bathymetry collected in November of 2018 was obtained at the same time as the last satellite picture of 2018, we modelled the monsoon period between November of 2018 and March of 2019.

The bathymetry was extended landwards 400 m from the last measured point emulating the shape of a profile measured at a nearby site[160]. The model domain was also extended 600 m seawards until water depth of $h = 6$ m, in order to avoid wave breaking at the model boundary. This seawards extension was done with a bed slope of $m = 0.002$, based on the offshore bathymetries collected by Tas *et al.*[149] in November of 2018. The time-series of offshore wave data during this period were obtained from Wave Watch III, and the offshore wave heights were propagated from deep water to the water depth the offshore model boundary. Wave Watch III data and field measurements of Demak were compared by Reniers et al.[121], who found a good agreement between them. The tide was prescribed using the tidal constituents derived by Tas *et al.*[149]. The sediment characteristics were chosen based on laboratory analyses conducted in the Netherlands with mud samples from Demak[37]. These analyses provided values for the sediment density, $\rho_s = 585$ kg/m^3, and for the fall velocity, $w_s = 0.07$ mm/s. The grain size was obtained from the average values measured in mudflats by van Bijsterveldt *et al.*[156], with $d_{50} = 7\mu$m. The diffusion coefficient was set to $D = 0.01$ m^2/s, which was estimated as the product of the maximum mean flow velocity and water depth in the domain. The empirical parameters of the erosion term due to wave breaking (Equation 4.16) were set to $\beta = 5\ 10^{-5}$ and $P_{cr} = 0$, as Reniers et *al.*[121] found these values suitable for Demak.

The structure properties were set equal to those of Section 4.3.5. Wave transformation through the structures was validated for relatively calm conditions (Section 4.3.5), whereas the structure performance could differ for larger storm waves during the NW monsoon. However, flume experiments with dense arrays of cylinders showed that the drag coefficient under relatively larger waves had a value of approximately $c_{D,bw} = 2$, which suggests that using this value is a reasonable assumption for storms.

During the NW monsoon of 2018-2019 the coastline retreated by 56 m at the low water line (for z = -0.3 m)[156]. The erodibility parameter m_e was thus calibrated to reproduce a coastline retreat of 50 m during the NW monsoon. We used a morphological acceleration factor of $M_f = 5$, since it provided comparable results to $M_f = 1$ (Figure C.1 e and f in Appendix C).

4.3.7. Influence of structure design on its performance

Effect of structure location

After its calibration, the model was applied to investigate how to optimize the structure design for the conditions of the NW monsoon of 2018-2019. During this period the coastline retreated although a structure was present in the profile. The model was used to test if a different structure location could have led to coastline expansion during this period. The structure location was thus varied between $z = +0.25$ m and $z = -1$ m with respect mean sea level (MSL). The remaining structure properties were kept constant ($w = 0.7$ m, $N_v = 400$ elements/m^2,c$_{D,bw} = 2$), and the wave conditions and sediment properties were set equal to those of Section 4.3.6.

4.3.8. Effect of structure width

In an additional set of runs we investigated the effect of structure width in the cross-shore direction, which was varied between $w =$ 0.25-5 m. All tested structures were located at 0.3 m below MSL, and the remaining structure properties were kept equal to those of Section 4.3.7.

4.3.9. Effect of brushwood density

The structures built in Demak experienced severe degradation as their brushwood filling was lost due to wave action, which caused high maintenance costs and the eventual collapse of the some of the structures. We thus tested several element densities, ranging from $N_v = 50$ elements/m^2, until $N_v = 800$ elements/m^2, to investigate (1) the optimum brushwood density to cause coastline advance, and (2) the potential effect of the loss of brushwood on structure performance. All tested structures were located at 0.3 m below MSL, and the remaining structure properties were kept equal to those of Section 4.3.7.

4.3.10. Effect of chenier on structure performance

Several structures of the Building with Nature project were built landwards from cheniers, which are dynamic sand lenses found in the intertidal zone. Cheniers fully block waves during low water, and break or dissipate them during high tide, reducing wave action landwards. To test the effect of a seaward chenier on structure performance, we modelled the effect of structures placed at 0.3 m below MSL during a monsoon season with and without the presence

of a chenier. The cheniers were represented as unerodible barriers with a fixed height, since in its current version the model only reproduces the transport of a single sediment fraction.

4.3.11. Effect of subsidence and sediment supply

Over timescales longer than a year the build-up of intertidal mudflat behind the structures may be strongly influenced by the subsidence and the local sediment supply. Measured subsidence rates in the Demak region vary between 0-0.16 m/year[174]. We consequently tested several scenarios with subsidence rates between 0-0.16 m/year. The sediment input into the area of Demak is not known, and we thus studied several scenarios of sediment supply across the profile (Equation 4.19), varying between 0-0.08 g/l. The model was run for 4 consecutive years, since the structures are designed to restore the bed profile within 2-5 years. The 4-year simulations were obtained by repeating the wave climate time-series of 2017-2018 four times. We chose those wave conditions because they corresponded to a particularly stormy year, which included the largest storm during the interval 2015-2019 and the largest coastline retreat rate observed by van Bijsterveldt *et al.*[156].

4.4. Field measurements and model results

4.4.1. Field data

The hydrodynamic measurements seawards and landwards from brushwood structures are shown for August of 2017 (T1) and November of 2018 (T2) in plots (b) to (i) of Figure 4.5. The time intervals when the sensors were emerged (and thus not recording properly)

are illustrated by blue shaded areas. We have also included the full wave climate from Wave Watch III in Figure 4.5 (a) to contextualize our measurements in the yearly wave climate. The Wave Watch III data do not include local wave effects, which dominate the wave climate during the SE monsoon season. However, locally generated waves are much smaller than the monsoon waves of the NW season[2], which are present in the Wave Watch III dataset.

During August 2017, the wave height was approximately equal to $H_{m0} = 0.05$ m during most of the time, except for a period of slightly higher waves ($H_{m0} = 0.07$ m) on the 6^{th} of August. The differences in wave height in front and behind the structures were almost negligible most of the time except for a short period during the 6^{th} of August. During November 2018, wave heights in front of the structures reached values of approximately $H_{m0} = 0.05$ m during the morning, and higher values with maximum of $H_{m0} = 0.18$ m in the afternoon, associated to the local sea breeze. The wave transmission measurements showed similar behaviour as in the summer; small waves travelled undisturbed through the structures, whereas higher waves experience minimum transmission rates of 60% with respect to the incoming wave energy flux (Figure 4.6 b). During November 2018 we aimed to measure storm waves caused by the NW monsoon, since the first storm events usually take place in this period, but unfortunately the conditions were unusually mild until January.

The mean wave periods remained approximately equal to $T_m = 5$ s in the August 2017, and between $T_m = 2$-5 s in November 2018. In both cases, waves were short, since the Java Sea is shallow and sheltered, which prevents the propagation of swells into the sea.

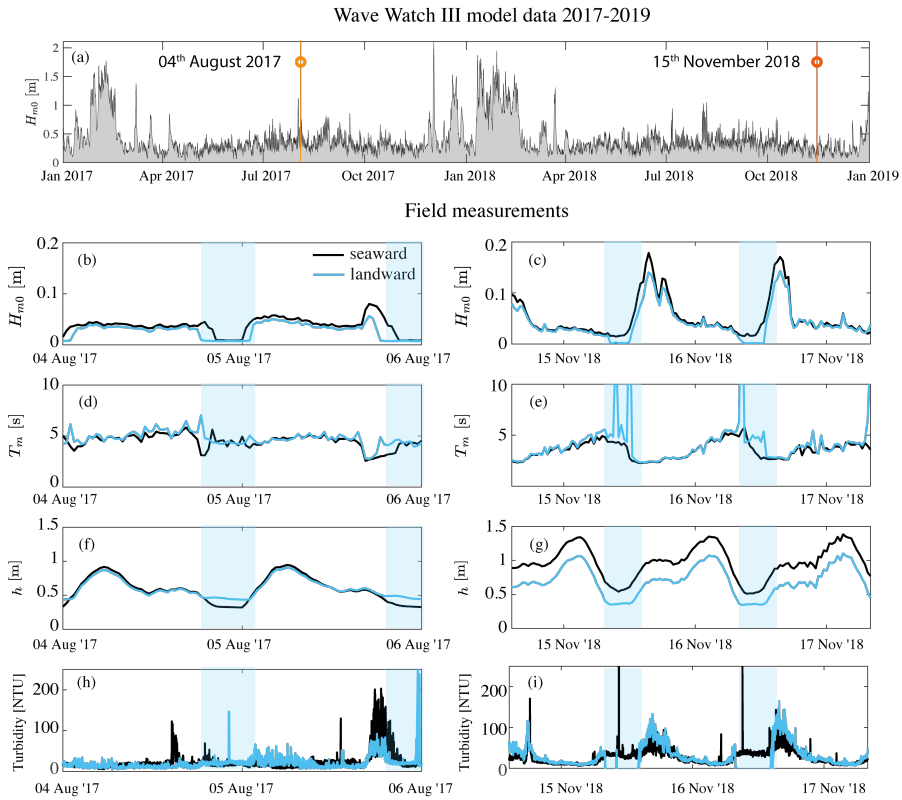

Figure 4.5: (a) Offshore significant wave height from Wave Watch III model during 2017-2019. (b) Measured significant wave height, (d) mean wave period, (f) water depth and (h) turbidity measured at T1 in August of 2017, seawards (black) and landwards (blue) from a structure. (c) Significant wave height, (e) mean wave period, (g) water depth and (i) turbidity measured at T2 in November of 2018, seawards (black) and landwards (blue) from a structure. The periods when the sensors were emergent (and thus not recording properly) are shown by blue shaded areas. Both field campaigns took place during relatively calm periods, where the effect of the structures on waves was small.

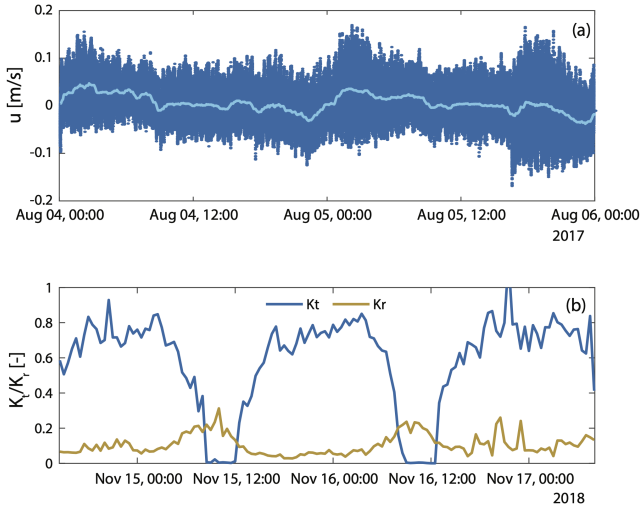

Figure 4.6: (a) Instantaneous velocity (dark blue) and average over 20-minute intervals (light blue) at T1, measured by an ADV placed at the seaward side of a structure, at a distance from 0.33 m from the bed. (b) Fraction of the wave energy flux that is transmitted (dark blue line) and reflected (brown line) through the structure of T2. The lowest transmitted ratios (60 %) are observed just after low water, when the highest waves occurred due to the local sea breeze. The drop in wave transmission corresponded with the periods when the landward sensor was emergent. The wave flux reflection rates oscillated around 5 %.

The water depth was very similar landwards and seawards from the bamboo and brushwood structure (T1) monitored in August 2017. For the brushwood structure monitored in November 2018 (T2), the front side of the structure was 0.2 m deeper than the land side. This difference in water depth cannot directly be attributed to erosion or subsidence between 2017 and 2018, as the location of these two transects is not identical due to the collapse of the structure of 2017.

The mean flow velocities are an order of magnitude smaller than the total velocities (Figure 4.6 a), which were mostly wave-driven. The turbidity measurements also displayed the same behaviour as the significant wave height, with lower turbidity values during low waves and more stirring associated to larger wave heights. We estimated the wave-driven shear stresses at the bottom using Equation 4.10, calculating the flow velocities from the measured wave properties using linear wave theory. Comparison of the shear stress estimates and the turbidity time series suggests that local erosion occurs for local shear stresses larger than τ_{cr} =0.02 N/m^2.

4.4.2. Model results

Wave transformation through structures

The model validation is shown in Figure 4.7. We tested the results of the model without modelling the structures (yellow line) and by modelling wave dissipation by the structures (brown line) against the measured waves (black dots).

The model was able to reproduce the wave height seawards from the structure (Figure 4.7). Neglecting the wave dissipation by

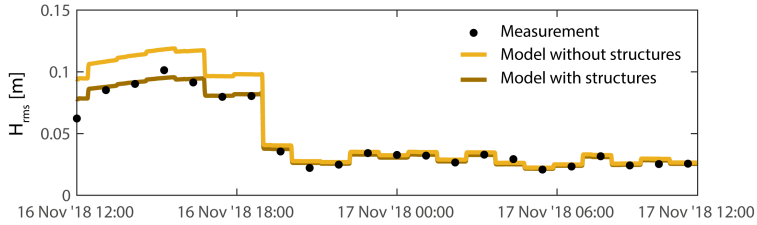

Figure 4.7: Comparison between measurements (black dots) and predictions of wave transformation of XMgrove, neglecting the presence of a brushwood structure (yellow) and including wave dissipation by the structure (brown).

the structures resulted in a (maximum) 38% over-prediction of the wave height, with the largest difference corresponding to the highest waves (between 15.00-18.00 on the 16^{th} of November), which experienced most wave attenuation. Since the structures had a negligible effect on waves during calmer conditions, the results of the model with and without structures are similar after the 17^{th} of November at 19.00.

Validation of morphodynamic processes

The erodibility parameter that reproduced the a coastline retreat of 50 m in the model was equal to $m_e = 2.0\ 10^{-4}$ kg/s/m^2. The results obtained with this m_e value are illustrated in Figure 4.8. The upper subplots of Figure 4.8 show the mudflat area at Demak before the NW monsoon (left), and after the monsoon (right). The modelled shape of the profile after this period is shown in Figure 4.8 (c). Coastal erosion in this period was dominated by the bottom stresses due to waves and currents (Equation 4.15), while the erosion term due to wave breaking-induced turbulence (Equation 4.16) had a negligible effect on the bed level. The model sensitivity

to different values of the sediment properties is shown in Figure C.2 of Appendix C.

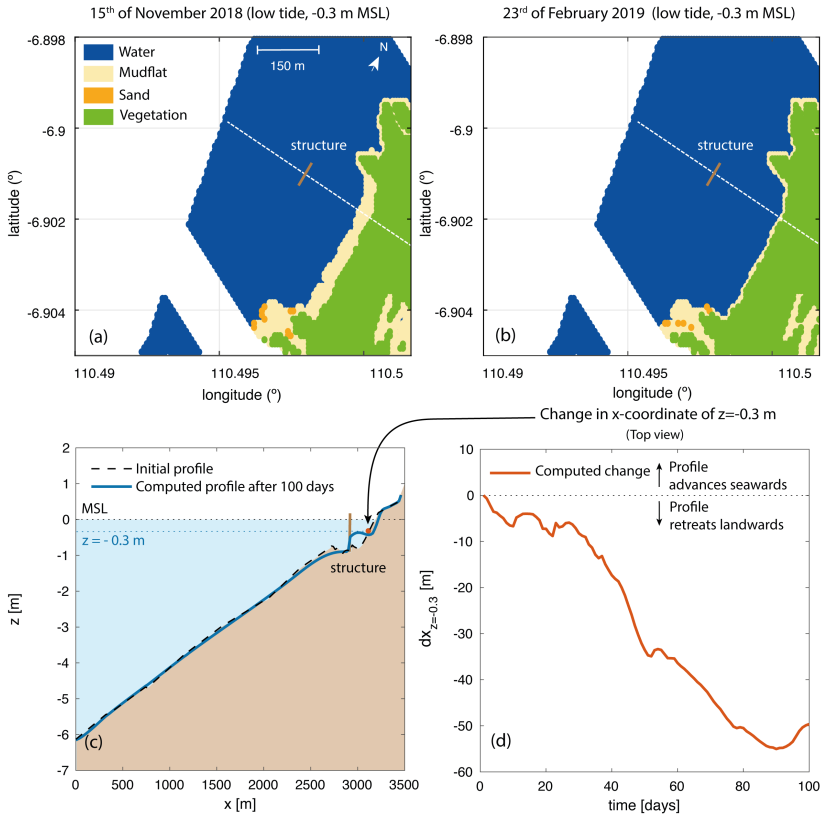

Figure 4.8: Processed satellite images of Demak from van Bijsterveldt *et al.*[156] in (a) November of 2018 and (b) February of 2019. Plot (c) shows the initial bathymetry of the model, measured in November of 2018, and the model results for February 2019. The change in coastline position at low tide (i.e. at z = -0.3 m with respect to MSL) from the model is shown in plot (d).

Influence of structure location on the coastline position

The influence of the water depth at the structure is shown in Figure 4.9 (a) and (b).

Erosion is predicted seawards of the structures for all conditions, and accretion at their land side (Figure 4.9, a). This behaviour is caused by the difference in wave height at both sides of the structure, which generates a gradient in concentration, and a net landwards sediment flux by the tide (see Figure C.1 a of Appendix C).

The structure placed 0.3 m below MSL is the most efficient during a NW monsoon season, although it is still insufficient to stop coastline retreat (Figure 4.9, b). Structures at deeper water cause significant accretion behind them, but their accretive effect has a relatively smaller influence on the coastline position (here defined as the location where $z = 0$ m), resulting in more retreat. Structures located above MSL are submerged during a relatively small fraction of the tidal cycle, and leave seaward areas exposed to the erosive action of waves.

Influence of structure width

The effect of varying the structure width for a structure placed at the most optimal depth for a NW monsoon season (-0.3 m with respect to MSL) is shown in Figure 4.9 (c) and (d). Widths smaller than 1 m cause coastline retreat (Figure 4.9, d), whereas larger widths lead to coastline expansion.

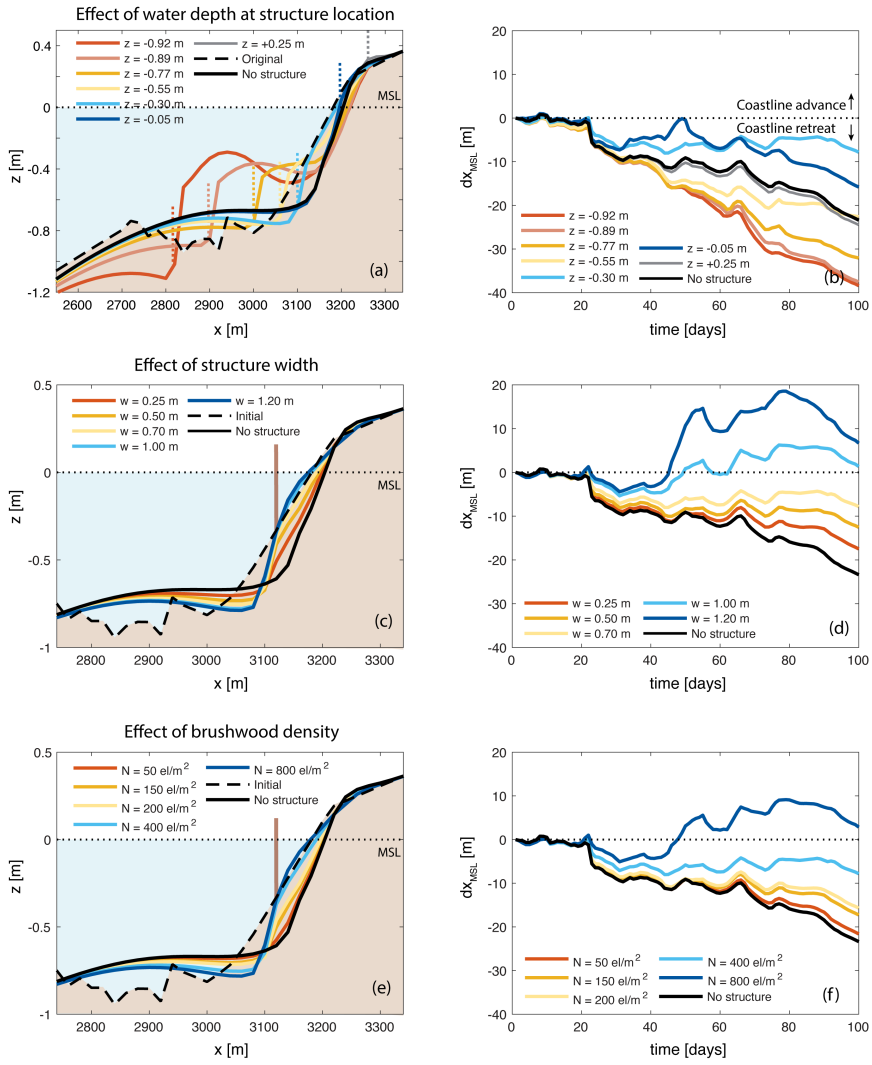

Figure 4.9: Effect of different structure designs for the monsoon season of 2018-2019. Plots (a) and (b) show the effect of varying structure locations, where the location of the structures is shown in colored dashed lines, plots (c) and (d) show the effect of varying the structure width, and plots (e) and (f) show the effect of varying the brushwood density. The structure location in plots (c) and (e) is shown by a light brown line. The left plots illustrate the impact of the structures across the profile, whereas the right plots show their influence on the position of MSL over time.

Influence of material degradation on structure performance

A structure with a density of $N_v = 800$ elements/m^2 can stop coastline retreat during a NW monsoon (Figure 4.9, e), whereas sparser structures cannot fully counteract it. The most pronounced reduction in efficiency is predicted for densities below $N_v = 50$ elements/m^2, which result in an almost negligible effect of the structures on the coastline position (Figure 4.9, f).

Effect of cheniers on structure performance

The influence of cheniers on structure performance is shown in Figure 4.10. Without a structure (Figure 4.10 a) the shoreline retreats over a monsoon season. A chenier with a top height of 0.06 m causes 44 m of coastal expansion. A higher chenier with a top elevation of 0.26 m produces practically the same coastline expansion, with differences of the order of decimeters.

In the absence of cheniers, coastline retreat can be mitigated over a monsoon season by building a structure at 0.3 m below MSL with a width of 1 m (Figure 4.10 b). When the structure is built landwards from a chenier with a top height of 0.06 m, the coastline expands 47 m seawards and its response is dominated by the influence of the chenier. The presence of the highest chenier makes the effect of a structure negligible, as wave attenuation is fully (during low water) or mostly (during high water) caused by the chenier.

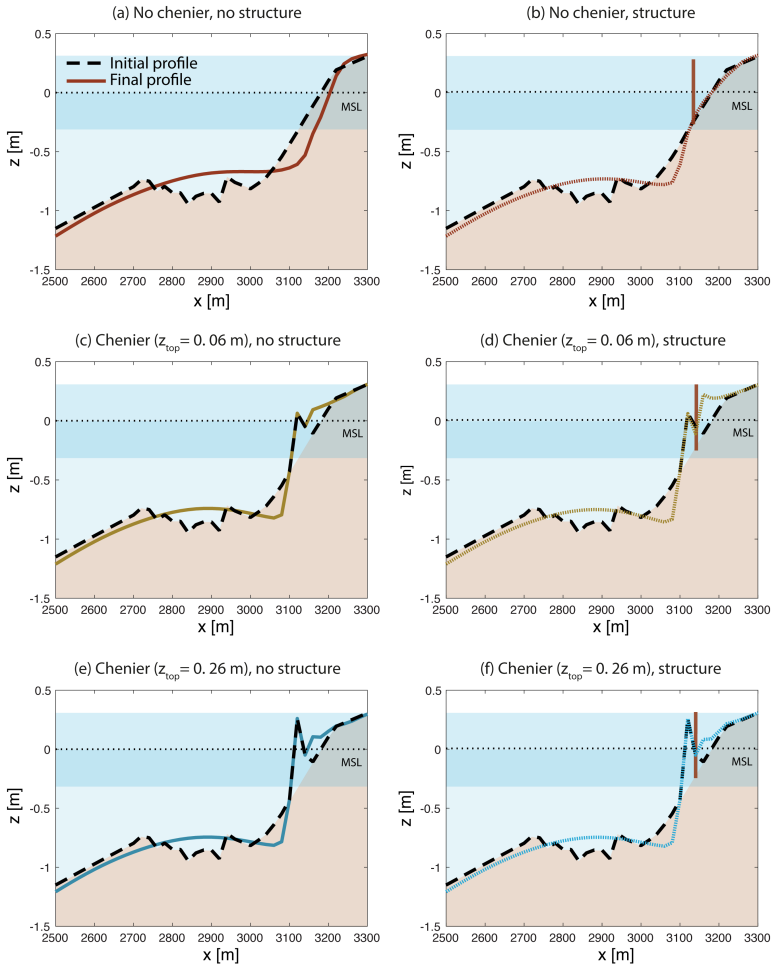

Figure 4.10: Effect of cheniers on structure performance. The reference situation without chenier and structure (illustrated by brown lines) is shown in (a), and the model results without chenier and with a structure placed 0.3 m below MSL are shown in (b). The effect of a chenier with a top height of 0.26 m is shown in plots (c) and (d). The effect of a chenier with a top height of 0.06 m is shown in plots (e) and (f). In both cases, the presence of a chenier made the effect of a structure at 0.3 m below MSL practically negligible. The intertidal areas are shown with blue shaded areas.

Influence of subsidence and sediment concentration on structure performance

The coastline change at MSL for 4-year long scenarios with varying subsidence and sediment supply is shown in Figure 4.11.

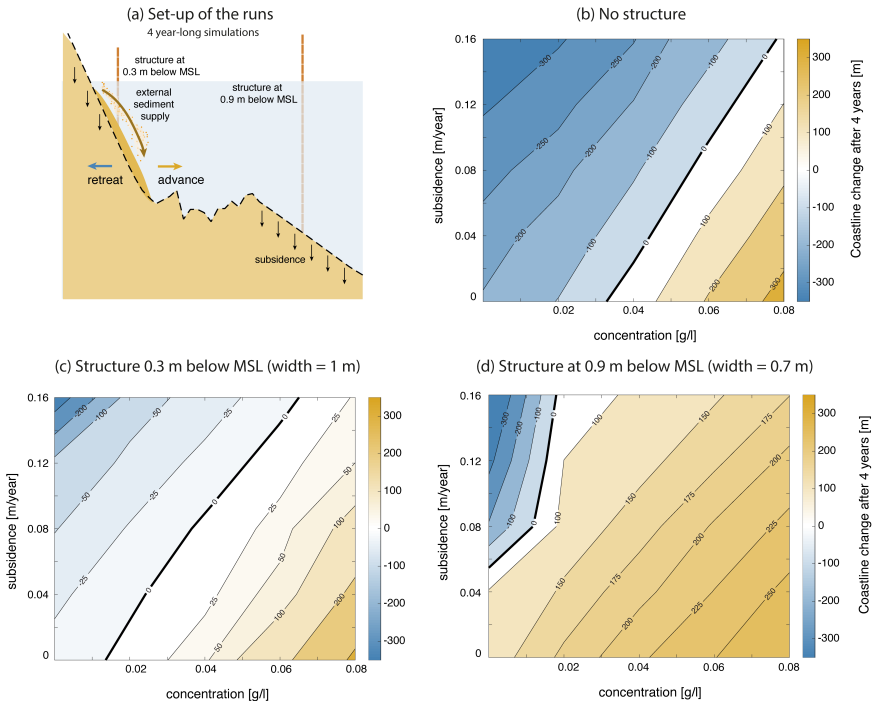

Figure 4.11: Evolution of the coastline of Demak over 4 years for several scenarios of subsidence and external sediment supply, such as rivers. The set-up of the runs is shown in plot (a). The results are presented for a situation without structures (b), with a structure placed at 0.3 m below MSL (c), and with a structure placed 0.9 m below MSL (d).

The coastline erodes in the reference situation without external sediment supply and without subsidence (Figure 4.11, b). This retreat mostly happens during the stormy NW monsoon, whereas during the calmer SE monsoon, the shoreline either remains at the

same location or it partly recovers its original position by expanding seawards (see Figure C.1 g of Appendix C). Higher subsidence rates induce coastline retreat and flooding. Conversely, higher sediment supplies cause accretion and coastline progradation. The net coastline response thus depends on the relative magnitude of the subsidence rate and the ambient sediment concentration.

Structures can mitigate shoreline retreat, as they retain the sediment close to the coast (Figure 4.11 c-d). However, the optimum design varies with the boundary conditions and with the lifetime chosen for the structure. During a NW monsoon season, a structure built 0.9 m below MSL induces sediment deposition but its accretive effects do not reach the MSL line (Figure 4.9 a). Over longer time scales, the accretion induced by the structure generates a wide shallow area near MSL where sediment is deposited, leading to coastline progradation in the 4-year scenarios. For example, without a structure, the coastline would retreat -193 m without subsidence nor external sediment input (Figure 4.11 b), whereas a structure placed at a water depth of 0.9 m causes 134 m of progradation for the same conditions (Figure 4.11 d). Conversely, for high subsidence scenarios structures placed at 0.9 m below MSL actually cause more retreat than in the reference situation without structures (upper left corner of Figure 4.11 d).

Structures placed at a shallower location, 0.3 m below MSL, provide a relatively poorer performance over 4-year scenarios with low subsidence and sediment supply. They still mitigate coastline retreat compared to a situation without structures, for instance without subsidence nor sediment input, the coastline retreats -15 m at the land side of the structure, which corresponds with a 92%

reduction in coastline retreat. However, net progradation is only obtained for external sediment supplies larger than 0.013 g/l. Structures at 0.3 m below MSL are more efficient in reducing coastline retreat than deeper structures for subsidence rates higher than 0.08 m/year and no sediment supply. Nonetheless, they do not stabilize the coastline nor expand it seawards in any of the subsidence scenarios without an external sediment input.

Brushwood structures can be counterproductive in scenarios of low subsidence and high sediment supply, as they reduce coastline progradation compared with the reference situation without structures (see lower right corners of Figure 4.11, b, c and d). Such scenarios of high sediment concentration would not require the presence of a structure, since there would not be any retreat to prevent. Nevertheless, they indicate that a structure at MSL could block sediment transport towards the higher part of the profile during periods of large ambient concentration.

4.5. Discussion

4.5.1. Optimizing structure design

Satellite images show that the permeable structures analyzed in this study were unable to stop coastline retreat during the NW monsoon season of 2018-2019. XMgrove also predicts that the structure design implemented in the field in 2018 does not stop coastline retreat during its first monsoon season. However, the design causes coastline progradation over a 4-year period in modelling scenarios with subsidence rates below 0.05 m/year without external sediment supply, and for higher subsidence rates when the ambient sediment

concentration exceeds 0.015 g/l. Since Google Earth images show that the coastline of Demak continued to retreat behind the structures between 2018-2022, the subsidence rates in Demak are likely larger than the threshold that can be compensated with the local sediment input.

The bamboo and brushwood structures implemented in Demak were designed to redistribute the sediment at sites where mangrove deforestation altered the local balance between erosive and accretive process. Nevertheless, they cannot address structural sediment losses. Sites with high subsidence and low sediment supply conditions would require other coastal protection strategies, such as nourishing the coast or management realignment. Evaluating the feasibility of using structures to create new mangrove habitat thus requires estimating the local sediment budgets and subsidence rates, and assessing how these factors affect the profile evolution.

The optimum design may also vary depending on the morphodynamic timescales of the system compared to the desired mangrove restoration time frame. For instance, structures built 0.3 m below MSL were most efficient in stopping retreat over a NW monsoon season, but structures built 0.9 m below MSL were more optimal over 4-year periods. Structures at other locations could lead to better results over decades and/or at sites where the profile adjusts faster (e.g., due to different forcing and/or sediment properties). Moreover, although erosion due to turbulence generated by wave breaking (E_{break}) had a negligible effect on the scenarios modelled in this study, this process was found relevant for longer timescales by Reniers et *al.*[121]. Changes in the relevant sediment transport mechanisms could also influence the profile evolution at the scale

of decades.

4.5.2. Model limitations

The actual threshold values of subsidence and sediment supply for which the coastline either retreats or advances likely differ from the values of Figure 4.11, as the model results are limited by several assumptions. For instance, the 4-year long model runs were obtained by simulating the wave climate of 2017-2018 four consecutive times. Since the NW monsoon season of 2017-2018 was particularly stormy, this would in principle imply that the threshold concentrations in the field may be lower than the ones predicted in Figure 4.11, but other assumptions and processes may also influence these values. One of the most influential factors in the profile evolution is the initial morphology.

The initial profile illustrated in Figure 4.9 shows a sudden decrease in slope from offshore to nearshore, which in turn causes a abrupt change in the computed morphodynamic processes. The same structure design causes a very different effect in the bed level when smoother convex and concave profiles are used as the initial bathymetry (see Figure C.1 c of Appendix C). Additional runs where we keep the same bathymetry except for the nearshore slopes also show variations in the coastal changes (Figure C.1 b of Appendix C). For instance, more coastline retreat is predicted for a shallower nearshore slope. This implies that predictions of coastal change at one site and the optimum structure design will strongly depend on the local morphology.

The presence of cheniers can also shift the threshold values of

subsidence and concentration with respect to those of Figure 4.11. As shown in Figure 4.10, if a chenier with a top height of 0.26 m above MSL is present seawards from a structure the coastline evolution is dominated by the effect of the chenier, to such extent that the influence of the structure is negligible. However, in the runs of Section 4.4.2 we assume cheniers unerodible as a first approximation. In reality, cheniers can be very dynamic even during calm conditions, as shown by Tas *et al.*[149]. The model by Tas *et al.*[148] for chenier migration and growth could be implemented in XMgrove, in order to investigate how changes in the chenier would affect the structure performance and the coastline evolution.

Cheniers and other coastal features, such as rivers, can also induce 2D effects in the flow and sediment transport. In the case of Demak, severe flooding of the aquaculture ponds has formed tidal basins that fill and empty through narrow creeks. Measured mean velocities were small at the location of T1-T2 (Figure 4.6 a), but close to areas of large flow exchange, currents are likely to reduce the accretive effect of the structures compared to the results of Figure 4.9 and Figure 4.11. At other sites, deposition may actually enhance accretion even further. Such processes can be investigated with a 2D model of the region that includes alongshore variations in the morphology, tidal creeks and rivers. This approach could provide more accurate estimates of the sediment supply needed to compensate subsidence at a regional level.

Assumptions in the sediment transport module can also influence the model results. We assume an equilibrium concentration as an offshore boundary, whereas using a constant or time-varying sediment influx, could change the timing and magnitude of the

sediment brought into the system. In a separate set of runs we test having three values of constant concentration at the offshore boundary (Figure C.1 d of Appendix C). Varying the concentration affects the results within the first 750 m of the domain (for a total domain length of 3,500 m), but it does not have a significant effect on the nearshore region. However, knowledge of the sediment input is particularly important for the alongshore boundary condition for the sediment concentration, as the evolution of the profile was highly influenced by the external ambient concentration (Figure 4.11). This would require long-term data of the flow velocities and sediment concentrations along the coastal area.

Longer time series of wave transformation through the structures would also indicate whether the assumptions used in Sections 4.3.7-4.3.11 hold for storm waves. We also assumed that the structure remained intact during the model simulations, whereas partial or total loss of the brushwood filling could occur during storm events. Including wave reflection by the structures would also influence their morphodynamic performance.

Lastly, there are inherent model inaccuracies due to neglecting changes in flow and sediment properties along the vertical coordinate. For example, sediment consolidation would decrease the erodibility of the sediment deeper into the ground. Sediment consolidation would also decrease bed level height over time, reducing the effect of the structures compared to the predictions of Figure 4.11. These processes could decrease the bed level behind the structures, which would shift the thresholds for coastline expansion of Figure 4.11.

Additional ecologic requirements

Our work focused on maximizing coastline expansion to ensure mangrove recovery, but in reality additional bio-physical requirements will limit mangrove establishment. Natural mangrove colonization can be limited by factors such as low seed availability[79], seedling dislodgement due to wave action[12,11,10], or seedling uprooting and burial[12,11,10].

Van Bijsterveldt *et al.*[158] installed a network of seed traps along the coast of Demak, which demonstrated high seed availability throughout the area. Pulling experiments with Avicennia marina seedlings, the pioneer species in Demak, showed that their anchoring forces were two order of magnitudes larger than the local wave forces during calm conditions. However, seedlings younger than 1 month, with lower anchoring forces, could be particularly vulnerable to dislodging during storm events[12]. Seedlings could also be uprooted due to erosion, even in scenarios where structures stop coastline retreat. For example, without subsidence and without sediment supply, a structure at 0.9 m below MSL can mitigate shoreline retreat and cause 134 m of progradation (Figure 4.11, d), but there are still 12 cm of vertical erosion along the higher part of the profile.

The largest peek in seed production of Avicennia marina in Demak coincides with the NW monsoon, when the wave attack and the erosion rates are largest. Sowing seedlings after the NW monsoon, by April-May, could give mangroves approximately 6-7 months to develop in undisturbed conditions until the next NW monsoon season. During this calmer period, mangroves could grow their roots, which would enable them withstand higher loads and higher ero-

sion depths during the next NW monsoon. This potential strategy could be investigated by applying XMgrove with a dynamic vegetation model that reproduces vegetation establishment, growth, and mortality. Mangrove colonization would also decrease the shear stresses on the bed and increase its shear strength, reducing erosion in the following years[162].

Besides including vegetation dynamics in morphodynamic modelling, another important step towards implementation is the development of mangrove mapping tools for eroding coastlines. Including mangrove restoration in coastal management requires systematic ways to find potential mangrove sites. However, existing mangrove mapping methodologies disregard eroding coastlines and classify them as unrestorable, which leaves out a considerable number of potential restoration sites. The following chapter explores how to find potential sites for restoring mangroves with structures using open-access data sets.

5. Mapping mangrove opportunities

5.1. Introduction

Integrating mangrove restoration and management in coastal protection plans requires tools to identify potential mangrove sites. Existing mapping methods have classified eroding coastlines as unsuitable for restoration, which neglects many areas that could potentially be recovered with bamboo structures. The aim of this chapter is thus to develop a mangrove mapping methodology, which is applied to the case study of Bangladesh. This chapter was made possible with financial support from the Japan World Bank Program for Mainstreaming Disaster Risk Management in Developing Countries, and technical support from its implementing arm, Disaster Risk Management Hub, Tokyo. The content of this chapter is included in the following publication:

A. Gijón Mancheño, P.M.J. Herman, S.N. Jonkman, S. Kazi, I. Urrutia, and M. van Ledden (2021). Mapping Mangrove Opportunities with Open Access Data: A Case Study for Bangladesh. Sustainability, 13(15).

5.2. Mangrove ecosystem services and restoration

5.2.1. Coastal protection in Bangladesh

Bangladesh was the 7th most-affected country by extreme weather events between 1999-2018 due to a confluence of reasons[39]. Cyclones regularly sweep the coastline of the Bay of Bengal, and funnel into the narrowing shape of the bay at Bangladesh[73]. The country is also low-lying and densely inhabited, which exposes a large population to the effect of surges. Besides cyclones, massive rains during the monsoon have also caused floods across the country[67]. This vulnerability to weather events is only likely to increase over the next century due to climate change and the expected population growth, setting a strong need for coastal defence measures.

The coastal zone of Bangladesh is currently protected by a system of 139 polders. These are surrounded by approximately 6,000 km of peripheral embankments, which were built in the 1960-1970s to prevent tidal flooding[135]. Their construction protected lives and livelihoods[114], and increased agricultural production by 200% to 300% in some areas[110]. Over time, river siltation combined with poor infrastructure maintenance caused drainage problems and water logging at some polders[105,7]. Moreover, since the embankments were not designed to contain surges, breaching events have taken place during some cyclones[64]. The embankment system is thus being upgraded to a higher safety standard by the Coastal Embankment Improvement Project – Phase 1 (CEIP-1), as the first phase in a potential series of projects to upgrade all polders along the coastal zone in Bangladesh.

The CEIP-1 project has several components, such as the reinforcement of 10 polders to a 25-year level of protection, and afforestation schemes seawards from embankments[65]. The scope of the afforestation works includes planting commercial species for economic purposes, and planting mangroves for coastal protection. Mangroves attenuate waves and currents[93,13,91,56], but have a limited effect on storm surges[76,99]. Since surge heights in Bangladesh often range between 3-5 m[70,175], embankments are necessary to fully protect coastal polders from flooding. However, by reducing wave impacts and wave run-up on embankments, mangroves provide additional coastal resilience, and potentially reduce the costs of upgrading embankments[153,154].

Bangladesh is home of the largest continuous mangrove forest in the world, the Sundarbans, and it has a long history of mangrove afforestation. Mangrove planting schemes have stabilized 150,000 ha of coastal land since 1966, and additional afforestation opportunities may be present along the coastal system[124]. However, existing methodologies for mangrove opportunity mapping are limited for the case of Bangladesh. For instance, Worthington and Spalding[171] identify mangrove areas lost all over the world since 1996, and estimate their restoration potential depending on the local conditions. However, most of the mangrove losses in Bangladesh happened between 1873-1933[62], and they are thus neglected by their mapping methodology. Afforestation opportunities (i.e., planting in areas not previously inhabited by mangroves) would not be identified by this method either.

The aim of this work is thus to develop a systematic screening method to map mangrove opportunities seaward from embank-

ments, which we applied to the case-study of Bangladesh. The methodology is conceived as a first screening technique based on readily available data, which helps identify sites to be investigated in subsequent more detailed studies. This methodology could also be valuable for other tropical countries facing increasing challenges with rising sea levels[109]. The following sections discuss the potential and limitations of coastal protection by mangroves, and the factors to consider in the screening methodology.

5.2.2. Coastal protection by mangroves

The protective role of mangrove vegetation against coastal hazards results from the combination of several mechanisms, illustrated in Figure 5.1. Mangroves exert resistant forces against waves and currents[93,92], and fix coastal sediments in the sea bed with their root system. The lower erosive forces combined with higher sediment stability reduce erosion and favor sediment deposition[151]. Sediment accumulation also reduces the water depth, limiting the highest waves that can propagate into the forest without breaking.

The wave attenuation efficiency of mangroves depends on several factors, such as wave characteristics, tree species, tree geometry, and the total extent of the vegetation[93,13]. In practice this implies that the forest width required to dissipate waves is site-specific. For instance, a minimum value of 100 m is often used as a reference for coastal protection[168], but Bao[13] observed that the required width for wave attenuation depended on the forest structure, with smaller widths being necessary for taller and denser forests, as shown in Figure 5.2.

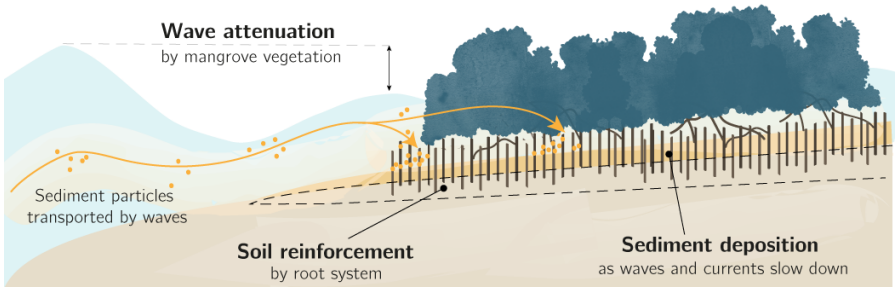

Figure 5.1: Diagram illustrating coastal protection by mangroves. Waves attenuate as they propagate through the forest. As a consequence, any sediment particles transported by the flow can deposit between the trees. The mangrove root system stabilizes the soil, further enhancing an increase in the bed level.

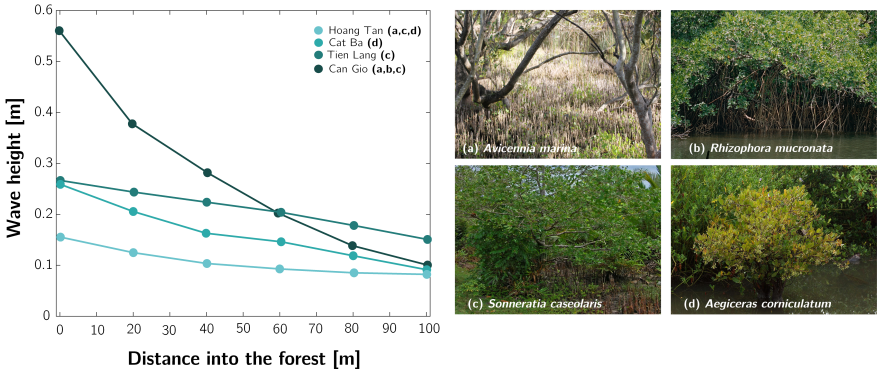

Figure 5.2: (Left) Wave transmission rates through four mangrove forest sites in Vietnam, adapted from Bao[13]. (Right) Pictures of the main species identified by Bao et al.[13] in the monitored transects: (a) Avicennia marina (by Alison Klein, CC0 1.0 from Flickr), (b) Rhizophora mucronata (by Bernard Dupont, CC BY-SA 2.0 from Wikimedia), (c) Sonneratia caseolaris (by Shagil Kannur, CC BY-SA 4.0 from Wikimedia), (d) Aegiceras corniculatum (by Vengolis, CC BY-SA 3.0 from Wikimedia).

Wave attenuation also varies with wave length, as illustrated in Figure 5.3. Wind waves, i.e., locally generated storm waves, can experience higher wave height reduction over a 100 m belt than swell waves, which are longer waves generated hundreds or thousands of kilometers away from the shoreline. Figure 5.2 also suggests that a mangrove belt width of 1 km would probably be more similar to the distance required to fully attenuate the longer swell waves, and even longer widths would be required to dissipate a tsunami, with wave lengths of hundreds of kilometers.

This does not imply that mangroves do not provide any protection against relatively longer waves. Vegetation can stabilize and maintain a sediment level that would be unstable without vegetation, affecting both the height and the form of the coastal profile. The presence of the vegetation can also decrease the run-up height and flow velocities under tsunamis, mitigating their effects, as observed in south-east Asia after the tsunami of 2004[145,143,71].

Surges can be considered as waves with very long periods, from a few hours to several days[99]. Following the reasoning illustrated in Figure 5.3, extensive mangrove forests would be needed to effectively dampen surges. Field observations have also shown limited surge reduction by mangroves, with attenuation rates of 9.4-24 cm/km through vegetated areas[76,100].

Since surge heights between 3-5 m are frequent in Bangladesh[175], some form of structure at the land side will always be needed to protect against flooding. However, surges can occur simultaneously with locally generated wind waves, with heights of 3 m at the exposed coastline[119]. The attenuation of these shorter waves by a mangrove belt would reduce the run-up height on coastal embank-

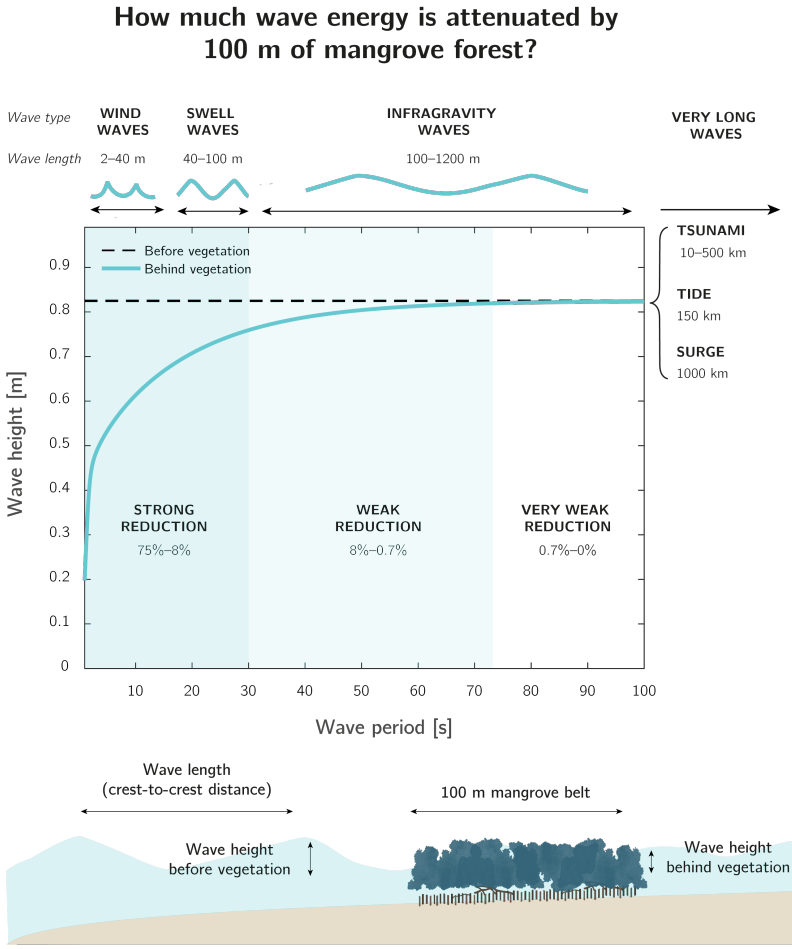

Figure 5.3: Diagram illustrating the amount of wave reduction for fixed value of incoming wave height and varying wave periods through a 100 m-wide mangrove belt. The diagram was derived using the model of Mendez and Losada[97] with mangrove vegetation parameters obtained from Suzuki[139]; vegetation density of 1.1 trees/m^2 and tree diameter of 0.27 m. The results were obtained with a water depth of 1.5 m and a wave height of 0.8 m (maximum wave height possible with a breaking ratio of 0.55). The wave lengths indicated in the figure are also calculated for a water depth of 1.5 m.

ments, potentially decreasing the costs of slope and bank protection, and the required crest height of the structures. The economic benefit of including mangroves for coastal protection will depend on site-dependent aspects like the costs of mangrove restoration and maintenance, or the land value.

5.2.3. Finding suitable locations for mangroves foreshores

Identifying opportunities for mangroves along the coastal system relies on knowledge of their habitat. Mangroves grow at depositional intertidal areas with low wave action and freshwater input[4]. Natural recruitment can take place on newly accreted land that satisfies the physical conditions required by mangroves (Figure 5.4 a), as long as there is a nearby supply of mangrove seedlings.

Similarly, if mangroves are removed at one site but the local conditions remain suitable for them, the vegetation may also recolonize naturally[80]. For instance, natural regeneration has taken place after deforestation in mangrove forests of Baja California[163] and Kenya[66]. When a mangrove site is degraded and the habitat requirements are no longer satisfied, the habitat should be restored to enable vegetation recruitment[80]. The required technique depends on the cause of mangrove absence, as illustrated in Figure 5.4.

If human activities reduce seedling availability, planting schemes can accelerate mangrove establishment[80] (Figure 5.4 d). Such planting efforts should be planned based on knowledge of the local ecology[80]. Although mangroves are generally present between mean sea level (MSL) and the highest astronomical tide (HAT), different species

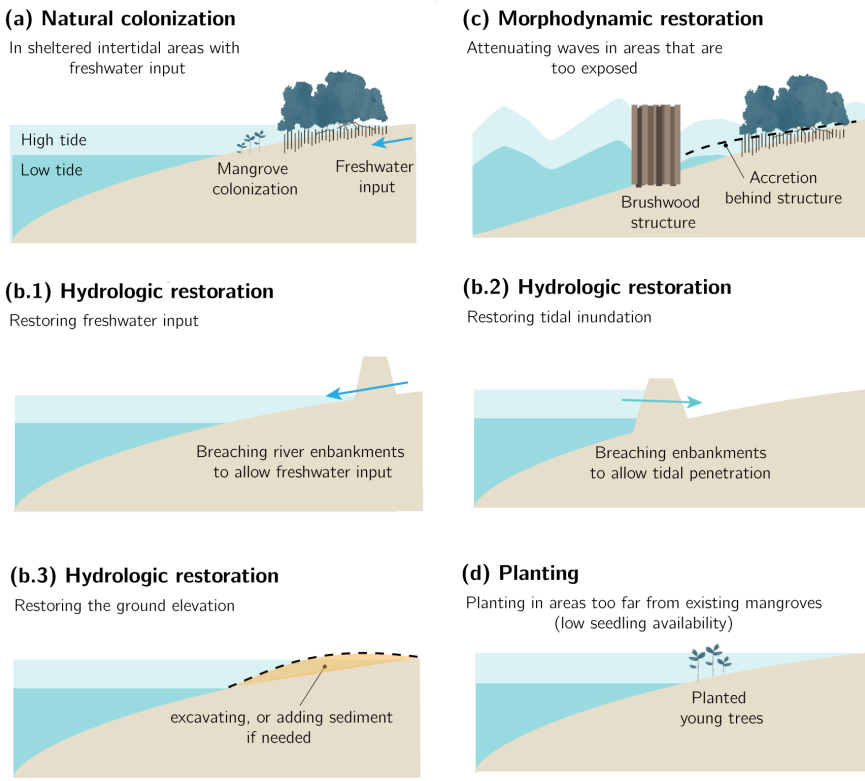

Figure 5.4: Diagram illustrating several mangrove restoration techniques. Mangroves grow at sheltered intertidal areas with freshwater input (a). If human or natural actions degrade a mangrove forest by changing the freshwater input or the local hydroperiod, hydrologic restoration measures can restore the original conditions (b1-b3). When a site becomes too exposed to wave action, leading to erosion, structures can be built to shelter the coastline and enable mangrove recovery (c). If the seedling availability is low at one site, planting can accelerate natural recruitment (d).

tend to grow in bands parallel to the coastline depending on their relative tolerance to physical factors like salinity, soil type, or nutrient content[133]. This relative distribution of the species changes from place to place.

For the case of Bangladesh, clear distribution patterns were not identified in the Sundarbans[41], although the species Sonneratia apetala and Ceriops decandra were generally associated to higher levels of salinity (i.e., to areas with more inundation), while Heritiera fomes (also known as Sunder or Sundri), was linked to lower salinity levels (i.e. to areas with less tidal inundation). The combination of multiple species, at once or in several stages of planting, is also a factor to consider in mangrove restoration designs, since biodiverse forests formed by multiple species are more resistant to pests and have higher chances of long-term survival[124].

Other forms of habitat degradation can require additional steps for mangrove establishment. Human interventions such as sediment disposal, excavation or coastal infrastructure can alter the emergence time needed by mangroves, which should be restored to enable mangrove establishment[84] (see Figure 5.4 b2 and b3). At sites where tributaries bringing freshwater have been blocked, mangrove establishment requires restoring the freshwater input (Figure 5.4 b1).

Some sites require restoring the morphodynamic conditions at the coast. At locations where high wave exposure has led to coastline retreat, bamboo and brushwood structures have been built to attenuate waves and enhance coastline accretion and create new mangrove habitat[169] (Figure 5.4 c). This solution may not be feasible at sites with low sediment availability and high local sea level

rise, since some rates of relative sea level rise may be too high to be compensated by local accretion (see Chapter 4). Lastly, pollution can alter the biochemical conditions of the soil to levels that are not acceptable for mangroves[84].

Mapping all of the relevant variables to diagnose the cause of mangrove absence (land use history, tides, waves, topography, fresh water influx, sediment properties, and soil biochemistry) is not straightforward since it requires high-resolution data that is often scarce. Worthington and Spalding[171] developed a large-scale map indicating potential areas for restoration all over the world by identifying areas of recent mangrove loss, excluding eroded areas and urban areas, and classifying the remaining potential locations based on aspects such as proximity and size of remaining vegetation patches, and local relative sea level rise.

Since the maps developed by Worthington and Spalding[171] display locations of recent loss, they limit the restoration options in countries like Bangladesh, where mangrove degradation has taken place for a long time. For example, historical maps show that in 1775 the Sundarbans forest extended over the southwestern coast of Bangladesh until Lakshmipur[22]. However, the forest area decreased from 7,500 km^2 to 6,000 km^2 between 1873 and 1933[31,19] and its limits have remained approximately the same ever since[61]. Such losses cannot be considered recent, and excluding their potential recovery would leave out a considerable portion of the coastal system.

The classification by Worthington and Spalding[171] also defines eroded areas as unrestorable, while erosion mitigation measures are being investigated in countries like Indonesia, Vietnam, Thailand,

and Surinam[171,139]. Their method could also be improved by accounting for the flood risk of landward areas, to focus the efforts on the most vulnerable locations. We consequently (1) made an inventory of open access data, based on which we (2) developed a screening methodology to map potential mangrove areas for the case-study of Bangladesh.

5.3. Mangrove mapping method

5.3.1. Description of the study area

Bangladesh is located at the north of the Bay of Bengal, bounded by India at the west, north, and east, and by Myanmar at the southeast. The country lies on the Gangetic delta, formed by the deposition of sediment transported by the Ganges, Brahmaputra, and Meghna rivers[8]. The eastern part of the coastal system is covered by the Bangladeshi side of the Sundarbans, the largest continuous mangrove forest in the world (Figure 5.5). The central part of the coastal system most consist of low-lying polder area, whereas the western coastal region consists of relatively narrower polders developed over steeper ground, e.g., as it can be seen in Figure 2.3. of Dasgupta[35].

5.3.2. Open access data bases

Figure 5.6 summarizes the open access sources identified in the present study, including digital elevation data[77], tidal data[23], relative sea level rise data[63], and GIS data providing the location of rivers, tidal flats[104], and mangroves. Both wave and bathymetric data were scarce, and we could not identify data sources covering

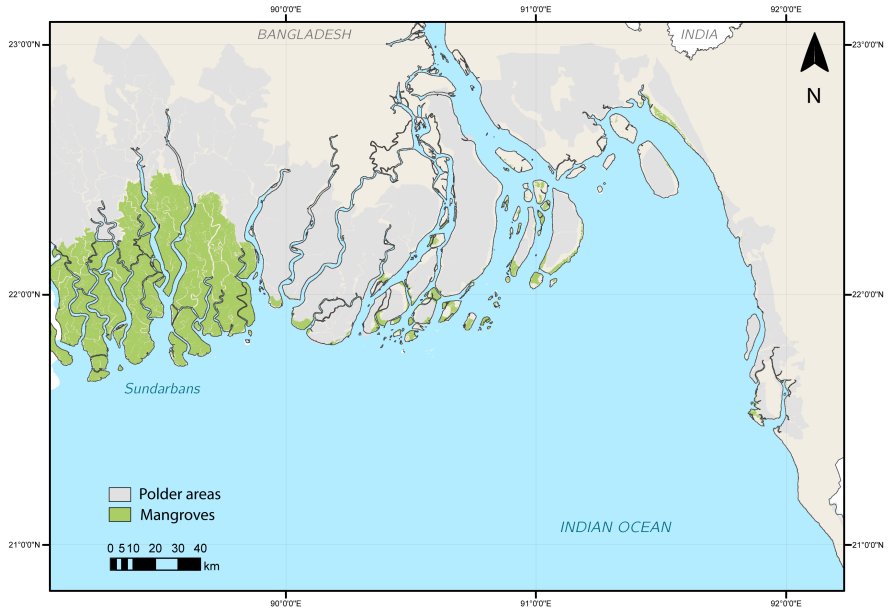

Figure 5.5: Coastal system of Bangladesh, showing mangrove areas (green) and embanked polder areas (grey). The large green area at the west is the Bangladeshi part of the Sundarbans, the largest continuous mangrove forest in the world. The Sundarbans is shared by Bangladesh and India, and the Bangladeshi side constitutes approximately 60% of the total area of the forest.

the full coastal zone.

Dataset Type	Description	Source
Digital elevation model	CoastalDEM ® is a digital elevation model at 90 × 90 m resolution, with a maximum vertical accuracy of − 0.29 m.	Kulp and Strauss [77]
Coastline change	The Aqua-monitor tool provides the rate of coastline change, and sediment composition (sandy or not sandy), since 2016, in transects every 15 m along the coastline.	Luijendijk [86]
Intertidal areas	Global Intertidal provides maps with tidal flat areas until 2016	Murray [103]
Mangrove cover	Global Forest Watch provides the areas of mangrove coverage from 2001 to 2018 (https://www.globalforestwatch.org, accessed on the 1 May 2020)	Global Forest Watch
Rivers	Maps of rivers of Bangladesh (https://data.humdata.org/, accessed on the 1 May 2020).	LGED
Tidal range	Tidal range measurements	Bricheno [23]
Country boundaries and regions	Boundaries of the country and its regions (https://gadm.org, accessed on the 1 May of 2020)	GADM
Sea level rise	Global predictions of relative sea level rise	IPCC [149]

Figure 5.6: Open access data sources identified in the present study.

5.3.3. Screening methodology

Based on the existing data sources, we developed a method to identify potential mangrove sites along the coastline. The criteria for site selection are explained below, and schematized in Figure 5.7:

1. Suitability of a site as potential habitat: we considered sites within 10 km of existing mangroves as potentially suitable for colonization. This limit is based on dispersal distances observed by Clarke[29] for Avicennia marina seedlings. In practice, the dispersal distances will vary between mangrove species, and will depend on the local hydrodynamic processes. However, this value provides a preliminary indication of the areas that could recruit naturally. The existing mangrove sites were obtained from the maps by the Global Forest Watch (Figure 5.6).

2. Method needed to implement vegetation: the techniques needed to vegetate a site were based on the rates of coastline change from the Aqua-monitor tool[86]. We assumed that natural coloniza-

tion would happen at locations with expanding coastlines near existing mangroves, and if seedling availability was low, or natural processes were too slow compared to coastal protection targets, they could be complemented by planting efforts. At sites with retreating coastlines, erosion mitigation measures such as bamboo structures or nourishments would be needed.

3. Prioritization criterion based on vulnerability: we evaluated the level of priority based on the flooding risk of landward areas using the ground elevation measurements from CoastalDEM®[77], and 3 scenarios of relative sea level rise (RSLR) from IPCC[63]; +0.3 m (expected value in 2050), +1 m (worst case scenario in 2050) and +2 m (worst case scenario in 2100). Since polders comprise inhabited areas and valuable assets, their protection was prioritized compared to non-polder areas. Moreover, polders are blocked from any sediment input by the tide, which means that, unlike unembanked areas, they have no mechanisms to accrete and keep up with rising sea levels. Polders that would be below MSL in the RSLR scenario of +1 m in 2050 were given the highest flooding risk, and we prioritized vegetated foreshores seawards of them.

5.4. Potential mangrove sites in Bangladesh

The sites identified as potentially suitable for foreshore afforestation are shown in Figure 5.8. Our method suggests that approximately 600 km of coastal stretches seawards from embankments are located within 10 km of existing mangrove patches. Out of those 600 km, we prioritized 6 sites based on their flood risk, which constitute approximately 140 km of coastline. Their location, polder, and the techniques recommended to implement mangrove vegetation are

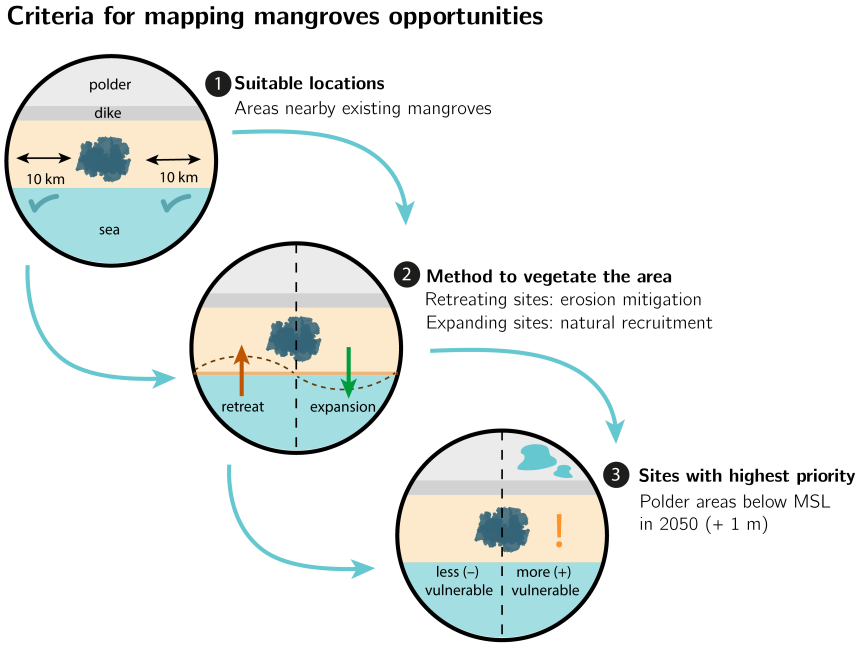

Figure 5.7: Criteria for mapping mangrove opportunities. (1) Coastal sites located less than 10 km away from existing mangroves are considered as potentially suitable for mangrove recruitment. (2) The technique needed to vegetate a site is chosen based on the coastline behavior. Expanding coastlines could be colonized naturally, and planting schemes could be conducted if more detailed studies show the need to do so (e.g., if seedling availability is too low, or if the natural establishment is too slow for coastal protection purposes). Retreating coastlines would require erosion mitigation measures. (3) Vegetating foreshores fronting polder areas with low ground elevations is prioritized.

indicated in Figure 5.9. The specific sites where erosion mitigation measures are needed are shown in Figure 5.10, Figure 5.11, and Figure 5.12.

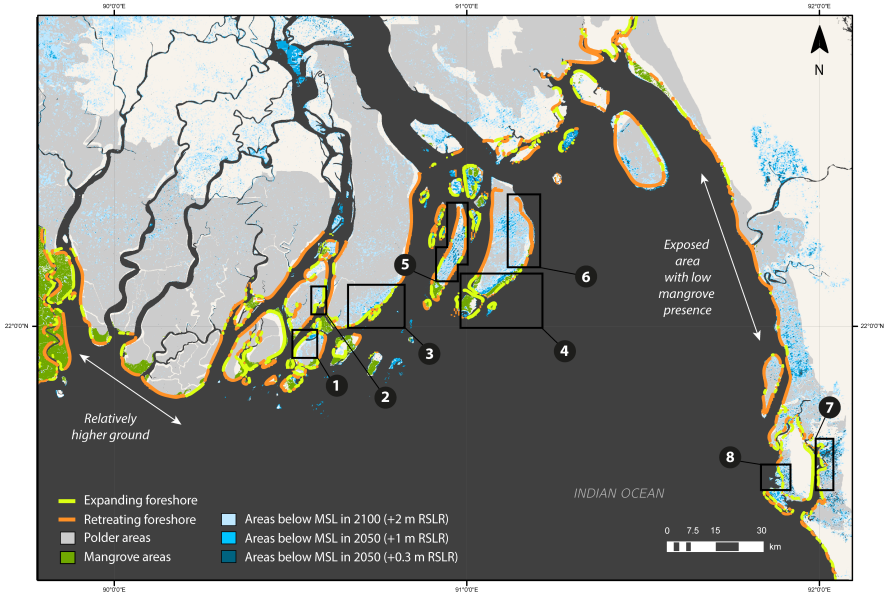

Figure 5.8: Map showing mangrove development opportunities in Bangladesh.

ID	Location	Polder	Vegetation Implementation Technique
1	Galachipa	P55/3	Natural recruitment/planting
2	Galachipa	P55/4	Natural recruitment/planting
3	Bhola	P56/57	Natural recruitment/planting
4	Hatiya South	P73/2	Natural recruitment/planting
5	Manpura	P58/1–3	Erosion mitigation/Natural recruitment/Planting
6	Hatiya North	P73/1	Erosion mitigation/Natural recruitment/Planting
7	Khangona	P66/3	Natural recruitment/planting
8	Boro Moheshkhali	P69	Natural recruitment/planting

Figure 5.9: Selected sites for mangrove-vegetated foreshores, including the polder number, and general technique recommended to vegetate each area.

The Sundarbans forest (western limit of Figure 5.8) was not included in the analysis since mangroves have natural mechanisms

to keep up with rising sea levels, and we assumed that natural recruitment processes will continue there without any need for human interference. The polder area east from the Sundarbans, along the coast of Barguna, had low vulnerability to relative sea level rise, so it was given low priority and excluded from the site selection.

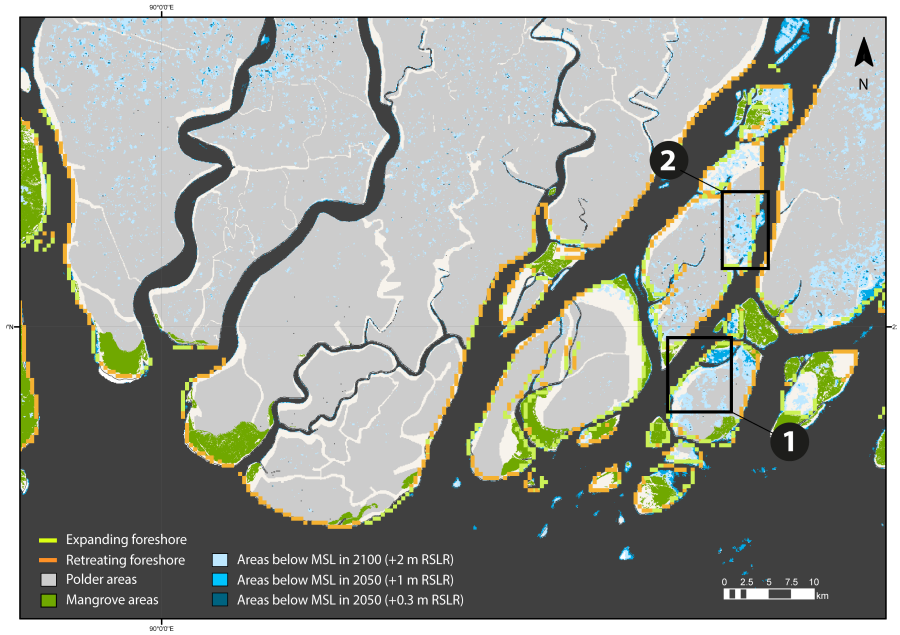

Figure 5.10: Potential sites for vegetated foreshores (west).

Locations 1-4 correspond with expanding coastlines fronting polder areas of low ground elevation. These four sites are placed near existing mangrove patches, so the newly accreted land could be colonized naturally by mangroves. Erosion mitigation measures may be needed at some specific stretches of sites 1 to 4 (see Figure 5.10 and Figure 5.11). Locations 5 and 6 also front areas vulnerable to flooding, but they require erosion mitigation measures along most of the coastline.

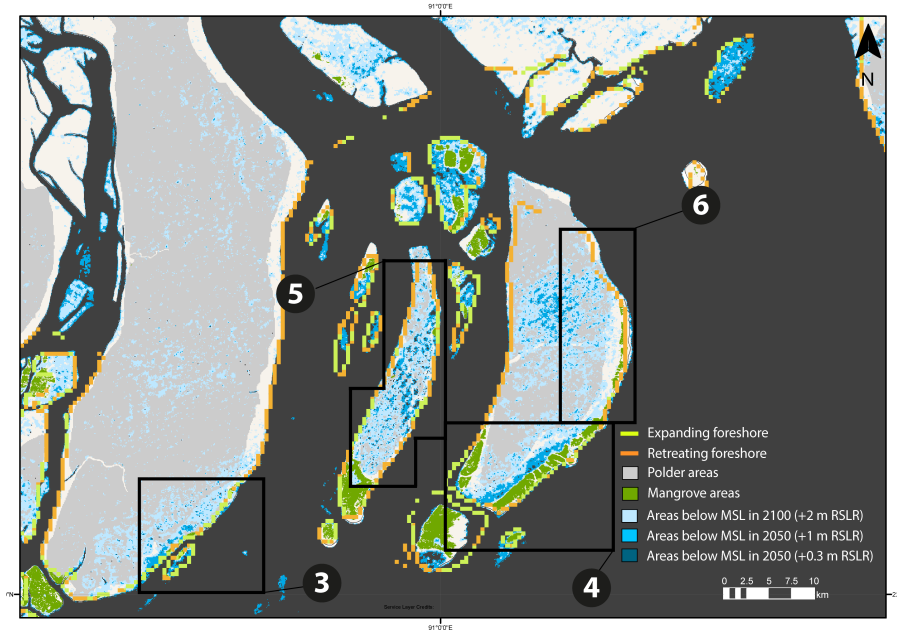

Figure 5.11: Potential sites for vegetated foreshores (center).

The coast at the eastern side of the country is mostly eroding and mangrove vegetation is almost completely absent. Sites 7-8 are relatively more sheltered from waves due to the presence of Maheshkhali island (Figure 5.12), and they correspond to expanding coastlines seaward from polders with high vulnerability to rising sea levels. Mangroves are already present close to these sites, so both locations have high potential for natural recruitment or planting schemes.

Implementing mangrove foreshores at the locations illustrated in Figures 5.8-5.12 could reduce the loads on embankments, decreasing their upgrading costs. In order to explore the impact of a vegetated foreshore on the design of a dike, here we estimate the required dike height with and without a mangrove belt seaward of the embankment. The crest height of a dike is designed so that the

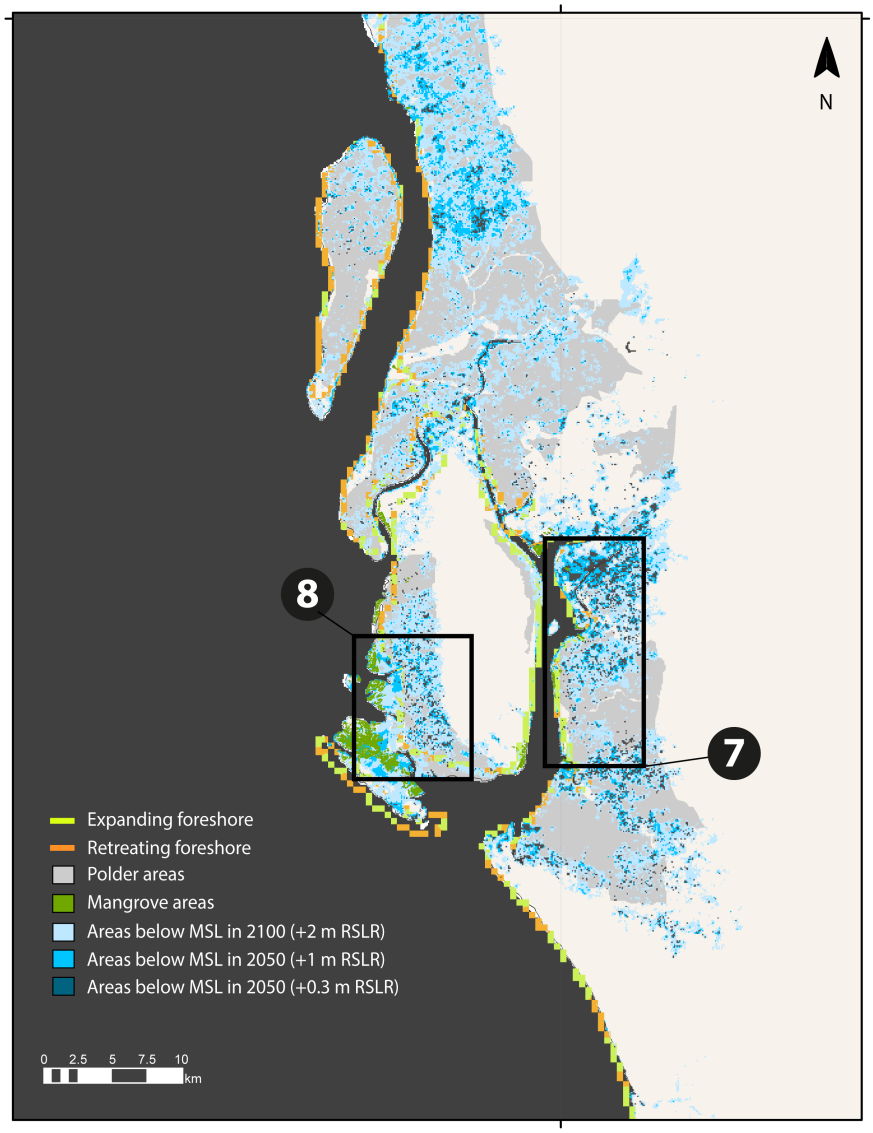

Figure 5.12: Potential sites for vegetated foreshores (east).

maximum discharge over the structure does not exceed a maximum threshold during design conditions. Figure 5.13 shows the needed embankment height to obtain a maximum overtopping discharge of 5 l/m/s, where the discharge is calculated with the equation of Van der Meer[159]:

$$q = \sqrt{gH_{m0}^3}\frac{0.026}{tan(\alpha)}\gamma_b\epsilon_{m-1.0}e^{-\left(2.5\frac{H_{crest}-H}{\epsilon_{m-1.0}H_{m0}\gamma_b\gamma_f\gamma_\beta\gamma_\nu}\right)^{1.3}} \tag{5.1}$$

where q is the overtopping discharge per meter, g is the gravitational acceleration, H_{m0} is the spectral wave height, α is the angle of the outer slope, $\xi_{m-1.0}$ is the breaker parameter, γ_b is the influence factor for a berm, γ_f is the influence factor for roughness elements on the slope, γ_β is the influence factor for oblique wave attack, γ_ν is the influence factor for vertical wall, H_{crest} is the crest level, and H is water level.

For coastal embankments, slopes of 1:8, armour layers (corresponding with $\gamma_f = 0.55$), and berms (with γ_b for a 5 m wide berm placed at the still water level) are often implemented. We assume perpendicular wave incidence (so $\gamma_\beta = 1$), and no vertical walls ($\gamma_\nu = 1$). The dark blue line is calculated with a design wave height of $H_{m0} = 3$ m, and a surge height of $H = 5$ m, which result in a minimum crest height of $H_{crest} = 6.1$ m.

The lighter blue line is obtained by reducing the wave height to simulate the effect of mangroves while keeping the surge height constant. Wave attenuation rates range from 5% to 100%[93,13] over 100 m of mangrove forest (see McIvor[94], or Horstman[56] for a full review). Assuming 8% reduction over 100 m, and that the wave height reduces linearly with the distance into the forest over the first 500 m (see Figure 4.1. in Barbier[14]), a mangrove belt of 500

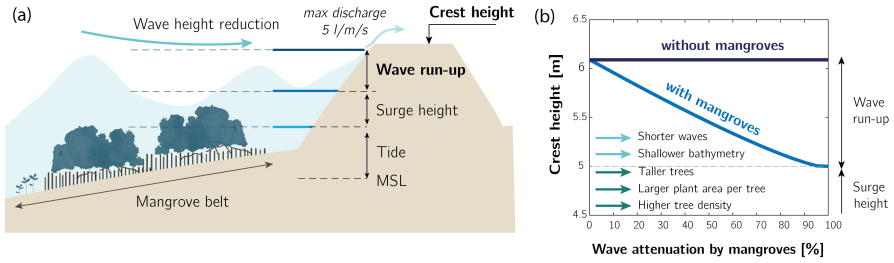

Figure 5.13: (a) Design water levels of an embankment. (b) Required embankment height to have a maximum discharge of 5 l/m/s, with and without wave attenuation by a mangrove belt.

m could cause a 40% reduction of the wave height, decreasing the minimum necessary height of the embankments from 6.1 m to 5.5 m. This crest height reduction would directly translate into a decrease of the building costs.

5.5. Discussion

By reducing the wave loads on the structure, mangroves would not only reduce the necessary crest height of a structure but they also could decrease the costs for slope and bank protection, or even completely eliminate the need for revetments. However, implementing vegetated foreshores requires addressing several considerations.

Firstly, we identified areas with potential for mangrove establishment, but the suitability of potential sites should be investigated in more detail. Our model did not include relevant factors such as the local hydrology, soil properties or wave action at the coast. These factors should be assessed locally and compared to the mangrove habitat requirements[12,24]. Remote sensing techniques may constitute a valuable source for these parameters. The combina-

tion of datasets of the physical parameters with maps indicating the presence of mangroves and deep learning methods could provide mode accurate habitat identification techniques. Expanding the mapping methodology with additional restrictions may limit the presence of mangroves at some of the locations highlighted in Figure 5.13, but it could also identify new mangroves opportunities. For example, our approach focused on mangrove opportunities along open coastal areas, but there may be additional potential sites at more upstream locations. Identifying those would require tidal and DEM data with higher resolution and accuracy than those listed in Figure 5.6.

Secondly, bed level changes seawards from the embankments could change the wave run-up height, and the required crest height with respect to the estimates of Figure 5.13. Process-based models[17] could estimate how the coastline is likely to change over time under different scenarios, and how the vegetation could develop. This approach would require more detailed morphodynamic data, and information about the local mangrove species and soil properties. The estimated coastline morphology and vegetation properties could be implemented in probabilistic design models such as Vuik[153,154], in order to assess impact of mangroves on other structure failure mechanisms, such as erosion of the dike cover.

Thirdly, although mangroves can reduce the loads on coastal infrastructure, afforestation involves an economical investment, and mangroves occupy areas that could have other productive applications. A complete cost-benefit analysis would require pondering the construction and maintenance costs of raising the embankments versus developing and maintaining a mangrove belt, and comparing

the benefit derived from productive land uses, such as farming or aquaculture, with the mangrove ecosystem services. This type of analysis could also indicate which mangrove belt width could be most cost-effective. Moreover, it is also important to assess how other ecosystem services could affect the protective role of the vegetation, for instance for activities like wood harvesting[78].

Mangroves can also be physically degraded during extreme events, for example due to breakage or uprooting by waves or currents. The possibility of vegetation failure should thus be considered in dike designs, due to both mechanical and biological causes. Low diversity has been associated to large-scale death event due to pests in single species stands of mangroves[167,26,27], but this aspect has received relatively less attention in planting schemes. Spatial statistical techniques can offer powerful tools to evaluate risk associated to low biodiversity[173], and to create more resilient afforestation plans.

Implementing mangroves in coastal protection plans would also require more accurate ways to estimate the flood risk. Our method indirectly evaluated flood risk by prioritizing polder areas (enclosing valuable assets) and low elevation polders (with potentially larger flooding depths), but it did not estimate the value of the assets nor the flood characteristics in case of dike failure. Hotspot detection tools[172] would be particularly valuable for policy makers, as they would provide quantitative ways to identify the most vulnerable areas. More accurate flooding models, including the potential effect of surges, would also be necessary for precise predictions of the flooding depth and speed, e.g. as done in Jonkman[69]. The combination of such tools would provide more accurate assessments of the risk reduction by a mangrove belt.

Once an optimum mangrove width is selected, it will take time for mangroves to grow. The growth period will depend on the local species and the afforestation technique, and the embankments should provide enough safety against wave attack while the mangrove belt is developing. Due to the inherent uncertainties in the evolution of the bed level and the vegetation, the foreshore should be monitored regularly by measuring (1) bathymetries, and (2) vegetation properties such as number of seedlings, and their geometry.

The monitoring data would enable readjusting the restoration strategy if necessary, or protecting the profile in case of erosion by building bamboo structures or nourishing sediment. If the restoration targets are not satisfied after the expected growth time, the embankment could then be reinforced to ensure the safety of landward areas.

The natural adaptability of mangroves to rising sea levels[151,126] in combination with grey infrastructure and robust monitoring systems, can provide a resilient tool to protect coastal areas. Our methodology offers a systematic approach to integrate vegetated foreshores and embankments in coastal protection schemes, which compensates data scarcity by using open access data sources. This mapping method could thus be applied to identify potential mangrove sites in data-scarce areas, constituting a useful tool to integrate nature-based flood defenses in coastal protection and adaptation plans.

6. Synthesis

This dissertation investigates how to aid mangrove restoration at eroding coastlines using bamboo structures. The first chapters explore how structures affect currents (Chapter 2), waves (Chapter 3) and sediment transport (Chapter 4). A methodology was also developed to find locations where mangrove belts may be developed seawards from dikes (Chapter 5).

This chapter discusses the outcome of each chapter by reiterating the main research objective, and providing its main scientific conclusions and their implications. Recommendations for future research are also provided for each chapter. The section concludes with a general reflection on the challenges of conserving and restoring mangrove coastlines all over the world.

6.1. Effect of bamboo structures on currents

Previous restoration efforts were limited by the lack of models to predict the effect of bamboo structures on currents. The aim of Chapter 2 is thus to develop a predictive method to estimate the resistance exerted by bamboo structures on a current.

Laboratory experiments were conducted to explore the processes driving the resistance by arrays of cylinders (representing the bamboo poles of a structure), and the experimental results guided the derivation of a model to predict their resistance. The flume experiments confirmed that the forces acting on regular cylinder arrangements vary with the spacing between poles. Narrower lateral spacings (in the direction perpendicular to a current) cause flow acceleration, which increases the forces acting on the poles (an effect denoted as blockage). Inversely, small distances between cylinders in the flow direction reduce the velocity acting on downstream elements, and the forces acting on them (an effect described as sheltering).

The resistance (drag) forces exerted on bamboo poles in a current are thus predicted using a quadratic drag formulation, in which the velocity upstream from a structure is multiplied by a blockage factor (f_b) and a sheltering factor (f_s) (Figure 6.1). The blockage factor is determined from mass conservation over a cross-section of the structure, as suggested by Etminan *et al.*[43,44]. The sheltering coefficient depends on the turbulence intensity[38], which is calculated from a balance between turbulence production and dissipation, following the approach of Nepf[106].

This approach is limited by several simplificative assumptions during its derivation, which are valid for the present case but may not hold in other applications. The model assumes that the forces acting on the poles are dominated by the form drag, caused by the turbulent wakes behind the poles. Vortex shedding can occur within a structure at high Reynolds numbers and for lateral spacing between cylinders larger than 1.3 times the diameter. However,

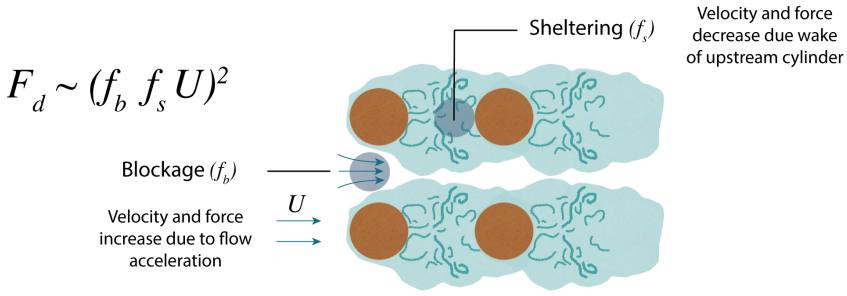

Figure 6.1: Parameterization of the drag forces acting on a cylinder in a current. The velocity upstream of the cylinders is multiplied by a blockage factor (f_b), which accounts for flow acceleration between cylinders, and by a sheltering factor (f_s), which accounts for the velocity reduction on downstream cylinders due to wake development.

smaller spacings may inhibit vortex shedding, and very dense cylinder arrangements may thus fall outside the range of applicability of this model. The method also assumes small differences in water level just upstream and in between the cylinders, and relies on the value of empirical parameters. Several potential adaptations to expand the model's applicability are presented in Chapter 2.

For the bamboo structures, this method constitutes a very flexible tool to predict the structure resistance. The inclusion of the sheltering and blockage factor enables testing many different regular geometries without having to derive empirical coefficients for each configuration, and model predictions also showed a reasonable agreement with measurements for random arrays of cylinders. As a next step, this method can be integrated into a larger-scale 2DH model, and applied to explore how different designs affect local currents and sediment transport.

6.2. Effect of bamboo structures on waves

The objective of Chapter 3 is twofold: (1) developing methods to predict wave reflection and dissipation by bamboo structures, and (2) assessing which designs could replace brushwood structures in Demak. The discussion on each objective is presented below.

6.2.1. Predictive models for wave reflection and dissipation by bamboo structures

Chapter 3 presents a model to predict the effect of bamboo structures on waves, based on measurements from wave flume experiments. Wave transmission through the structures is calculated by schematizing them as parallel rows of cylinders, and subtracting the wave energy dissipation and reflection row by row. Wave dissipation is computed as the work done by the drag forces.

In oscillatory wave flows, the drag forces are also calculated by multiplying the velocity upstream from the structure by a blockage (f_b) and a sheltering factor (f_s), but a factor dependent on the Keulegan-Carpenter number (f_{KC}) is also included to represent the transition between inertia and drag dominated conditions (Figure 6.2). Wave reflection is calculated with an empirical expression that depends on the fluid area occupied by cylinders.

The model provides good results for the conditions of the flume experiments but depends on empirical parameters derived from a relatively narrow set of experimental conditions. The wave experiments of Chapter 3 only cover KC values between $KC = 10 - 22$, where the drag coefficient had not yet approached the limit of steady flow values. This implies that the full behaviour of f_{KC}

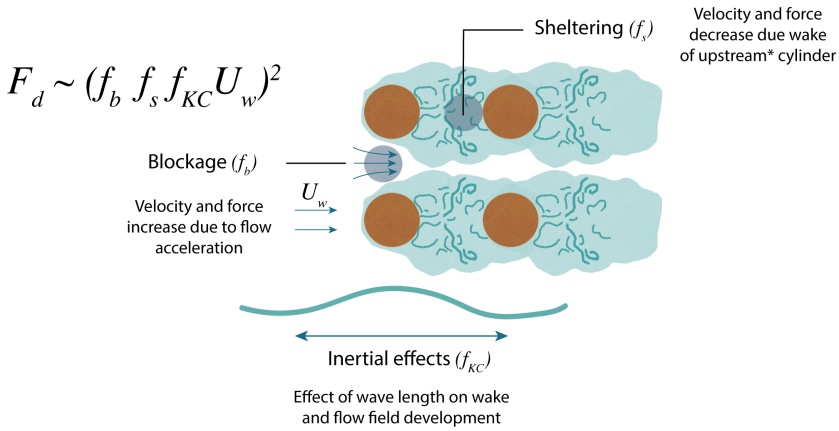

Figure 6.2: Parameterization of the drag forces acting on a cylinder in a wave oscillatory flow. The velocity upstream from the cylinders is multiplied by a blockage factor (f_b), which accounts for flow acceleration between cylinders, and by a sheltering factor (f_s), which accounts for the velocity reduction on downstream cylinders due to wake development. A factor dependent on the wave excursion (f_{KC}) is included to represent the effect of wave length on the flow field. The asterisk is meant to indicate that in waves the flow direction reverses every half cycle.

cannot be described from the measurements. For oscillatory wave flows the sheltering coefficient is empirically fitted to experimental data, instead of determined with a turbulence model. The wave reflection coefficient is assumed to be uniquely dependent on the cross-section of the structures, whereas in reality it will also depend on wave properties such as the wave period. In order to make the method as general as possible, it is thus recommended to expand the experimental range of wave conditions and structural geometries to find more complete expressions for f_s and f_{KC}, to expand the turbulent model of Chapter 2 for wave flows, and to develop the expression for wave reflection.

Despite these shortcomings, the present method constitutes a physics-based framework that accounts for the different processes influencing flow velocity changes inside groups of cylinders. This is a significant step compared to the traditional approach of gathering all effects into a single bulk drag coefficient. The separate predictions for the processes of sheltering and blockage are especially useful when comparing different structure configurations to optimize designs. An example of model application is thus provided in the next section.

6.2.2. Cost-optimum structure designs for wave attenuation

As hypothesized based on the existing literature, wave flume experiments show that bamboo pole arrangements with small lateral spacings (perpendicularly to waves) and long separation in the wave direction maximize forces and wave dissipation rates per element (Figure 6.3 a-b). Horizontal beams also cause more wave attenua-

tion compared to vertical poles (Figure 6.3 c), as they produce form drag forces both vertically and in the direction of wave propagation. The additional dissipation by horizontal beams becomes relevant for deep water waves, whereas in shallow water conditions horizontal and vertical poles provide comparable forces and dissipation. Structures formed by horizontal bamboo beams could therefore be an alternative to brushwood structures in deep and intermediate waters, whereas both horizontal beams and vertical bamboo poles could be implemented in shallow water (Figure 6.4 a-c).

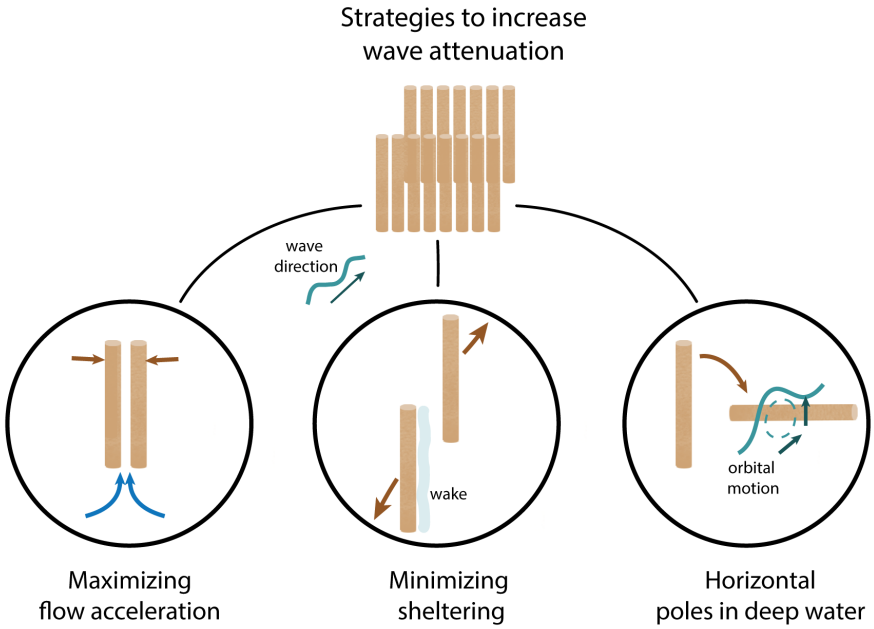

Figure 6.3: Strategies to increase wave attenuation of a group of bamboo poles: (a) decreasing the lateral spacing (perpendicular to the wave direction) to maximize flow acceleration, (b) increasing the spacing in the wave direction to minimize sheltering on downstream elements, and (c) placing the bamboo poles horizontally in intermediate and deep water to induce wave energy dissipation by a vertical and a horizontal drag force component.

The cost-effectiveness of a structure does not only depend on finding optimum cylinder arrangement, but also on material, construction and maintenance costs. These aspects are examined here for the case of Demak, using unit costs provided by Witteveen and Bos (Figure 6.4 e). These values were used to calculate the initial investment costs of the structures, and their maintenance over time. Bamboo poles are wrapped in polyethylene sheets to expand their durability from two to five years, whereas the brushwood filling has to be replaced twice a year at exposed locations, and once a year at more sheltered sites.

The cumulative costs (initial investment plus yearly maintenance) are calculated for structures with a transmission rate of 50% for waves of $H = 0.25$ m and $T = 3.5$ s, assuming a water depth of 0.5 m with respect to mean sea level (MSL). The structure dimensions are calculated using the model presented in Chapter 3, for three types of configurations: a structure formed by brushwood (Figure 6.4 c), a structure formed by vertical bamboo poles only (Figure 6.4 a), and a structure formed by horizontal rows of bamboo (Figure 6.4 b). For the structures formed by brushwood and horizontal beams, additional vertical poles are included for structure stability (2 per row and per m of structure in the alongshore direction). The resulting structure properties are summarized in Figure 6.4 (d). Although all structures provide 50% transmission for the chosen wave condition, the wave reflection rates are not identical and they are equal to 14% (for vertical cylinders only), 10% (for horizontal beams), and 22% (for brushwood), respectively.

Structures formed by only vertical bamboo poles are the most expensive option (as shown in the first year of Figure 6.4 f). Since

(a) Vertical poles (b) Horizontal poles (c) Brushwood

(d) Structure types

Structure type	D [m]	sy/D [-]	sx/D [-]	Nr [-]	N [el/m]
Vertical poles	0,15	1,5	10,0	7,0	28,0
Horizontal poles	0,10	1,5	10,0	5,0	35,0
Brushwood	0,02	1,5	1,5	23,0	759,0

(e) Unit costs

Material type	Unit	Material cost (euros)	Installation cost (euros)
Vertical bamboo	pole	7	4
Horizontal bamboo	pole	5	4
Brushwood	m3	22	9

(f) Cummulative costs maintaining brushwood once a year

Structure configuration	Cummulative costs (euros/m)				
	Year 1	Year 2	Year 3	Year 4	Year 5
Vertical bamboo	308	308	308	308	308
Horizontal bamboo + vert. bamboo	232	232	232	232	232
Brushwood + vert. bamboo (1 m/y)	95	117	139	162	186
Brushwood + vert. bamboo (2 m/y)	95	139	184	230	276

Figure 6.4: Cost comparison of different structure designs: (a) structures formed by vertical poles, (b) structures built with horizontal beams, and (c) brushwood structure. Table (d) shows the structure geometry, where D is the pole or brushwood diameter, s_y is the spacing between elements in the alongshore direction, s_x is the spacing between elements in the wave direction, N_r is the number of rows, and N the number of elements per m of structure. The unit costs of structure materials and construction are shown in (e). The total costs per meter in the alongshore direction are shown in (f) for vertical, horizontal, and brushwood structures, with brushwood maintenance once a year (1 m/y), and twice a year (2 m/y). These costs are only indicative as unit costs may change for different providers, and they may also change over time.

every pole must be driven into the soil, vertical poles have to be at least 2 m longer than if they were placed horizontally, increasing their material as well as labor costs. Structures formed by horizontal beams are the second cheapest alternative, as they minimize the required material and their investment costs are relatively lower than for structures uniquely formed by vertical poles. Brushwood structures are the cheapest option, as they have less vertical poles than the other two alternatives, and due to the low cost of the brushwood filling.

When long-term maintenance costs are factored in (see years 2-5 of Figure 6.4 f), where the costs are expressed in euros of 2021 correcting for steady 2% inflation over the following years), brushwood structures become increasingly expensive over time. With one maintenance operation per year (third row in Figure 6.4, f), brushwood structures still remain the most economical option for all years despite their repair costs. With two maintenance operations per year (fourth row in Figure 6.4, f), brushwood structures are the cheapest alternative for lifetimes smaller than three years. After 4 years, horizontal beams and brushwood structures become comparable options. Horizontal structures are more economical for a lifetime of 5 years. The choice of structure configuration is thus largely dependent on the desired structure lifetime and on the maintenance frequency.

The cost estimates of Figure 6.4 are presented to discuss how additional factors besides cylinder placement can affect structure optimization. However, a full cost-comparison requires ensuring that the designs remain stable during design conditions - an aspect that was not considered in the designs of Figure 6.4. The timing

of structure failure is also a limiting factor since maintenance operations are limited by the weather. A structure failing during a storm in the beginning or in the middle of a NW monsoon may not be accessible for repair until early March, exposing the coastline to larger waves during the storm season. Modelling results of Chapter 4 indicate that if the density of the brushwood filling falls below $N_v = 50$ elements/m^2, a structure has almost no effect on the coastline position. Monitoring of the pilot study also showed that significant damage in the brushwood filling led to a negligible effect on the coastline (compared to control locations).

The brushwood filling was the most vulnerable component of the structures in the pilot study, but structures formed vertical poles and horizontal beams can also fail during a storm, especially since the spacing between elements is kept small in Figure 6.4 to maximize the drag forces and the wave energy dissipation per pole. The stability of the brushwood filling and the contribution of the local geotechnical conditions to structure integrity are outside the scope of this work but they should be integrated in structure designs. Since the geotechnical properties, the wave climate, the material availability and prices will differ between sites, the choice of the optimal structure should be based on site-specific cost-assessments.

Lastly, the plans for structure design should also include environmental assessments and their clean-up costs (Figure 6.5). Existing designs disregarded the environmental effect of structure degradation under the assumption that bamboo and brushwood structures are biodegradable. However, polyethylene sheets will disintegrate over time and pollute the coast, and debris from deteriorated bamboo and brushwood structures was found to damage

fringe mangroves in Vietnam[117]. The breaking down of bamboo poles can also be a hazard for swimmers and fishermen at coastal areas - broken poles can become sharp razors that cannot be seen through the murky waters. Assessing environmental impacts and quantifying the structure dissembling costs are thus recommended for future designs[117].

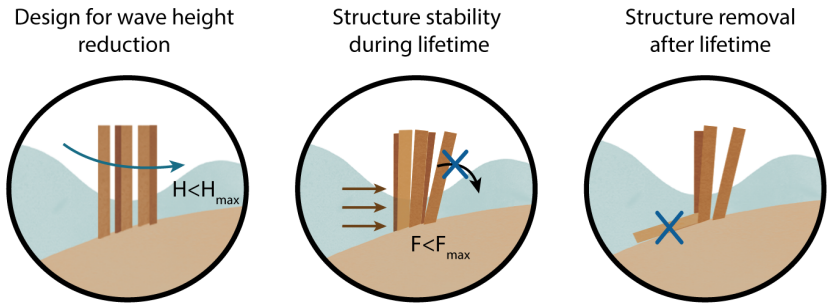

Figure 6.5: Aspects to consider in hydrodynamic structure design: (1) finding the structure configuration that provides the amount of wave reduction needed to mitigate erosion and cause sediment accretion (according to a morphodynamic model), (2) while ensuring the designs are stable under design loads and (3) structure removal after its lifetime.

6.3. Effect of bamboo structures on morphodynamics

Chapter 4 aims to investigate the effect of brushwood structures on sediment transport and on the coastline position for the case of Demak. Field data was thus collected to validate XMgrove, a morphodynamic model developed by Reniers et al.[121]. Once validated the model was applied to evaluate scenarios with different structure configurations and different boundary conditions. The discussion

on the model results contain four parts: (1) on the lessons learnt for Demak, (2) on the limitations of the model results based on the knowledge of the local ecology, (3) on how to minimize erosion seawards from the structures, and lastly (4) on how optimum designs could change at other coastal systems.

6.3.1. Optimising restoration with structures in Demak

Bamboo and brushwood structures were developed to enhance sediment accumulation at sites where human interventions have destabilized the balance between erosion and deposition, leading to coastline retreat. This imbalance can be compensated by a local redistribution of sediment by the structures. However, local sources can become depleted after some time, and compensating rising water levels requires a continuous supply of sediment. Modelling scenarios suggest that the structure monitored in Chapter 4 may have failed to stop coastline retreat because the subsidence rates in Demak are too high to be counteracted by the local sediment sources.

Assessing whether structures can be implemented to cause accretion and create new mangrove habitat, in Demak and other mangrove coastlines, thus requires: (1) knowledge of the history of the area and the causes of mangrove degradation, (2) quantifying the local morphodynamic conditions (e.g.: waves, water levels, currents, sediment properties, local bathymetry), (3) quantifying the local rates of relative sea level rise (RSLR), and (4) estimating the local sediment budget. Some physical properties, such as the wave climate or the sediment input by rivers, may vary on a seasonal or yearly basis, and these variations should be investigated by preliminary assessments. The collected data can then be used in a

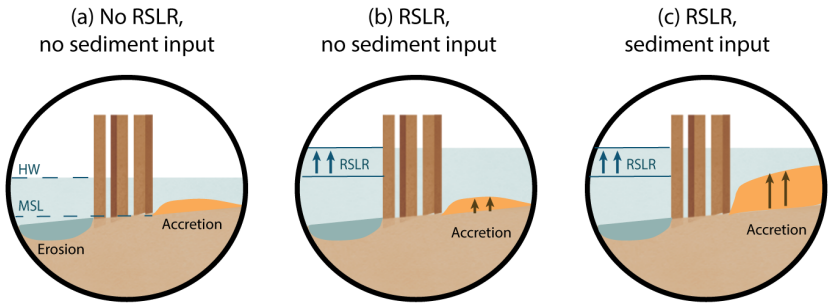

Figure 6.6: Effect of bamboo structures on bed level for different rates of relative sea level rise (RSLR) and sediment supply. (a) Without RSLR and without sediment supply, structures cause a redistribution of sediment which can produce mudflat expansion landwards from the structure. (b) With RSLR and without subsidence, local sediment sources will be depleted at some point and the coastline will retreat. (c) With RSLR and sediment supply, structures may be able to counteract RSLR depending on the relative magnitude of the sediment input versus the rates of change of the water levels.

morphodynamic model, in order to assess the feasibility of using structures to stop coastline retreat. At sites where retreat cannot be compensated by sedimentation, sediment nourishing may be considered as an alternative measure to restore the mangrove habitat.

6.3.2. Additional bio-physical requirements for mangrove colonization

Although the modelling approach followed with XMgrove can guide efforts to cause coastline progradation and create new mangrove habitat, mangroves have additional requirements to establish and grow over time (see Section 6.4). Assessing whether the vegetation will colonize the newly accreted land requires modelling the

windows of opportunity of mangrove establishment. The numerical design tool XMgrove includes a dynamic vegetation model based on criteria for establishment and growth rates provided by Balke et al.[12] for Avicennia marina seedlings, which is the pioneer species in Demak. In the future, the model will be expanded to include the growth and failure of mature trees over time (Figure 6.7). Moreover, additional species could follow after the establishment of Avicennia seedlings. Including several types of mangroves would thus enable reproducing the dynamics of a natural mangrove forest.

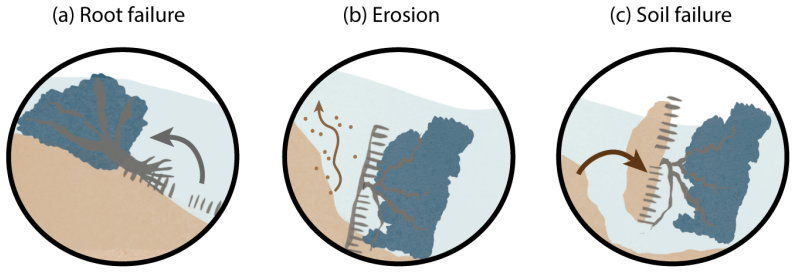

Figure 6.7: Potential failure mechanisms of mature mangrove trees. (a) Root failure, (b) erosion of the seabed, and (c) soil failure.

Even though Chapter 4 did not explore the processes of mangrove establishment, growth and mortality, ecologic studies suggest that subsidence is the main limiting factor for mangrove rehabilitation in Demak. Local soil conditions and water quality were measured and found suitable for mangroves[157]. Mangrove seeds are also available across the coastal system, and remote sensing studies have shown that mangroves occasionally have established in Demak during periods of large sediment deposition and low wave action[18]. Mechanical pulling experiments of seedlings showed that the forces needed to uproot them cannot not be produced by local

waves, except for seedlings less than one month old[18]. However, most seedlings established during the pilot project were not able to survive in the long run, probably due to the continuous coastline retreat caused by subsidence and erosion. This is further supported by the spatial distribution of mangrove mortality; mangrove loss was found highest towards the south, at locations that are furthest away from the Wulan river and closest to the city of Semarang[18], where the subsidence rates are largest and the sediment input lowest.

Cheniers are able to generate some windows of opportunity for mangroves. These intertidal sand lenses promote fine sediment deposition on their land side, and shelter small seedlings from wave action. Analysis of satellite images thus showed that cheniers reduce the minimum mudflat width required for mangrove expansion in Demak. Without cheniers, the tipping point between mangrove retreat and expansion is found for a mean mudflat width of 110 m[156]. With cheniers, the tipping point is observed for mudflat widths between 16-70 m[156], depending on the stability of the chenier. These minimum mudflat widths could serve as targets for future modelling work with bamboo structures. Moreover, they support the positive effect of cheniers on mangroves. However, chenier presence is temporary, as they are dynamic features that migrate through the coast[149,147]. With large subsidence rates and low sediment supplies, cheniers are likely insufficient to cause long-term mangrove expansion along the coast.

6.3.3. Minimizing scour seawards from the structures

Modelling scenarios with XMgrove predicted accretion landwards from the structures, but also erosion at their sea side. This erosion is induced by wave attenuation by the structures. The sudden decrease in wave height through a structure causes a drop in the sediment concentration, leading to an asymmetry in the sediment transport as more sediment travels landwards with the infilling tide than seawards with the falling tide. This imbalance in the sediment fluxes leads to erosion at the sea side of the structure and accretion at its land side.

Structures in the field also display erosion on their seaward side, which on average reached values around 20 cm. This value has the same order of magnitude in the model results. For example, XMgrove predicts 35 cm of erosion on the sea side of a structure placed 0.9 m below MSL over its first storm season. However, additional mechanisms could cause erosion in the field such as wave reflection and flow acceleration due to the presence of the structures (Figure 6.8).

The different mechanisms driving erosion in front of structures should thus be investigated for more accurate morphodynamic predictions. This requires integrating all processes into to a large-scale model that comprises the overall sediment balance and links all mechanisms, and evaluating their relative importance in a set of modelling scenarios. Such exercise would also enable finding strategies to minimize erosion seawards from the structures.

With respect to wave reflection, wave flume experiments already provide useful insights on how to reduce it. For instance, rows of

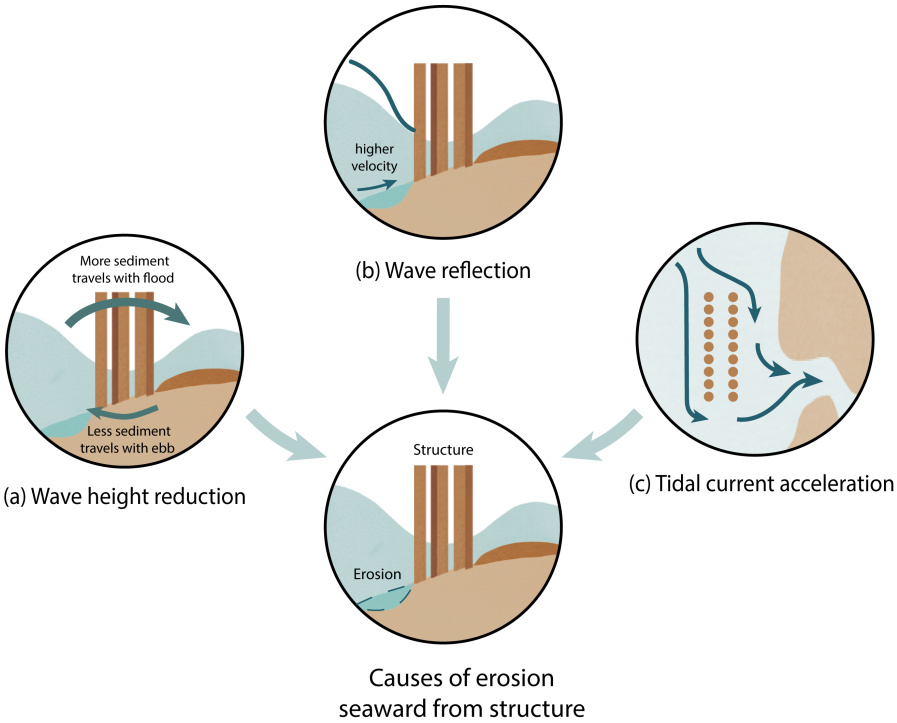

Figure 6.8: Causes from erosion seaward from a structure. (a) Wave height reduction by the structure causes a gradient in sediment concentration, and higher tidal sediment transport in the landwards direction. This results in sediment erosion at the sea side and accumulation at the land side of the structure. (b) Wave reflection increases the flow velocities near the bed at the sea side of the structure, enhancing erosion. (c) Acceleration of local currents near the structures can also induce erosion.

bamboo with a larger spacing in the wave direction induce less reflection than identical rows built closer to each other, which is also observed in the modelling work of Alferink[2]. Spreading rows of bamboo poles perpendicularly to waves could also reduce wave reflection, but the wave dissipation per element would decrease as well. The choice of configuration thus depends on a cost-benefit analysis considering the total material costs, the structure stability, and how erosion seawards from the structures will affect coastline expansion in the long term.

6.3.4. Optimum structure design for coastline expansion

At locations with sufficient sediment supply to stop coastal erosion, the rates of accretion behind the structures depend on how sediment is distributed by waves and currents. The classic literature on tidal flats identifies higher tidal ranges, associated to stronger tidal currents as the drivers of coastal progradation and convex profiles[47] whereas larger wave action erodes the profile, which develops a concave shape[47]. Since different physical conditions influence the coastal morphology, the optimal structure configuration and placement are most likely case-dependent.

In order to test how designs may vary in different circumstances, the optimum structure configuration is here investigated for a schematized coastal transect of French Guiana. Mangrove dynamics in French Guiana are linked to the migration of mud banks along the coast[48]. Mud banks are fine sediment deposits with a thickness between 5-10 m and widths between 10-20 km in the cross-shore direction. Whenever mud banks are present in front of the coast

(Figure 6.9 b), they attenuate waves and enhance sediment accumulation, leading to coastal progradation and mangrove expansion. Once the mud banks migrate away from a site, erosion and mangrove retreat take place (Figure 6.9 c)[48].

Mangrove degradation can be unfavorable for coastal protection purposes, especially at sites where the width of the mangrove forest has already been squeezed by human interventions. Bamboo and brushwood structures can also serve as a way to mitigate retreat when mudflats disappear from a site. The modelling approach of Chapter 4 is thus applied for a profile nearby Sinnamary, French Guiana, which experienced an average erosion rate of 117 m/year between 2000-2012[86]. In the model, a situation with an alongshore uniform stretch of coastline is assumed, where the alongshore sediment transport can be neglected, and with negligible subsidence and no external sediment supply. Scenarios with and without structure are considered, in order to find structure designs that halt coastline retreat and create new mangrove habitat, as illustrated in Figure 6.9 (d).

The input data and model parameters are obtained from a combination of open access datasets and literature of the area. The bathymetry of the site is obtained from the Blue Earth tool (https://blueearthdata.org), and the average monthly wave conditions of 2012 from Wave Watch III. The local tide is semi-diurnal, with a tidal range of 2.5 m, and it is represented using a sine component with the period of M2. The critical shear stress is set to a default value of 0.05 N/m^2, and the fall velocity is set to 0.1 mm/s[51]. The erodibility parameter is adjusted to $m_e = 0.8\ 10^{-4} kg/s/m^2$, in order reproduce a coastal retreat of 100 m over one year. The diffu-

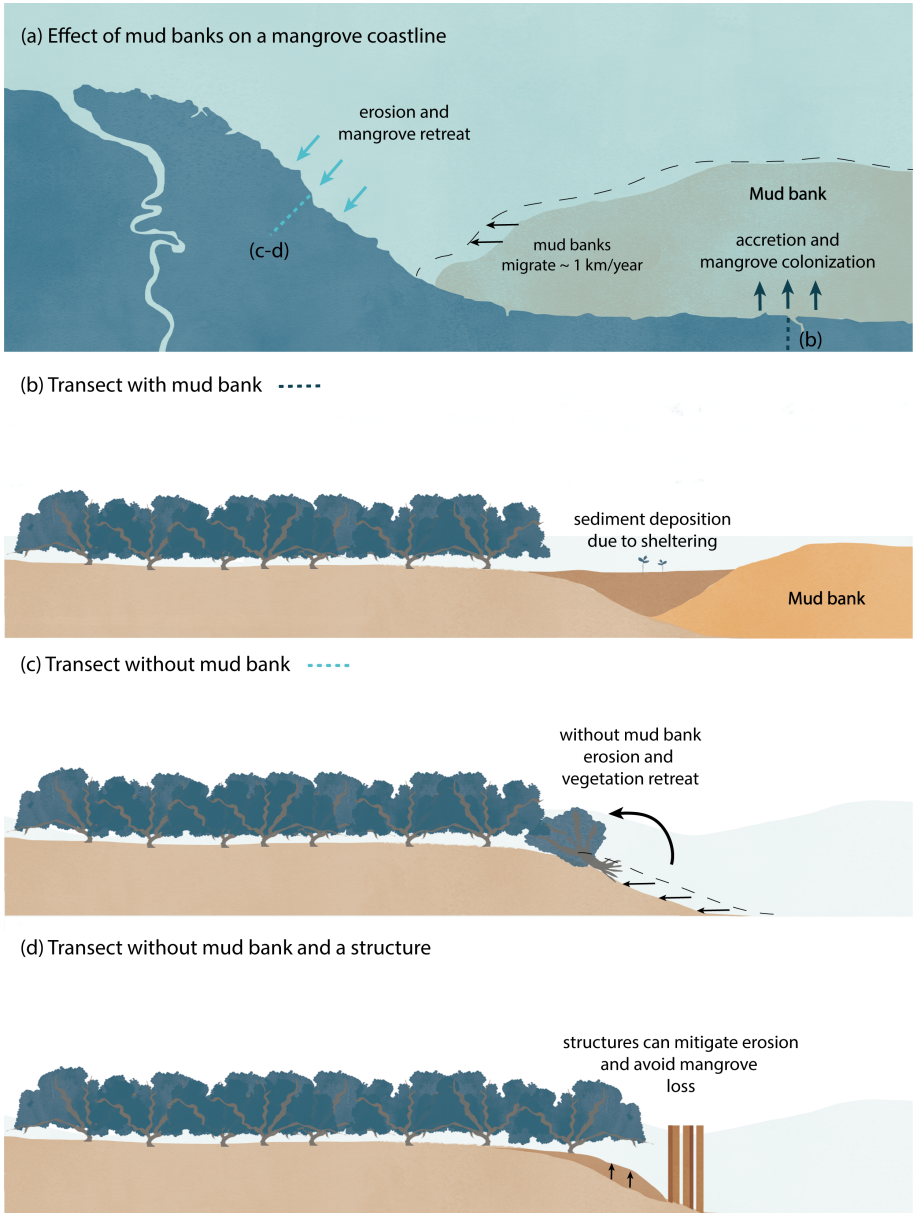

Figure 6.9: When mud banks migrate along mangrove coastlines (a), they shelter the coast from wave action, enhancing sediment accretion and mangrove colonization (b). When mud banks migrate away, shoreline retreat and mangrove loss take place (c). Structures could mitigate erosion and reduce mangrove mortality (d).

sion coefficient was estimated as the product between the maximum flow velocities (up to 0.5 m/s) and water depth (2 m) in the domain, resulting in $D = 1$ m^2/s. The modelled profile evolution after 1 year considering different brushwood structures locations (for structures with a width of 1 m, and a brushwood density of $N_v = 400$ elements/m^2) is shown in Figure 6.10.

The higher tidal range and the larger diffusion spread the sediment accumulation induced by the structures towards the upper part of the profile. For instance, a structure placed approximately -1 m with respect to MSL is already successful in causing coastal expansion after its first year, whereas in Demak coastline retreat was only mitigated by a similar design after 2 years. These scenarios consequently suggest that the performance of a design is heavily dependent on the local morphodynamic conditions.

Moreover, in the modelling scenarios of French Guiana, structures below and at MSL cause similar rates of wave height reduction. Their different effect on the coastline position was mostly due to their location and to the way sediment was locally distributed. Designs uniquely based on wave attenuation, without evaluating the morphodynamic processes, may thus fail in creating mangrove habitat.

6.4. Mapping mangrove opportunities

The first 3 chapters focus on the developing tools to design structures for mangrove restoration. Including these structures in coastal protection plans requires methods to systematically find the locations where they can be implemented. In Chapter 5 a map-

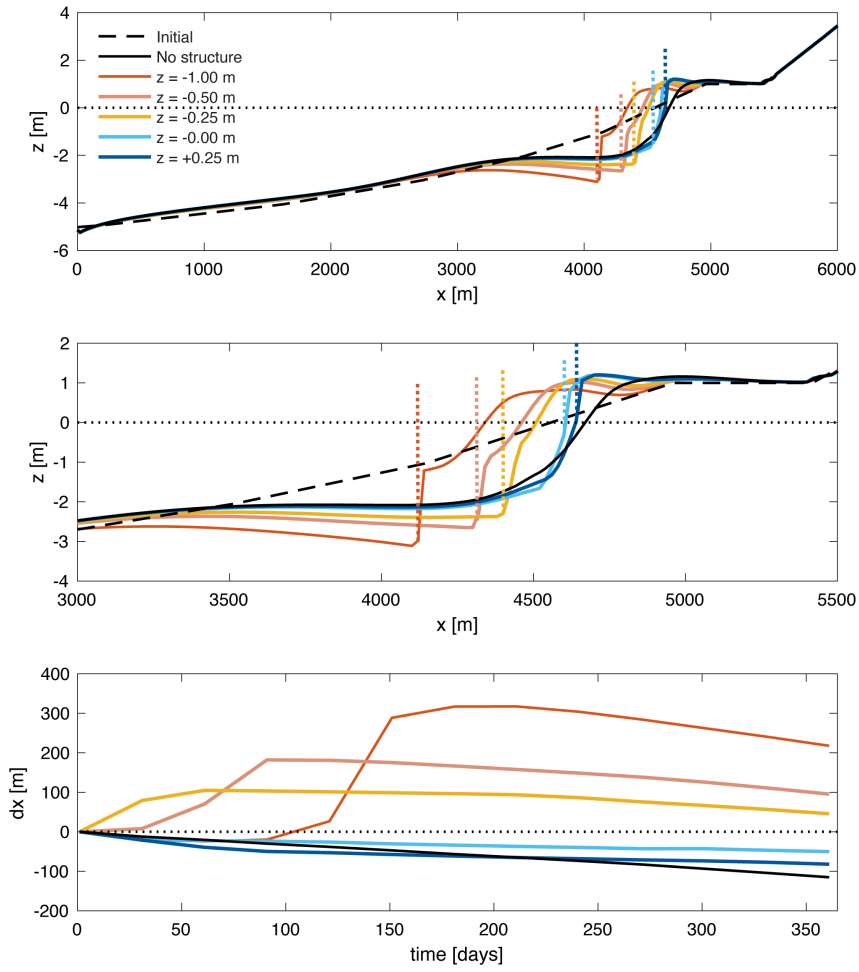

Figure 6.10: Effect of different structure designs for a schematized situation inspired in French Guiana. Plots (a-b) show the modelled cross-shore profile after 1 year for structures placed at different water depths. Plot (c) shows the change in the shoreline position (defined as the locations where the profile elevation is equal to MSL) over time for the different structures.

ping methodology is developed and applied for a case study of Bangladesh, as part of a World Bank project. The mapping tool identifies accreting coastal areas nearby existing mangroves, and prioritizes potential mangrove sites depending on the flood risk of the hinterland (with more vulnerable areas having higher priority).

This identification provides a first selection of areas for further investigation. However, the methods has limitations, some of them related to the conditions for mangrove suitability. Mangroves have specific requirements for the hydrology, freshwater input, and soil quality[42] that could not be investigated due to lack of data. The method is further based on the assumption that coastlines that on average expanded (i.e., moved seawards) over the last years are suitable for mangrove colonization.

In reality extreme events causing shear stresses (wave, current, or wind-driven) above the maximum thresholds of mangrove survival likely result in mangrove dislodgement or uprooting - even if the coastline expands in a year-averaged sense. Since the shear stresses will be largest during storm events, the timing of the biologic and physical processes is thus very important for mangrove colonization. For example, in Demak, Indonesia, the largest peak in seed production of the local pioneer species occurs during the stormiest and rainiest season. Fruiting during this period hinders mangrove establishment due to large wave action and erosion at the coast. For the case of Demak, this implies that large-scale mangrove colonization is episodic, and occurs during years with unusually calm monsoon seasons[156].

At locations where waiting for such episodes does not match the timeline set for coastal protection, planting during calm con-

ditions or using erosion-mitigation interventions could be options to accelerate the process. However, assessing the magnitude and time-evolution of the shear stresses at the coast of Bangladesh, or modelling its potential morphodynamic evolution is limited by data-scarcity (for example, it was not possible to identify published nearshore wave measurements along the coastal system, and datasets for the subsidence, sediment concentration, and bathymetry were also lacking).

The development of remote sensing tools over the next years will probably overcome some of these limitations, as they can potentially provide spatial and temporal distribution of physical variables like wave height, water levels, currents, and sediment turbidity, which in turn can lead to a deeper system understanding and more accurate mangrove suitability maps. Coupling those datasets with models like XMgrove (Chapter 4) can provide useful tools to investigate scenarios with different interventions and find those that would facilitate mangrove colonization.

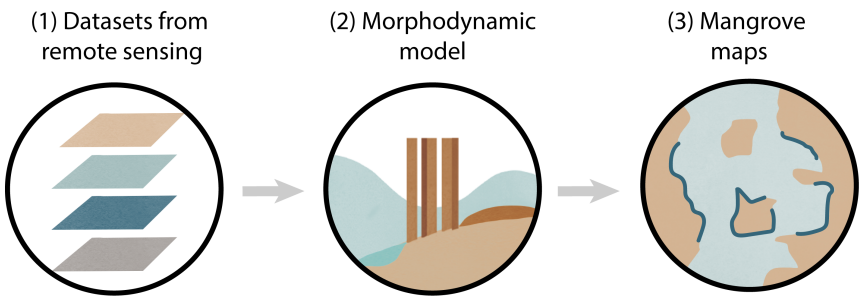

Figure 6.11: The combination of datasets of the relevant biophysical parameters for mangroves from remote sensing techniques and morphodynamic models like XMgrove will provide systematic ways of mapping mangrove opportunities

6.5. Mangrove conservation and management

This work investigates how to mitigate the effects of human interventions like deforestation or groundwater extraction, but it does not addresses the causes of the problem. The coastline of Demak, as many others, was almost fully deforested, excavated, and it is continuously sinking due to ground water extraction in and around Semarang. Mangroves were cut to build fish ponds that could only be exploited for 5 years, but with detrimental effects that last decades. Land subsidence also has catastrophic effects on local communities. Although structures can locally help to stop retreat and compensate some of the effects of ground subsidence, they depend on a local supply of sediment. The experience of the pilot and the current behavior of the coastline suggests that the subsidence rates in Demak are too high to be counteracted with structures.

This situation results from a lack of awareness of the value of mangroves, combined with a prioritization of short-term economical developments regardless of their long-term impacts - a frequent reasoning approach along coastlines all over the world. Wider awareness of the protective value of mangroves should be raised through education, and communication campaigns via social and digital media. Further research can also strengthen existing arguments to protect mangroves, and create new economic opportunities that incentivize nature preservation. At the governmental and legal level, large steps can be made to protect mangroves, such as legislation that protects mangrove areas, taxation of activities that damage them, and subsidizing activities that protect them.

These measures are key since Timbulsloko is not an isolated case, but a glimpse into the future of many areas. The road towards

Timbulsloko crosses an empty landscape, mostly water and sky. On stormy days the scenery is quite desolate, but during sunny days the road is surprisingly lively. People walk, cycle and ride in the only two possible directions. Buildings squeeze along two rows, one at each side of the road; tokos, schools, mosques. Both the road and the buildings are rebuilt every few years to offset subsidence, and the villagers resiliently adapt to every change.

One day there may be a limit to their adaptability, and Timbulsloko may become a modern Atlantis[18], but the resilience showed by its inhabitants is in some way hopeful. Humans can be impressively resourceful, and we will probably find ways to co-exist with climate change. However, adaptation and technological developments will take time. Every day that we waste in stopping relative sea level rise and protecting coastal ecosystems endangers the lives of millions of people in the future. It is in our hands to decide the type of world we hand down to future generations.

Bibliography

[1] O. Aburto-Oropeza et al. “Mangroves in the Gulf of California increase fishery yields”. In: *PNAS* 105 (2008).

[2] M. Alferink. “Wave transmission through permeable structures in Demak Indonesia A design study with the numerical model SWASH”. In: *TU Delft* (2022).

[3] S. Ali and W.S.J. Uijttewaal. “Flow resistance of vegetated oblique weir-like obstacles during high water stages”. In: *Hydrology and Earth System Sciences Discussions* 139.3 (2011). DOI: 10.5194/hess-18-1-2014.

[4] D.M. Alongi. “Present State and Future of the World’s Mangrove Forests”. In: *Environmental Conservation* 29 (2002).

[5] V. Arunachalam, J.J. Murray, and D.B. Muggeridge. “Flow interference between circular cylinders subjected to waves - A review”. In: *IEEE Boston, USA* (1981), pp. 943–951.

[6] L.N. Augustin, J.L. Irish, and P. Lynett. “Laboratory and numerical studies of wave damping by emergent and near-emergent wetland vegetation”. In: *Coastal Engineering* 56 (3 2009), pp. 332–340.

[7] M.A. Awal and A.F.M. Islam. “Water Logging in South-Western Coastal Region of Bangladesh: Causes and Consequences and People’s Response. ” In: *Asian Journal of Geographical Research* 3 (2020), pp. 9–28.

[8] K. Bagchi. “The Ganges Delta. University of Calcutta, Calcutta, India.” In: (1944).

[9] T.E. Baldock et al. “Cross-shore hydrodynamics within an unsaturated surf zone”. In: *Coastal Engineering* 34 (1988).

[10] T. Balke et al. “Limits to seaward expansion of mangroves: Translating physical disturbance mechanisms into seedling survival gradients”. In: *Marine Ecology Progress Series* 440 (2011).

[11] T. Balke et al. “Limits to seaward expansion of mangroves: Translating physical disturbance mechanisms into seedling survival gradients”. In: *Journal of Experimental Marine Biology and Ecology* 467 (2015).

[12] T. Balke et al. “Windows of opportunity: Thresholds to mangrove seedling establishment on tidal flats”. In: *Marine Ecology Progress Series* 440 (2011).

[13] T.Q. Bao. “Effect of mangrove forest structures on wave attenuation in coastal Vietnam”. In: *Oceanologia* 53 (2011).

[14] E.B. Barbier. “Capitalizing on Nature: Ecosystems as Natural Assets. Cambridge University Press.” In: (2011).

[15] E. Bayraktarov et al. “The cost and feasibility of marine coastal restoration”. In: *Ecological Applications* 26 (2015).

[16] S.J. Bennet, T. Pirim, and B.D. Barkdoll. “Using simulated emergent vegetation to alter stream flow direction within a straight experimental channel”. In: *Geomorphology* 44 (2002).

[17] U.S.N. Best et al. “Do salt marshes survive sea level rise? Modelling wave action, morphodynamics and vegetation dynamics”. In: *Environmental Modelling Software* 109 (2018).

[18] C.E.J. van Bijsterveldt. “Mangrove ecology and restoration at subsiding coastlines”. In: *PhD thesis University of Utretch* (2022).

[19] F. Blasco. “Outlines of ecology, botany and forestry of the mangals of the Indian subcontinent. In: Chapman VJ (ed) Wet coastal ecosys-tems, ecosystems of the world, vol 1. Elsevier, Amsterdam, pp 241–260.” In: (1977).

[20] R.D. Blevins. “Forces on and stability of a cylinder in a wake”. In: *Journal of Offshore Mechanics and Arctic Engineering* 127.1 (2005), pp. 39–45.

[21] A. Bokaian and F. Geoola. “Offshore Technology Conference”. In: *Marine Ecology Progress Series* (2008). DOI: 10.4043/5007-ms.

[22] W. Bolts. “Carte du Bengale et de ses dépendances”. In: *Universität Bern* (1775).

[23] L.M. Bricheno, J. Wolf, and S. Islam. “Tidal intrusion within a mega delta: An unstructured grid modelling approach”. In: *Estuarine, Coastal and Shelf Science* 182 (2016).

[24] D. Cannon et al. “Hydrodynamic habitat thresholds for mangrove vegetation on the shorelines of a microtidal estuarine lagoon”. In: *Ecological Engineering* 158 (2020).

[25] S. Chakrabarti. “Hydrodynamic coefficients for a vertical tube in an array”. In: *Applied Ocean Research* 3.1 (1 1981), pp. 1–12.

[26] N. Chaturvedi. “A new alternative host plant of teak defoliator Hyblaea puera (Hyblaeidae: Lepidoptera)”. In: *Journal of the Bombay Natural History Society* 92 (1995).

[27] N. Chaturvedi. “Some observations on teak defoliator Hyblaea puera (Lepidoptera: Hyblaeidae) on secondary host plant Avicennia marina. In Proceedings of the National Seminar on Creeks, Estuaries, and Mangroves: Pollution and Conservation, ed. G. Quadros. Thane, India: Department of Zoology, B. N. Banddkar College of Science, p. 289.” In: (2002).

[28] H. Chen et al. “Deriving vegetation drag coefficients in combined wave-current flows by calibration and direct measurement methods”. In: *Advances in Water Resources* 122 (2018), pp. 217–227.

[29] P.J. Clarke. “Dispersal of grey mangrove (Avicennia marina) propagules in southeastern Australia”. In: *EAquat. Bot* 45 (1993).

[30] C.V. Cuong et al. “Using Melaleuca fences as soft coastal engineering for mangrove restoration in Kien Giang, Vietnam”. In: *Ecological Engineering* 81 (2015), pp. 256–265. ISSN: 0925-8574. DOI: 10.1016/j.ecoleng.2015.04.031. URL: http://dx.doi.org/10.1016/j.ecoleng.2015.04.031.

[31] S.J. Curtis. “Working plan for the forests of the Sundarbans Division for the period from 1st April 1931 to 31st March 1951, Volume III Part of Appendix III Description of the Compartments and their Histories. Government of Bengal ”. In: (1933).

[32] R. Dalrymple, J. Kirby, and P. Hwang. “Wave Diffraction Due to Areas of Energy Dissipation”. In: *Journal of Waterway, Port, Coastal and Ocean Engineering* 110 (1 1984), pp. 67–79.

[33] H.T. Dao et al. “Experimental Assessment of the Flow Resistance of Coastal Wooden Fences”. In: *Water* 12 (2020).

[34] T. Dao. “Hydraulic performance of brushwood fences for mangrove replantation in the Mekong Delta”. In: *PhD thesis TU Delft* (2021).

[35] S. Dasgupta et al. “Vulnerability of Bangladesh to Cyclones in a Changing Climate: Potential Damages and Adaptation Costs. Policy Research Working aper 5280, The World Bank Development Research Group, Environment and Energy Team”. In: (2010).

[36] Deltares. “Ecological mangrove restoration by use of permeable structures. Monitoring of the Permeable structures. Report version 02”. In: (2020).

[37] Deltares and BioManCO. “Sediment analysis of Demak. Report version 01”. In: (2019).

[38] I. Eames, C. Jonsson, and P.B. Johnson. “The growth of a cylinder wake in turbulent flow”. In: *Journal of Turbulence* 12 (2011).

[39] D. Eckstein et al. “Global Climate Risk Index 2019”. In: *Germanwatch e.V.* (2020).

[40] Ecoshape. *Building with Nature Indonesia; Securing Eroding Delta Coastlines. Technical report.* 2015.

[41] A.M. Ellison, B.B Mukherjee, and A. Karim. “Testing patterns of zonation in mangroves: scale dependence and environmental correlates in the Sundarbans of Bangladesh”. In: *Journal of Ecology* 88 (2000).

[42] J.C. Ellison. “Impacts of Sediment Burial on Mangroves”. In: *Marine Pollution Bulletin* 37 (8–12 1999), pp. 420–426.

[43] V. Etminan, R.J. Lowe, and M. Ghisalberti. “A new model for predicting the drag exerted by vegetation canopies”. In: *Water Resources Research* 53 (2017).

[44] V. Etminan, R.J. Lowe, and M. Ghisalberti. “Canopy resistance on oscillatory flows”. In: *Coastal Engineering* 152 (2019). ISSN: 0378-3839. DOI: 10.1016/j.coastaleng.2019.04.014. URL: https://doi.org/10.1016/j.coastaleng.2019.04.014.

[45] FAO. “The world’s mangroves 1980–2005”. In: *FAO Forestry Paper* 153 (2007), p. 89.

[46] M.S. Fonseca and J.A. Calahan. “A preliminary evaluation of wave attenuation by four species of seagrasses”. In: *Estuarine, Coastal and Shelf Science* 35 (1992), pp. 565–576.

[47] C.T. Friedrichs. “Tidal flat morphodynamics: a synthesis”. In: *Treatise on Estuarine and Coastal Science: Sedimentology and Geology. Elsevier, pp. 137-170.* (2011).

[48] J.M Froidefond, M. Pujos, and X. Andre. “Migration of mud banks and changing coastline in French Guiana”. In: *Marine Geology* 84 (1988).

[49] Y. Goda and T. Suzuki. “Estimation of incident and reflected waves in random wave experiments”. In: *Coastal Engineering Proceedings* 1.15 (1976).

[50] J.M.R. Graham. “The forces on sharp-edged cylinders in oscillatory flow at low Keulegan-Carpenter numbers”. In: *Journal of Fluid Mechanics* 97 (2 1980).

[51] N. Gratiot and E.J. Anthony. “The role of flocculation and settling processes in geological development of the mangrove-colonized, Amazon-influenced mud bank coast of South America”. In: *Marine Geology* 373 (2016).

[52] Z. Gu and T. Sun. “On interference between two circular cylinders in staggered arrangement at high subcritical Reynolds numbers”. In: *Journal of Wind Engineering and Industrial Aerodynamics* 80.3 (1999), pp. 287–309. ISSN: 01676105. DOI: 10.1016/S0167-6105(98)00205-0.

[53] W.L Hakim, A.R. Achmad, and C.W. Lee. “Land Subsidence Measurement of Jakarta Coastal Area Using Time Series Interferometry with Sentinel-1 SAR Data”. In: *Advances in Geospatial Research of Coastal Environments. Journal of Coastal Research* 102 (2020).

[54] J.C. Heideman and T. Sarpkaya. “Hydrodynamic Forces on Dense Arrays of Cylinders”. In: *Offshore Technology Conference* (2008).

[55] P.J. Hochard, S. Hamilton, and E.B. Barbier. “Mangroves shelter coastal economic activity from cyclones”. In: *PNAS* 116 (2018), pp. 12232–12237.

[56] E. Horstman et al. “Wave attenuation in mangroves: A quantitative approach to field observations”. In: *Coastal Engineering* 94 (2014), pp. 47–62.

[57] J. van Houwelingen et al. “The effect of finger spreading on drag of the hand in human swimming”. In: *Journal of Biomechanics* 63.November (2016). arXiv: arXiv:1611.08578v1.

[58] Z. Hu et al. “Laboratory study on wave dissipation by vegetation in combined current–wave flow”. In: *Coastal Engineering* 88 (2014), pp. 131–142.

[59] Delft Hydraulics. *Manual for Wave Height Meter*. year unknown.

[60] Delft Hydraulics. *User’s manual for the Delft hydraulics four quadrant electromagnetic liquid velocity meter*. 1990.

[61] M.S. Iftekhar and M.R. Islam. “Degeneration of Bangladesh Sundarbans mangroves: a management issue”. In: *Int Forest Rev* 6 (2004).

[62] M.S. Iftekhar and P. Saenger. “Vegetation dynamics in the Bangladesh Sundarbans mangroves: a review of forest inventories”. In: *Wetlands Ecol Manage* 16 (2008), pp. 291–312.

[63] IPCC. “Climate Change 2007: Impacts, Adaptation and Vulnerability: Summary for Policymakers. Working Group II Contribution to the Intergovernmental Panel on Climate Change Fourth Assessment Report. IPCC, Geneva”. In: (2007).

[64] A.S. Islam et al. “Performance of Coastal Structures during Cyclone Sidr. ” In: *Natural Hazards* 12 (2011).

[65] A.S. Islam et al. “Project Appraisal Document of People’s Republic of Bangladesh Coastal Embankment Improvement Project-Phase 1 (CEIP-1) (P128276)”. In: *Report No.: PAD432* (2013).

[66] Kairo J.G. et al. “Restoration and management of mangrove systems – a lesson for and from the East African region”. In: *S Afr J Bot* 67 (2001).

[67] F. Jakobsen et al. “Valuation of the Short-Term Processes Forcing the Monsoon River Floods in Bangladesh”. In: *Water International* 30 (2005), pp. 389–399.

[68] W.J. Jansen. “Wave dissipation in a permeable structure”. In: *MSc thesis, Delft University of Technology* (2019).

[69] S.N. Jonkman, M. Kok, and J.K Vrijling. “Flood Risk Assessment in the Netherlands: A Case Study for Dike Ring South Holland ”. In: *Risk Analysis* 28 (2008).

[70] M.F. Karim and Mimura N. “Impacts of climate change and sea-level rise on cyclonic storm surge floods in Bangladesh”. In: *Global Environmental Change* 18 (2008), pp. 490–500.

[71] K. Kathiresan and N. Rajendran. “Coastal mangrove forests mitigated tsunami”. In: *Estuarine, Coastal and Shelf Science* 65 (2005).

[72] G. H. Keulegan and L. H. Carpenter. “Forces on cylinders and plates in an oscillating fluid”. In: *J. Res. Nat. Bur. Standards* 60 (1958), pp. 423–440.

[73] R.S. Khan. "Cyclone Hazard in Bangladesh". In: *Community Development library, Dhaka, 86–102. National States Geographic Information Council. Available online: www.adpc.net* (1992).

[74] S.J. Kim and T. Stoesser. "Closure modeling and direct simulation of vegetation drag in flow through emergent vegetation". In: *Water Resources Research* 17 (2011), pp. 1–15.

[75] J.T. Kirby and R.A. Dalrymple. "An approximate model for nonlinear dispersion in monochromatic wave propagation models". In: *Coastal Engineering* 9.6 (1986), pp. 545–561.

[76] K.W. Krauss et al. "Water level observations in mangrove swamps during two hurricanes in Florida". In: *Wetlands* 29 (2009), pp. 142–149.

[77] S.A. Kulp and B.H. Strauss. "New elevation data triple estimates of global vulnerability to sea-level rise and coastal flooding". In: *Nature Communications* 10 (2019).

[78] R.R. Lewis and B. Brown. "Ecological mangrove rehabilitation – a field manual for practitioners. Version 3. Mangrove Action Project Indonesia, Blue Forests, Canadian International Development Agency, and OXFAM. p 275". In: (2014).

[79] R.R. Lewis III. "Ecological engineering for successful management and restoration of mangrove forests". In: *Ecological Engineering* 24.4 (2005), pp. 403–418. DOI: 10.1016/j.ecoleng.2004.10.003.

[80] R.R. Lewis III. “Methods and criteria for successful mangrove forest restoration. In: Gerardo M. E. Perillo, Eric Wolanski, Donald R. Cahoon, Mark M. Brinson, editors, Coastal Wetlands: An Integrated Ecosystem Approach. Elsevier, 2009, p. 787. ISBN: 978-0-444-53103-2 ”. In: (2009).

[81] R.M Li and Shen H.W. “Effect of tall vegetations on flow and sediment”. In: *J Hydraul Div* 99 (1973), pp. 793–814.

[82] K. Lindner. “Der Strömungswiderstand von Pflanzenbeständen”. In: *Mitt. Liechtweiß-Institut für Wasserbau Technische Universitat Bräunschweig* 75 (1982), pp. 905–920.

[83] X. Liu, M. Levitan, and D. Nikitopoulos. “Wind tunnel tests for mean drag and lift coefficients on multiple circular cylinders arranged in-line”. In: *Journal of Wind Engineering and Industrial Aerodynamics* 96.6-7 (2008), pp. 831–839. ISSN: 01676105. DOI: 10.1016/j.jweia.2007.06.011.

[84] J.L. Lopez-Portillo et al. “Mangrove Forest Restoration and Rehabilitation. Mangrove Ecosystems: A Global Biogeographic Perspective. Springer, Cham. https://doi.org/10.1007/978-3-319-62206-4_1”. In: (2017).

[85] C.E. Lovelock et al. “The vulnerability of Indo-Pacific mangrove forests to sea-level rise”. In: *Nature* 526 (2015).

[86] A. Luijendijk et al. “The State of the World’s Beaches”. In: *Scientific Reports* 8 (2018).

[87] A. Lygre and H. E. Krogstad. “Maximum Entropy Estimation of the Directional Distribution in Ocean Wave Spectra”. In: *Journal of Physical Oceanography* 16.12 (1986), pp. 2052–2060.

[88] C. Maan et al. “Morphodynamic Feedback Loops Control Stable Fringing Flats”. In: *Journal of Geophysical Research: Earth Surface* 123 (2018).

[89] M. Marfai et al. “The Morphodynamics of Wulan Delta and Its Impacts on the Coastal Community in Wedung Subdistrict, Demak Regency, Indonesia”. In: *Journal of Environmental Protection* 7 (2016), pp. 60–71.

[90] G. Mariotti and S. Fagherazzi. “A numerical model for the coupled long-term evolution of salt marshes and tidal flats”. In: *Journal of Geophysical Research* 115 (2010).

[91] S.R. Massel, K. Furukawa, and R.M. Brinkman. “Surface wave propagation in mangrove forests.” In: *Fluid Dynamics Research* 24 (1999).

[92] M. Maza, J.J Lara, and I.J. Losada. “Experimental analysis of wave attenuation and drag forces in a realistic fringe Rhizophora mangrove forest. ” In: *Advances in Water Resources* 131 (2019), pp. 69–87.

[93] Y. Mazda, E. Wolanski, and B. King. “Drag force due to vegetation in mangrove swamps. ” In: *Mangroves and Salt Marshes* 1 (1997), pp. 193–199.

[94] A. McIvor et al. “Reduction of wind and swell waves by mangroves. Natural coastal protection series: Report 1. Cambridge coastal research unit working paper 40. The nature conservancy, Arlington, USA/Wetlands International, Wageningen, Netherlands, pp 27”. In: (2012).

[95] K.L. McKee and W.C. Vervaeke. “Will fluctuations in salt marsh–mangrove dominance alter vulnerability of a subtropical wetland to sea-level rise?” In: *Global Change Biology* 28 (2018).

[96] B. Meftah and M. Mossa. “Prediction of channel flow characteristics through square arrays of emergent cylinders”. In: *Physics of Fluids* 25.March 2013 (2017). DOI: 10.1063/1.4802047.

[97] F.J. Méndez and I.J. Losada. “An empirical model to estimate the propagation of random breaking and nonbreaking waves over vegetation fields”. In: *Coastal Engineering* 51 (2004), pp. 103–118.

[98] P. Menéndez et al. “The Global Flood Protection Benefits of Mangroves”. In: *Scientific Reports* 1.10 (2020).

[99] J. M. Montgomery et al. “Attenuation of storm surges by coastal mangroves”. In: *Geophysical Research Letters* 46 (2019), pp. 2680–2689.

[100] J.M. Montgomery et al. “Attenuation of Tides and Surges by Mangroves: Contrasting Case Studies from New Zealand”. In: *Water* 10 (2018).

[101] J. R. Morison et al. “The force exerted by surface waves on piles”. In: *Petroleum Trans.* 189 (1950), pp. 149–157.

[102] M. Mossa et al. “How vegetation in flows modifies the turbulent mixing and spreading of jets”. In: *Scientific Reports* 7 (2017), pp. 1–14. DOI: 10.1038/srep39103.

[103] D. Murdiyarso et al. “The potential of Indonesian mangrove forests for global climate change mitigation”. In: *Nature Climate Change* 5 (2015).

[104] N.J. Murray et al. “Global distribution and trajectory of tidal flats”. In: *Nature* 565 (2019).

[105] F. Naz and M.C. Buisson. “Multiple actors, conflicting roles and perverse incentives: the case of poor operation and maintenance of coastal polders in Bangladesh”. In: *Proceedings of the CPWF, GBDC, WLE Conference on Revitalizing the Ganges Coastal Zone: Turning Science into Policy and Practices, Dhaka, Bangladesh, 21-23 October 2015.* (2015), pp. 147–161.

[106] H.M. Nepf. “Drag, turbulence, and diffusion in flow through emergent vegetation”. In: *Water Resources Research* 35.2 (1999), pp. 479–489.

[107] I. Nezu and H. Nakagawa. *Turbulence in Open-channel Flow.* 7th. IAHR Monograph, Balkema, Rotterdam, The Netherlands, 1993.

[108] T.P. Nguyen and Kevin E. Parnell. “Gradual expansion of mangrove areas as an ecological solution for stabilizing a severely eroded mangrove dominated muddy coast”. In: *Ecological Engineering* 107.August (2017), pp. 239–243. DOI: 10.1016/j.ecoleng.2017.07.038.

[109] R.J. Nicholls, F.M.J. Hoozemans, and M. Marchand. “Increasing flood risk and wetland losses due to global sea-level rise: regional and global analyses”. In: *Global Environmental Change* 9 (1999), pp. 69–87.

[110] A. Nishat. “Review of present activities and state of art of the coastal areas of Bangladesh. Coastal area resource development and management Part II”. In: *Dhaka, Coastal Area Resource Development and Management Association (CARDMA)* (1988), pp. 22–35.

[111] Nortek. *Vectrino technical specification.* 2020.

[112] B.D Obasaju, P.W. Bearman, and J.M.R. Graham. “A study of forces, circulation and vortex patterns around a circular cylinder in oscillating flow”. In: *Journal of Fluid Mechanics* 196 (1988), pp. 467–494.

[113] Y. Ozeren, D.G. Wren, and W. Wu. “Experimental Investigation of Wave Attenuation through Model and Live Vegetation”. In: *Journal of Waterway, Port, Coastal, and Ocean Engineering* 140 (5 2014).

[114] B.K. Paul. “Why relatively fewer people died? The case of Bangladesh’s Cyclone Sidr. ” In: *Natural Hazards* 50 (2009), pp. 289–304.

[115] S. Petryck. “Drag on cylinders in open channel flow”. PhD thesis. Colorado State University, Fort Collins, 1969.

[116] L. Phan et al. “The effects of wave non-linearity on wave attenuation by vegetation”. In: *Coastal Engineering* 147 (2019), pp. 63–74.

[117] A. Pranchai, M. Jenke, and U. Berger. “Well-intentioned, but poorly implemented: Debris from coastal bamboofences triggered mangrove decline in Thailand”. In: *Marine Pollution Bulletin* 146 (2019).

[118] J.H. Primavera and J.M.A. Esteban. “A review of mangrove rehabilitation in the Philippines: successes, failures and future prospects”. In: *Wetlands Ecology and Management volume* 16 (2008), pp. 345–358.

[119] Multi-purpose Cyclone Shelter Project. “Summary report. Dhaka: Bangladesh University of Engineering and Technology and Bangladesh Institute of Development Studies”. In: (1993).

[120] D. Rabinowitz. “Dispersal Properties of Mangrove Propagules”. In: *Biotropica* 10.1 (1978), pp. 47–57.

[121] A.J.H.M. Reniers and A. Gijón Mancheño. “XMgrove: Morphodynamic Mangrove Profile Modeling”. In: *Frontiers in Marine Science (submitted)* (2022).

[122] C.B. Rizzo and F.P.J. de Barros. “Minimum Hydraulic Resistance and Least Resistance Path in Heterogeneous Porous Media”. In: *Water Resources Research* (2017), pp. 8596–8613.

[123] A. van Rooijen et al. “Predicting Current-Induced Drag in Emergent and Submerged Aquatic Vegetation Canopies”. In: *Frontiers in Marine Science* 5.December (2018), pp. 1–14. DOI: 10.3389/fmars.2018.00449.

[124] P. Saenger and N.A. Siddiqi. “Land from the sea: The mangrove afforestation program of Bangladesh”. In: *Ocean Coastal Management* 20 (1993), pp. 23–39.

[125] N. Saintilan et al. “Thresholds of mangrove survival under rapid sea level rise”. In: *Science* 368 (2020).

[126] N. Saintilan et al. “Thresholds of mangrove survival under rapid sea level rise”. In: *Science* 368 (2020).

[127] D.A. Sánchez-Náuñez, G. Bernal, and J.E. Mancera Pineda. “The Relative Role of Mangroves on Wave Erosion Mitigation and Sediment Properties”. In: *Estuaries and Coasts* 42 (2019).

[128] T. Sarpkaya. “Hydrodynamic forces on various multiple-tube riser configurations”. In: *Offshore technology conference. Houston, Texas.* (1979). DOI: 10.3389/fmars.2018.00449.

[129] S.D. Sasmito et al. In: *Wetlands Ecology and Management* 24 (2016).

[130] SCAIME. *Manual Load cell - Single point - AL.* 2020.

[131] K. Schmitt et al. “Site-specific and integrated adaptation to climate change in the coastal mangrove zone of Soc Trang Province, Viet Nam”. In: *Journal of Coastal Conservation* 17.3 (2013), pp. 545–558. DOI: 10.1007/s11852-013-0253-4.

[132] T. Schoneboom, J. Aberle, and A. Dittrich. “Spatial Variability, Mean Drag Forces, and Drag Coefficients in an Array of Rigid Cylinders”. In: *Experimental Methods in Hydraulic Research* 1 (2011), pp. 255–265.

[133] S.C. Snedaker. “Mangrove species zonation: Why?” In: *Tasks for Vegetation Science* 2 (1982).

[134] F. Sonnenwald, V. Stovin, and I. Guymer. “Estimating drag coefficient for arrays of rigid cylinders representing emergent vegetation”. In: *Journal of Hydraulic Research* 1686 (2019). DOI: 10.1080/00221686.2018.1494050. URL:

https://doi.org/10.1080/00221686.2018.1494050.

[135] M.F. Staveren, J.F. Warner, and M.S.A. Khan. "Bringing in the tides. From closing down to opening up delta polders via Tidal River Management in the southwest delta of Bangladesh". In: *Water Policy* 19 (2017), pp. 147–164.

[136] B.M. Sumer and J. Fredsoe. *Hydrodynamics around cylindrical structures*. 1st. World Scientific, 1997.

[137] D. Sumner. "Two circular cylinders in cross-flow: A review". In: *Journal of Fluids and Structures* 26.6 (2010), pp. 849–899. ISSN: 08899746. DOI: 10.1016/j.jfluidstructs.2010.07.001. URL: http://dx.doi.org/10.1016/j.jfluidstructs.2010.07.001.

[138] F. Sun and R.T. Carson. "Coastal wetlands reduce property damage during tropical cyclones". In: *Coastal Engineering* 117 (2020), pp. 5719–5725.

[139] T. Suzuki. "Wave dissipation over vegetation fields". In: *PhD Thesis. Delft University of Technology* (2011).

[140] T. Suzuki and T. Arikawa. "Numerical analysis of bulk drag coefficient in dense vegetation by immersed boundary method". In: *Proceedings of the 32nd International Conference on Coastal Engineering, ICCE 2010, June/July, Shanghai* (2010). DOI: 10.3389/fmars.2018.00449.

[141] T. Suzuki et al. "Non-hydrostatic modeling of drag, inertia and porous effects in wave propagation over dense vegetation fields". In: *Coastal Engineering* 149 (2019), pp. 49–64.

[142] T. Suzuki et al. “Wave dissipation by vegetation with layer schematization in SWAN”. In: *Coastal Engineering* 59 (2012), pp. 64–71.

[143] N. Tanaka. “Effectiveness and Limitations of Vegetation Bioshield in Coast for Tsunami Disaster Mitigagation”. In: (2011).

[144] N. Tanaka et al. “Coastal vegetation structures and their functions in tsunami protection: experience of the recent Indian Ocean tsunami”. In: *Landscape and Ecological Engineering* 3 (2007).

[145] N. Tanaka et al. “Coastal vegetation structures and their functions in tsunami protection: experience of the recent Indian Ocean tsunami”. In: *Landscape Ecology and Engineering* 3 (2007).

[146] Y. Tanino and Heidi M. Nepf. “Laboratory Investigation of Mean Drag in a Random Array of Rigid, Emergent Cylinders”. In: *Journal of Hydraulic Engineering* 134.1 (2008), pp. 34–41. ISSN: 0733-9429. DOI: 10.1061/(asce)0733-9429(2008)134:1(34).

[147] S.A.J. Tas. “Chenier dynamics”. In: *PhD thesis TU Delft* (2022).

[148] S.A.J. Tas, D.S. van Maren, and A.J.H.M. Reniers. “Drivers of cross-shore chenier dynamics off a drowning coastal plain”. In: *Marine Geology (submitted)* (2021).

[149] S.A.J. Tas, D.S. van Maren, and A.J.H.M. Reniers. “Observations of Cross-Shore Chenier Dynamics in Demak, Indonesia”. In: *Journal of Marine Science and Engineering* 8 (2020).

[150] R.O. Tinoco and E.A. Cowen. "The direct and indirect measurement of boundary stress and drag on individual and complex arrays of elements". In: *Experiments in Fluids* 54.4 (2013). ISSN: 07234864. DOI: 10.1007/s00348-013-1509-3.

[151] U. Trampanya. "Mangroves and sediment dynamics along the coasts of southern Thailand". In: *PhD thesis. Wageningen University and Research* (2019).

[152] S.H. Truong, Q. Ye, and M.J.F. Stive. "Estuarine Mangrove Squeeze in the Mekong Delta, Vietnam". In: *Journal of Coastal Research* 33 (2017), pp. 747–763.

[153] Vuik V. et al. "Assessing safety of nature-based flood defenses: Dealing with extremes and uncertainties". In: *Coastal Engineering* 139 (2018), pp. 47–64.

[154] Vuik V. et al. "Salt marshes for flood risk reduction: Quantifying long-term effectiveness and life-cycle costs". In: *Ocean Coastal Management* 171 (2019), pp. 96–110.

[155] A. del Valle et al. "Mangroves for Coastal Protection : Evidence from Hurricanes in Central America". In: *Policy Research Working Paper; No. 8795. World Bank, Washington, DC.* (2019).

[156] C.E.J. Van Bijsterveldt et al. "Can cheniers protect mangroves along eroding coastlines? – A study investigating the effect of different fore-shores on long-term stability of mangroves". In: *(in preparation for submission)* (2022).

[157] C.E.J. Van Bijsterveldt et al. “How to restore mangroves for greenbelt creation along eroding coasts with abandoned aquaculture ponds”. In: *Estuarine, Coastal and Shelf Science* 235 (2020), p. 106576. ISSN: 0272-7714. DOI: https://doi.org/10.1016/j.ecss.2019.106576. URL: http://www.sciencedirect.com/science/article/pii/S0272771419305669.

[158] C.E.J. Van Bijsterveldt et al. “To plant or not to plant: when can planting facilitate mangrove restoration?” In: *Frontiers in Environmental Science* 9 (2022).

[159] J.W. Van der Meer et al. “Manual on wave overtopping of sea defences and related structures. An overtopping manual largely based on European resreach, but for worldwide application. www.overtopping-manual.com: EurOtop”. In: (2018).

[160] T. Van Domburg. “Identifying Windows of Opportunity for Mangrove Establishment on a Mud Coast”. In: *MSc thesis, Delft University of Technology* (2018).

[161] A.F. Van Loon et al. “Hydrological Classification, a Practical Tool for Mangrove Restoration”. In: *PLoS ONE* 11 (2016).

[162] P. Van Santen et al. “Sedimentation in an estuarine mangrove system”. In: *Journal of Asian Earth Sciences* 29.4 (2007). Morphodynamics of the Red River Delta, Vietnam, pp. 566–575. DOI: https://doi.org/10.1016/j.jseaes.2006.05.011.

[163] A.G. Vovides, Y. Bashan, and Guevara R. López-Portillo J. “Nitrogen fixation in preserved, reforested, naturally regenerated and impaired mangroves as an indicator of functional

restoration in mangroves in an arid region of Mexico". In: *Restor Ecol* 29 (2019).

[164] Y.Q. Wang, Z.F. Wang, and W.C. Cheng. "A review on land subsidence caused by groundwater withdrawal in Xian, China". In: *Bulletin of Engineering Geology and the Environment* 78 (2018).

[165] B. K. van Wesenbeeck et al. "Aquaculture induced erosion of tropical coastlines throws coastal communities back into poverty". In: *Ocean and Coastal Management* 116 (2015), pp. 466–469. ISSN: 09645691. DOI: 10.1016/j.ocecoaman.2015.09.004. URL: http://dx.doi.org/10.1016/j.ocecoaman.2015.09.004.

[166] F. M. White. *Viscous fluid flow*. 2nd. McGraw-Hill, New York., 1991.

[167] A.J. Whitten and S.J. Damanik. "Mass defoliation of mangroves in Sumatra, Indonesia". In: *Biotropica* 18 (1986).

[168] J.C. Winterwerp, W.G. Borst, and M.B. Vries. "Pilot Study on the Erosion and Rehabilitation of a Mangrove Mud Coast Pilot Study on the Erosion and Rehabilitation of a Mangrove Mud Coast". In: *Journal of Coastal Research* 21.2 (2005), pp. 223–230. DOI: 10.2112/03-832A.1.

[169] J.C. Winterwerp et al. "Defining Eco-Morphodynamic Requirements for Rehabilitating Eroding Mangrove-Mud Coasts". In: *Wetlands* 33.3 (2013), pp. 515–526. DOI: 10.1007/s13157-013-0409-x.

[170] C.D. Woodroffe et al. “Mangrove Sedimentation and Response to Relative Sea-Level Rise”. In: *Annual Review of Marine Sciences* 8 (2016).

[171] T.A. Worthington and M.D. Spalding. “Mangrove Restoration Potential: A global map highlighting a critical opportunity.” In: (2018).

[172] Y. Xie, S. Shekhar, and Y. Li. “Statistically-Robust Clustering Techniques for Mapping Spatial Hotspots: A Survey”. In: (2021).

[173] Y. Xie et al. “Discovering Spatial Mixture Patterns of Interest. In Proceedings of the 28th ACM SIGSPATIAL International Conference on Advances in Geographic Information Systems (pp. 608-617)”. In: (2020).

[174] B.D Yuwono et al. “Time Series of Land subsidence rate on Coastal Demak Using GNSS CORS UDIP and DINSAR ”. In: *E3S Web of Conferences* 94 (2019). DOI: 10.1051/e3sconf/20199404004.

[175] S. Zaman and M.S. Mondal. “Risk-based determination of polder height against storm surge Hazard in the south-west coastal area of Bangladesh”. In: *Progress in Disaster Science* 8 (2020).

[176] M.M. Zdravkovich. “The effects of interference between circular cylinders in cross flow”. In: *Journal of Fluids and Structures* 1.2 (1986), pp. 239–261. ISSN: 08899746. DOI: 10.1016/s0889-9746(87)90355-0.

[177] Y. Zhou and M. Mahbub Alam. “Wake of two interacting circular cylinders: A review”. In: *International Journal of Heat and Fluid Flow* 62 (2016), pp. 510–537. ISSN: 0142727X. DOI: 10.1016/j.ijheatfluidflow.2016.08.008. URL: http://dx.doi.org/10.1016/j.ijheatfluidflow.2016.08.008.

A. Appendix A

Validation data

The data that support the findings of this study were directly obtained from the graphs of Tanino and Nepf[146] and Tinoco and Cowen[150], and from the dataset collected by Jansen[68]. Jansen[68] conducted laboratory experiments in the wave and current flume at Delft University of Technology, in order to measure the hydrodynamic forces acting on groups of cylinders with varying geometrical configurations with currents and waves. His report[68] focuses on the description of flume experiments with waves, and we have thus included a more detailed explanation of the experiments with currents in the present section.

The flume is 40 m long, 0.8 m wide and 0.8 m high. A continuous inflow of water was pumped into the flume, while the water level upstream from the cylinder array was kept at a constant level of $h = 0.55$ m. The pumping rates were adjusted to obtain three different depth-averaged flow velocities of $0.1, 0.2$ and 0.4 m/s. These values corresponded with Re values of 4,000, 8,000 and 16,000, where Re is the Reynolds number based on cylinder diameter and incoming velocities upstream from the structure. A frame with cylinders was placed in the middle of the flume, as illustrated in Figure A.1 (a).

The physical model consisted of a grid of 0.76 x 0.76 m, where aluminum cylinders could be introduced in different arrangements. The elements were held together by a top and a bottom plate. The tested volumetric porosities ranged between $n = 0.64 - 0.9$. The cylinder diameter was $d = 0.04$ m for all experiments. The tested configurations are illustrated in Figure A.1 (b). The properties of the configurations are summarized in Figure 2.3.

The locations of the instruments used during the experiments are presented in Figure A.1 (a). All the instruments were measuring continuously with a frequency of 100 Hz. An electromagnetic flow meter (EMF) was placed at a distance of 0.4 m upstream from the structure, at a fixed height of 0.4 m from the bottom. The EMF measured with an accuracy of 1%[60]. The instantaneous flow velocities were measured with a Nortek Vectrino acoustic velocimeter (ADV) at a fixed height of 0.4 m from the bottom. The ADV probe was installed 0.04 m upstream from the gap between two elements. The ADV measured the approaching flow before it was accelerated between two elements, and it had an accuracy of approximately 1%[111]. The output of both velocity sensors was in volts, and the velocities were obtained from linear regression, using separate calibration factors for each instrument.

The hydrodynamic loads acting on one single cylinder were recorded with a SCAIME load cell mounted on the upper part of the element, measuring in volts with 0.017% accuracy[130]. The load cells were calibrated using known weights, and fitting a linear relationship between weight and voltage output. The forces were calculated by multiplying the sensor output by the calibration factor, and by the acceleration of gravity.

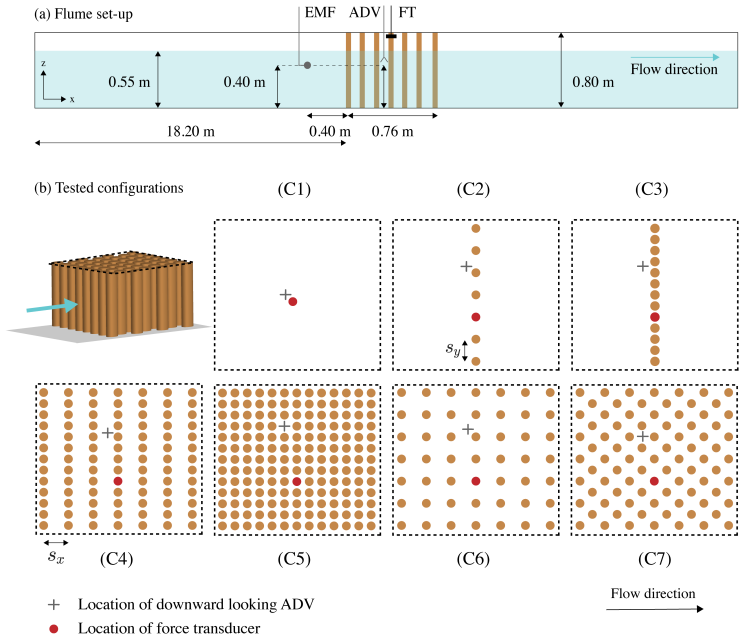

Figure A.1: (a) Side view of the instrument set-up in the flume, consisting of an electromagnetic flow meter (EMF), a Nortek Vectrino acoustic velocimeter (ADV) and a SCAIME load cell mounted on the upper part of the element (FT). (b) Configurations tested in the experiments. An oblique view of the structure is shown at the top left side of the plot, where the flow direction is indicated by a blue arrow. The top view of the structure is marked by a dashed black line, and it is illustrated for each of the tested arrangements: (C1) single cylinder with $d = 0.04$ m, (C2) single row with spanwise spacing between the elements of $s_y = 3d$, (C3) single row with spanwise spacing between the elements of $s_y = 1.5d$, (C4) multiple rows with $s_y = 1.5d$ and $s_x = 3d$ in uniform arrangement, (C5) multiple rows with $s_y = 1.5d$ and $s_x = 1.5d$ in uniform arrangement, (C6) multiple rows with $s_y = 3d$ and $s_x = 3d$ in uniform arrangement, and (C7) multiple rows with $s_y = 3d$ and $s_x = 3d$ in staggered arrangement.

The bulk drag coefficients were determined by using Equation 2.1 with the mean force measured at the center of each configuration, and the mean incoming velocity recorded by the EMF. The average forces and velocities were calculated using a moving average over intervals of 20 s.

B. Appendix B

Reconstructing the velocity profile

In the present appendix we have provided plots for the intermediate steps for reconstructing the velocity profile. We calculated the moving average of the time series over an interval of 0.25s. The resulting signal for the velocity measured by the EMF for 1C and $T = 3$s is shown in Figure B.1. For each wave condition and struc-

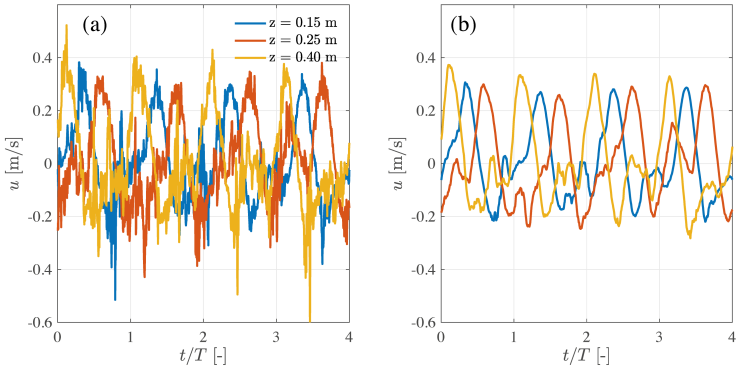

Figure B.1: (a) Measurements for 1C and $T = 3$ s before doing a moving average over 0.25 s. (b) Measurements for 1C and $T = 3$ s after doing a moving average over 0.25 s

ture configuration the velocities at different elevations from the bed were measured in separate tests. In order to build the velocity pro-

file, we calculated the time shift between the different experiments to ensure that the velocities at different elevations corresponded to the same phase of the wave. The time shift was calculated by maximizing the correlation between the measurements at WG2 of two experiments. The correlation function is given by Equation B.1:

$$R(\eta_1(t), \eta_2(t + \Delta t_s)) = \frac{\sum_{j=1}^{T/\Delta t} \eta_{1j}(t)\eta_{2j}(t + \Delta t_s)}{\sqrt{(\sum_{j=1}^{T/\Delta t} \eta_{1j}(t)^2)(\sum_{j=1}^{T/\Delta t} \eta_{2j}(t + \Delta t_s)^2)}} \tag{B.1}$$

Where η_1 and η_2 are the surface elevations for the experiment with velocity measurements at $z = 0.15$ m (which we arbitrarily chose as the reference case) and at a height z, respectively. T is the wave period, Δt is the time-step and Δt_s is the time shift. The velocity time series with and without correcting for the time shift are shown in Figure B.2 for 1C and $T = 3$ s. For 1C the mean velocities were extracted from the instantaneous velocity time series using the detrend function in Matlab. The velocities at the mean water level and at the bottom were extrapolated by doing a hyperbolic cosine fit of the measurements. The results for 1C and all wave periods are shown in Figure B.3.

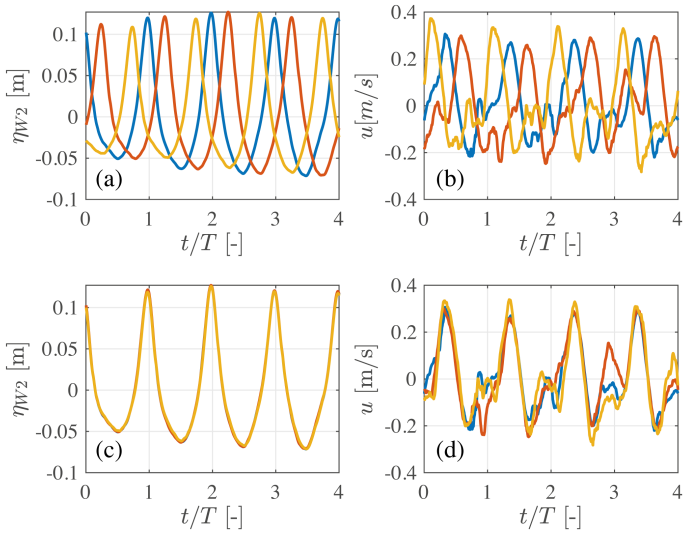

Figure B.2: The upper plots show the surface elevation (a) and the flow velocities (b) at tests where the velocity measurements were collected at different heights from the bed for $1C$ and T =3 s, prior to shifting the time series. The lower plots show the surface elevation (c) and velocity (d) measurements after time shifting the time series.

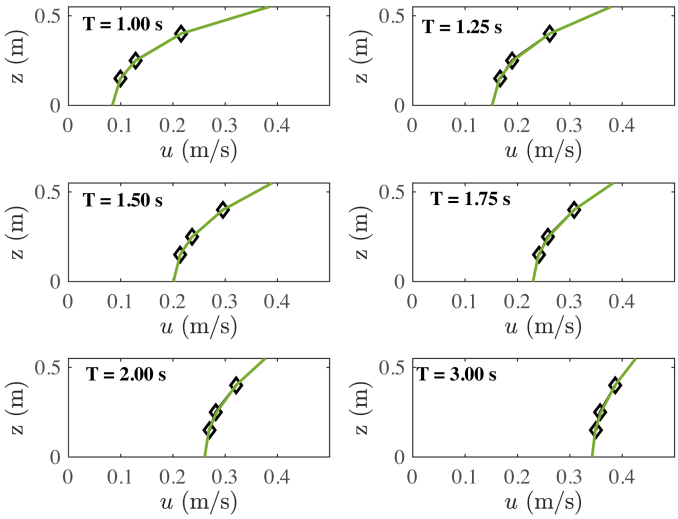

Figure B.3: Velocity measurements (black) and fitted hyperbolic cosine profile (green) for 1C and the six wave periods tested in the flume.

C. Appendix C

Sensor height

The height from the bed of the ADV and OBS sensors is shown in Table C.1.

Table C.1: Elevation of the sensors with respect to the bed, defined as the top of the soft mud layer.

Transect	Side	Sensor	Height from the bed [m]
T1	Seaward	ADV	0.28
		OBS	0.13
T1	Landward	ADV	0.36
		OBS	0.12
T2	Seaward	ADV	0.33
		OBS	0.33
T2	Landward	ADV	0.33
		OBS	0.24

Effect of sediment transport by tide

The effect of the sediment transport by tidal currents on the bed level changes is shown in Figure C.1 (a). Tidal currents had a significant role transporting sediment between areas with different

sediment concentration, such as at both sides of a structure. When the transport of sediment due to the tide (second term from the left in Equation 4.18) was set to zero, the erosion seawards from the structure became significantly smaller, and the sediment accumulation at the landward side disappeared.

Effect of the nearshore slope

The effect of varying the initial nearshore slope is shown in Figure C.1 (b) for the input parameters and hydrodynamic conditions of Section 4.4.2. Varying the slope largely influences the modelled morphology. A milder nearshore slope results in a larger water depth for a given distance with respect to the offshore boundary, and causes larger changes in the bed level compared to a steeper slope.

Effect of the profile shape

The effect of varying the initial profile shape on the morphodynamic changes over a monsoon period is shown in Figure C.1 (c) for the input parameters and hydrodynamic conditions of Section 4.4.2. The profile shape strongly influences the bed level changes. For instance, the effect of a structure on the morphology is more pronounced on a convex profile than on the measured bathymetry.

Effect of the concentration in the offshore boundary

The effect of varying the offshore sediment concentration on the morphodynamic changes over a monsoon period is shown in Figure C.1 (d) for the input parameters and hydrodynamic conditions of Section 4.4.2.

Using fixed values of the sediment concentration of $c = 0$ g/l and

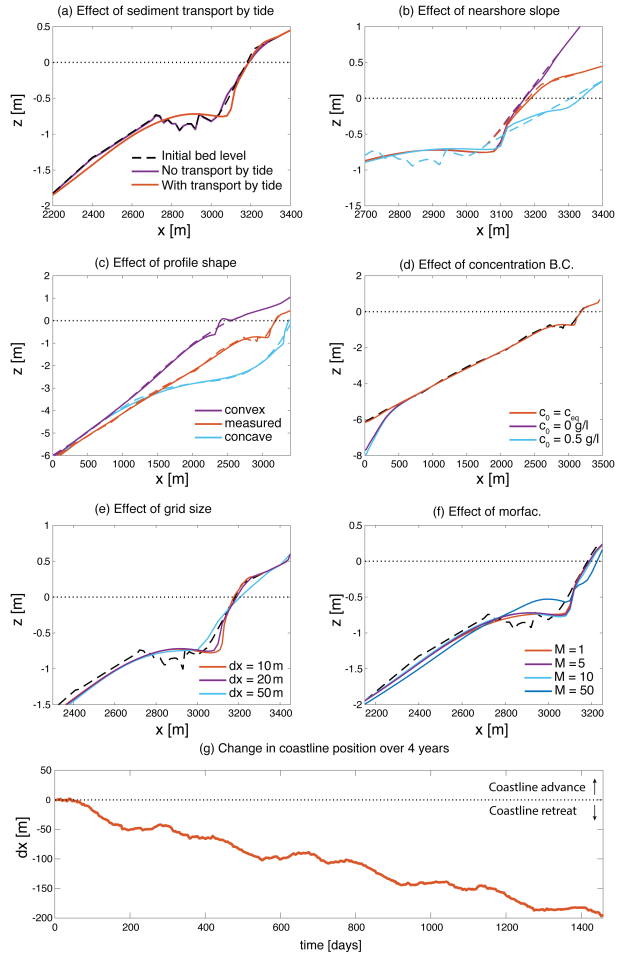

Figure C.1: Comparison of effect of a NW-monsoon period on the bed level with a structure placed at MSL (a) with and without the sediment transport by the tidal current, (b) for three different values of nearshore slope (defined between $x = 3050$ m and $x = 3450$ m), (c) for three different bathymetries, (d) for three different offshore boundary conditions for the concentration: with an equilibrium concentration $c = c_{eq}$, with $c = 0$ g/l, and with $c = 0.5$ g/l. Effect of varying the (e) grid size and (f) the morphological acceleration factor over a monsoon period. The initial bathymetries are shown by black dashed lines. (g) Coastline change over time without a structure, with $c_{max} = 0$ 0 g/l and no subsidence.

$c = 0.5$ g/l caused erosion over the most offshore part of the domain, but it barely affected the results at the nearshore in comparison to using an equilibrium concentration at the boundary.

Effect of grid size and of the morphological acceleration factor

The effect of varying the grid size and the acceleration morphodynamic factor is shown in Figure C.1 (e) and (f) for the input parameters and hydrodynamic conditions of Section 4.4.2.
Grid sizes larger than $dx = 20$ m and morphological acceleration factors larger than $m_e = 10$ induced significant changes in the final morphology, and we thus chose $dx = 20$ m and $m_e = 5$ to optimize the duration of our simulations.

Sensitivity analysis

The sensitivity of the model to variations of the sediment input parameters is shown in Figure C.2. The reference (default) values were equal to those used in Section 4.4.2. The period of the simulations corresponded with a 2-day storm with an offshore significant wave height of $H_s = 2$ m and a mean period of $T_m = 7$ s.
The model results were most sensitive to the critical shear stress, soil density, fall velocity, and erodibility parameter. This is consistent with these four parameters driving the erosive and depositional fluxes, and thus the bed level changes. The grain size and the diffusion coefficient had relatively smaller influence on the model results. The grain size had an indirect effect on the wave friction factor, whereas the effect of the diffusion coefficient was small due to the relatively low tidal velocities across the coastal profile.

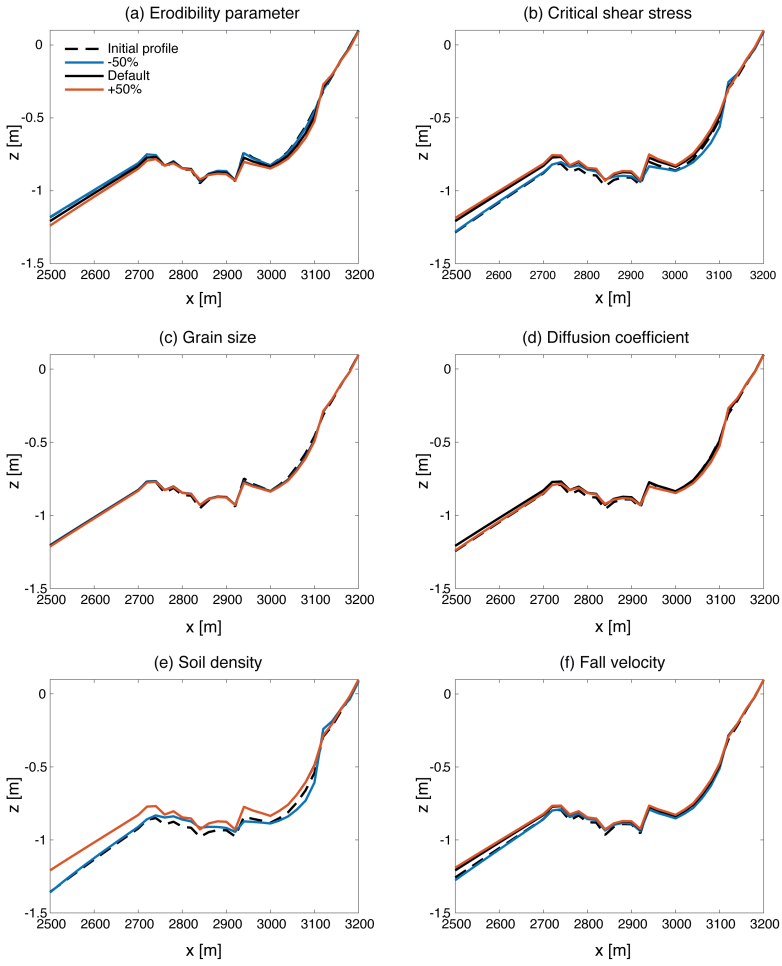

Figure C.2: Sensitivity analysis of the results for a 2-day storm period with $H_s = 2$ m and $T_m = 7$ s with respect to (a) the erodibility parameter m_e, (b) the critical shear strength τ_{cr}, (c) the mean grain size D_{n50}, (d) the diffusion coefficient D, (e) the soil density ρ_s, (f) and the fall velocity w_s.

Coastline change over time

The changes in the coastline position over a 4-year long simulation without a structure, without sediment supply (c_{max} = 0 g/l) and without subsidence, are shown in Figure C.1 (g). The sediment input parameters were equal to those used in Section 4.4.2. The hydrodynamic parameters corresponded to those used in Section 4.4.2. The profile shows a pattern of erosion during the NW monsoon, followed by some recovery and a mostly stable coastline position during calm conditions. The recovery after the NW monsoon is not complete, and the coastline shows a residual retreat over the 4-year period.

Acknowledgements

As civil engineers, we often design and build infrastructure with large benefits for people, but not so much for the rest of our ecosystem. When I first heard about this PhD position I thus felt immediately drawn to it - I had somehow found a field where it was possible to protect coastal areas while preserving and enhancing nature.

The process that followed has been a roller coaster, and at times quite challenging. Silke, Celine and I all did our PhDs together in the BioManCo project, and we had to figure out lots of things from scratch. From all the logistics behind international fieldwork (research permits, carnets, travelling with a ratio of 5 boxes to one person), to conducting field work in Indonesia - an activity that neither Silke or I had ever done. I was very lucky to share this learning process with Celine and Silke, who are among the most competent people I've ever met. We solved problems together as they came, supported each other over the last years, and our weekly meetings are a moment to look forward to every week.

A big thank you to Ruben (or Mr. Luberth, as he is better known in Indonesia), who joined us for our two field campaigns in Indonesia during his MSc. Ruben carried out his independent

research while also joining us in our activities. He was a big support in the field and remains to be a good friend. Thanks also to Tom Heuts for joining us in the first field campaign. It was a lot of fun to help him in his and Celine's biologic experiments, although I still think that seeing us uprooting trees, even if it was for a good reason, was probably a confusing message for the local people.

In the field we all had the invaluable help from Pak Yogi. For my field experiments I had to build very sturdy frames where we could place sensors, and bringing 200 kg of steel from the Netherlands was not really an option. Celine and I thus scootered around the city, searching for steel pipes in every construction shop. Our rustic Bahasa combined with our lack of any construction vocabulary made this quest daunting. However, in the last shop we visited, we found a shop manager who spoke English perfectly, and who became our local supplier.

Pak Yogi's first question was always, "what do you want this for?", which was followed by a redesign of our set-up. I feel a bit guilty of the tight deadlines we gave him, but I think (and hope) that deep inside he enjoyed problem-solving with us. If you ever need a hardware shop in Semarang, I highly recommend him.

Our fieldwork would have not been possible the invaluable help of many Indonesian colleagues. Special thanks to Aris, who kindly helped us to coordinate things between universities and backed us up in the field. A big thanks also to Pak Max and Pak Helmi, who helped us with the research permit process, flying to Jakarta if necessary to represent us, and supported us during our stay in Semarang.

I am also very thankful to Pak Saeri and Pak Slamet, who hosted

us and took care of us during our stay in Timbulsloko. Both of them, plus their families, dealt with dozens of European students (including myself) who probably caused all kinds of cultural miscommunications, all of which were kindly tolerated. Thank you to Pak Eko and Pak Apri, for their support, and for their inspiring work of protecting mangrove forests in Indonesia. And a heartfelt thank you to all the BSc and MSc students from Universitas Diponegoro who joined us in the field and in our workshops, and who spent their free time crawling together with us in the mud driven by their curiosity and willingness to learn.

In BioManCO we were lucky to research in parallel with an ongoing pilot project. Structures were built and experiments were being carried out as we did our PhDs. This also meant that we felt a sense urgency as we worked, since the pilot would finish exactly by the end of our projects, and we should thus give our input as soon as possible. This timeline also created a nice collaboration with our partners from Ecoshape and Wetlands International, as we could all learn from each other's work.

Thank you to Tom Wilms, who provided valuable input throughout the project and who supervised MSc students with us during the last 6 years. Another big thank you to the Deltares team: Bregje, Miguel, Amrit, Bob and Floris, who had an important role supporting us in the Netherlands and in the Demak. Bregje joined us in Timbulsloko, helped us interpret our results and their implications during our monthly team meetings, and provided helpful insights for Chapter 4 of this thesis. Miguel and Bob largely contributed to our research conducting sediment experiments with us at Deltares. Bob also carried out a deeper analysis of the consol-

idation experiments, and derived valuable parameters for Chapter 4. The analysis of the monitoring work by Amrit was also very insightful for this thesis, as it gave an overall perspective of the experience of the pilot.

Thanks also to Tjeerd, for his valuable help when he visited us in our first field campaign, and for his advice and enthusiasm during the last years. And thanks to Fokko, and Femke for joining us during the user group meetings, and to Roula and Maartje for making these useful meetings possible.

This work is largely influenced by the expertise and perspective of my supervisory committee:

Thanks to Wim, for offering me this opportunity, and for believing in my skills all along. His guidance also largely shaped Chapter 2 and Chapter 3 of this dissertation. I really enjoyed our discussions, and I have a deep respect for his strong conviction in fighting climate change and making our planet a better place.

I am also very thankful to Ad, who largely contributed to Chapter 3 and made Chapter 4 possible. Ad would often be quietly reflective as we presented any research problems in our meetings, and some time later, he would suddenly surprise us with a new model that could address those issues. He always tried to help BioManCO by any means he could find, and his support was also key during the finalization of this thesis.

A big thank also to Han, who made this project possible to begin with. I still can't believe that I trusted him when, during my interview, he told me that miraculously he barely saw any mosquitoes in Timbulsloko. However, I would have taken this opportunity with

or without mosquitoes, and I am very grateful of having had him as a supervisor, and for his valuable work in mangrove restoration.

Another big thank you to Peter, who helped conceptualizing and writing Chapter 5 of this thesis. During our team meetings Peter would interlink concepts of different and complex disciplines, from hydrodynamics to mangrove ecology, and he helped us pose the right questions. His ideas largely influenced my work and Celine's.

Special thanks also to Tomo and Arnold for the nice discussions and their important contributions to Chapter 3. Thank you to Mathijs van Ledden, Bas Jonkman, and Swarna Kazi, for giving me the opportunity to develop a mapping mangroves for Bangladesh, which I really enjoyed. And thanks also to Bas Hofland, Bregje, Han, and Peter to giving me the chance to continue working with them as a postdoctoral researcher, together with Lara, Wawan, Coco and Su. Special thanks also to Ibu Sri and Stefan, for kindly supporting the continuation of BioManCO through MUMACO.

Chapters 2 and 3 would have not been possible without MSc students Samantha and Wiljan, who did a great job conducting laboratory experiments. Thanks also to Pieter, Sander, Chantal, Arno, and all the laboratory team that made those experiments possible. Thanks also to all the other students that I have been very lucky to supervise and whose enthusiasm motivate my work: Esmée, Marijn, Tim, Koen, Kelvin, Tjerk, and Kimberly.

The Waterlab is filled by smart and fun people who create a really nice working atmosphere, thanks a lot to: Ana, Astrid, Bram, Claire, Claudia, Erik, Jianwei, Jill, Kifayath, Liselot, Lodewijk, Marco, Matt, Merel, Patricia, Stuart, Yorick, and Victor. Special thanks to Judith, whose course is probably the best one that I have

ever taken, and who always took the time to teach Yorick, Stuart and I how to educate. Thank you also to Marco, who made the first years much more fun organizing karaoke nights and making his awesome risotto.

Special thanks also to Jill and Ana, who are always happy to organize nice plans to bring everybody together, and who are a large contributing factor to the nice lab atmosphere. Another big thank you to Lodewijk, Bram, and Irene, who provided (life-saving) remote help when sensors failed in Indonesia. Lodewijk taught me the fundamentals of fieldwork, and was always happy to help Silke and I (besides being a fellow fan of Domino pizza). Claudia and Patri have been great friends during the last years, and they have both largely supported this work - bringing artistic inspiration, cheering up, and making the pandemic much more bearable, among many other things.

Thanks to Said and Stuart for the cozy dinners, and for their friendship, especially at the beginning, when the three of us were new at TU Delft and barely knew anyone else. Stuart has already been mentioned in several categories, and it would take a whole section to fully acknowledge his contribution to this thesis. He was always happy to proof-read chapters of this thesis, discuss about plots, and to provide emergency tortilla whenever needed. A big thank you to Ana Serrano, for her support during the last years despite the distance.

Before going into the lab, I shared an office with Silke, Sabine, Lotte and Irene. Thank you all for nice conversations and for the oatmeal coffee breaks; I am happy that we still keep them even when we have all spread over Europe. Thanks also to Otti for her

help during the last years, and to Sotiria, Steffie, Carine, Floris, Gal, Lennart and Juanma for creating such a nice environment in the second floor.

A big thank you to Daan, for his love and support, and for making our home a fun place to return to every day. I'm both amused and a bit fearful of what his next home project will be (as his projects are expanding in size and scope), but also looking forward to more happy years together.

Lastly, thank you to my family, to my brother and to my parents, who have always supported me unconditionally, and who taught me the work ethics, sense of adventure, and the inner curiosity without which this thesis would have never been completed.

List of publications

A. Gijón Mancheño, W. Jansen, W.S.J. Uijttewaal, J.C. Winterwerp (2021) Predictive model of bulk drag coefficient for a nature-based structure exposed to currents. *Scientific Reports 11.*

A. Gijón Mancheño, W. Jansen, W.S.J. Uijttewaal, A.J.H.M Reniers, A.A.van Rooijen, T. Suzuki, V. Etminan, J.C. Winterwerp (2021) Wave transmission and drag coefficients through dense cylinder arrays: implications for designing structures for mangrove restoration. *Ecological Engineering 165.*

A. Gijón Mancheño, A.J.H.M. Reniers, B.K. van Wesenbeeck, C.E.J. van Bijsterveldt, S.A.J. Tas, T. Wilms, M. Muskanonfola, and J.C. Winterwerp (2022) Restoring eroding mangrove coastlines using nature-based structures *(in preparation for submission).*

A. Gijón Mancheño, P.M.J. Herman, S.N. Jonkman, S. Kazi, I. Urrutia, and M. van Ledden (2021) Mapping Mangrove Opportunities with Open Access Data: A Case Study for Bangladesh. *Sustainability, 13(15).*

A.J.H.M. Reniers and A. Gijón Mancheño (2022) XMgrove: Morphodynamic Mangrove Profile Modeling. *(in preparation for submission).*

T. Schoonees, A. Gijón Mancheño, B. Scheres, T. J. Bouma, R. Silva, T. Schlurmann and H. Schüttrumpf (2019). Hard Structures for

Coastal Protection, Towards Greener Designs. *Estuaries and Coasts, 42*.

Winterwerp, J.C and Albers, T. and Anthony, E.J. and Friess, D.A. and Gijón Mancheño, A. and Moseley, K. and Muhari, A. and Naipal, S. and Noordermeer, J. and Oost, A. and Saengsupavanich, C. and Tas, S.A.J. and Tonneijk, F.H. and Wilms, T. and van Bijsterveldt, C.E.J. and Van Eijk, P. and van Lavieren, E. and and Van Wesenbeeck, B.K. (2020). Managing erosion of mangrove-mud coasts with permeable dams – lessons learned. *Ecological Engineering, 158*.

Van Bijsterveldt, C.E.J. and van der Wal, D. and Gijón Mancheño, A. and Fivash, G. and Helmi, M. and Bouma, T.J. (2022). Can cheniers protect mangroves along eroding coastlines? – A study investigating the effect of different fore-shores on long-term stability of mangroves *(in preparation for submission)*.

Hendriks, I.E., Marba, N., van Wesenbeeck, B.K., Gijón Mancheño, A., Bouma, T.J., Maza, M., Losada, I.J., and Duarte, C.M. (2022). Climate Change Adaptation Benefits of Coastal Vegetation *(under review)*

Sirks, E., Kuipers, C., and Gijón Mancheño, A. (2021). Schaalmodelonderzoek naar ontwerpoptimalisatie van permeabele dammen voor mangroveherstel. *Civiele Tekniek*.

Curriculum vitae

EXPERIENCE

MAR 2021 - MAR 2025 Postdoc researcher, Delft University of Technology

SEP 2016 - MAR 2021 PhD candidate, Delft University of Technology

MAR 2020 - MAY 2020 Consultant, Delft University of Technology

OCT 2014 - DEC 2014 Research assistant, Norwegian University of Science and Technology

MAR 2014 - JUL 2014 Intern, TYPSA

EDUCATION

SEP 2016 - MAR 2021 PhD degree in Environmental Fluid Mechanics, Delft University of Technology

SEP 2014- JUL 2016 MSc in Coastal and Maritime Engineering and Management. Delft University of Technology, University of Southampton, Norwegian University of Science and Technology, Cum Laude

SEP 2010-JUL 2014 BSc in Civil Engineering (Especialization in Hydraulics), Universidad de Sevilla, Valedictorian

Over history human beings have lived at the shelter of mangroves. People built houses with their wood, and fished between their roots. Extensive mangrove deforestation for farming during the 20th century left coastal communities vulnerable storm waves, and deprived from their ancient provision of food and safety. This PhD thesis explores how to recover mangrove forests, using bamboo structures that imitate the lost mangrove trees.

Delft, 2022